

Modelling the mechanical performance of bolted deck-to-girder connections in FRP-steel hybrid bridges

Jan Swinnen

Delft University of Technology

Modelling the mechanical performance of bolted deck-to-girder connections in FRP-steel hybrid bridges

by

Jan Swinnen

in partial fulfilment of the requirements for the degree of

Master of Science
in Civil Engineering

at the Delft University of Technology,
to be defended on 15th of October 2020.

Student number: 4493575
Project duration: 1 December 2019 – 15 October 2020
Thesis committee: Dr. M. Pavlović, TU Delft, Chairman
Dr. Ir. G. Ravenshorst, TU Delft
Dr. Ir. M. Hendriks, TU Delft
Ir. M. Rikken, Arup
Ir. F. Csillag, Arup



ARUP

Abstract

In recent years, a growing amount of movable highway bridges with a timber deck are approaching the end of their service life. Since these bridges have opened, the traffic intensity has increased yearly and environmental effects had the opportunity to deteriorate the bridges slowly. Inspections revealed that the main load-carrying elements are generally in adequate conditions while the deck structure is deteriorated. In an effort to extend the bridge's lifetime, fibre-reinforced polymer (FRP) decks can be used to replace deteriorated members. These decks have gained popularity over the past years due to their high strength-to-weight and stiffness-to-weight ratio's which enables fast installation. Furthermore, their freedom in design, the ability to be prefabricated and good durability are all characteristics that make FRP bridge decks a worthy competitor for the refurbishment of movable bridge decks. The main challenge of applying FRP bridge decks is connecting it with the underlying steel girders. Fortunately, recent developments of deck-to-girder connections have suggested a slip-resistant demountable shear connection, namely, the injected Steel Reinforced Resin (iSRR) connection. Initial experiments of the iSRR connection concluded that the connection provides excellent fatigue behaviour which is favourable in hybrid FRP-steel bridges.

The main objective of this thesis is to investigate the behaviour of bolted deck-to-girder connections in FRP-steel composite bridges with the application of renovating movable highway bridges with timber decks. Using a series of finite element models, the application of a bolted FRP deck is investigated on an existing movable highway bridge, namely, the Beneden Merwede bridge. In order to achieve interaction between the existing steel structure and FRP panels, the slip-resistant iSRR connections are considered. Starting from a small-scale finite element model of the iSRR connection, a process of simplifications and upscaling of the models will lead to a large-scale bridge model. Firstly, a highly detailed model of a push-out test is developed to assess the static performance of the iSRR connector with embedded nuts and a coupler system. Secondly, the mechanical performance of an FRP-steel composite system is investigated in a composite beam model. Using the latter model, different modelling techniques of the deck-to-girder connections are compared in order to propose an efficient technique to determine the forces in the deck-to-girder connections. Finally, a large-scale bridge model is used to determine the forces in the deck-to-girder connections under a number of load cases and to provide a recommendation for the distribution of the connections.

The analyses of the iSRR connection with the embedded nuts and coupler show that both configurations have a similar static behaviour characterised by the shear rupture of the connection and limited damage to the FRP. Based on the known long-term behaviour of the iSRR connection with the embedded nuts, it is advised to use this type of configuration as deck-to-girder joint. Applying the connection on the composite beam model every 600 mm, the iSRR connections provide full composite action between the FRP deck and the steel girder and preserves the interaction between the two components until yielding of the steel beam is initiated. The composite beam analysis also concludes that connection forces may be reduced when friction is not considered during the analysis, e.g. during engineering analysis with linear springs ($212kN/mm$) in GSA. Investigating the deck-to-girder connections on the bridge level, it is advised to install iSRR connections on the cross- and main-girders to connect the FRP deck. In such manner, the deck is well supported in longitudinal and transverse direction of the bridge and local force concentrations near the cross- to main-girder connection are prevented. When connecting the FRP panel to the cross- and main-girders, the bending moments in the cross- to main-girder connections are significantly reduced compared to the original design of the bridge with a timber deck.

Keywords: Fibre Reinforced Polymers, FRP-steel bridges, bridge renovation, deck-to-girder connections, iSRR connection, finite element modelling & techniques

Acknowledgements

As part of my studies at the TUDelft, this thesis marks the end of obtaining my Master's degree in Civil Engineering. Therefore, I would like to express my gratitude to everyone that contributed to this thesis and my experiences at the TUDelft.

Firstly, I want to thank my committee members who patiently advised me on both technical and personal matters. Supervising me during both my BSc and MSc thesis, my gratitude goes out to my chairman, Marko Pavlović. Throughout my thesis, you've always been there to keep me on track and encourage me to go beyond my limits. I am thankful for my two university supervisors, Max Hendriks and Geert Ravenshorst, who provided a critical view on my work.

I would like to express my deepest appreciation to my company supervisors, Fruzsina Csillag and Maarten Rikken, for being always available and energising. Fruzsina, I would like to thank you for introducing me to Arup and the field of FRP-steel connections. Your extensive knowledge and previous research work have been a major source of inspiration for this thesis. Maarten, during my internship and thesis you've always provided me with constructive feedback and shared your valuable experiences. You pushed me to look further than the theory and consider the practicality of the application.

Secondly, my sincere gratitude goes to everyone from the infrastructure team at Arup Amsterdam. From the very first day, I was amazed by the great working atmosphere and the passion that was driving the team. During my internship and thesis, I was always able to rely on the experience of many colleagues in the team and learn from them. I wanted to thank Maureen, Kevin, Tessa, Albin, Laetitia, Ronan, Katinka, Alwin, Paul, Roel, Mike, Felix and all others for the numerous coffee break discussions and support.

Last but not least, I want to thank my friends, family and my sister, Christina, for their continuous support and care. When I needed a break, you were always there to clear my mind and provide positive energy. Special thanks go to my girlfriend, Sandra. During my whole thesis, you've been by my side and encouraged me until the finish line. My utmost gratitude goes out to my parents, Nilda and Jan, for their unconditional love and supporting my wish to become an engineer.

*Jan Swinnen
Amsterdam, October 2020*

Contents

Abstract	ii
Acknowledgements	iii
List of Symbols	vi
List of Abbreviations	vii
1 Introduction	1
1.1 Problem statement	1
1.2 Aim of the research	2
1.3 Methodology	3
1.4 Outline	5
2 Literature review	6
2.1 FRP bridge deck systems	6
2.1.1 Deck geometry & performance	7
2.2 Connection methods	10
2.2.1 Deck-to-girder connections	10
2.2.2 iSRR connector	13
2.3 FRP-steel composite beams	16
2.3.1 FRP-steel composite beam tests	17
2.3.2 Analytical approximations	19
2.4 Summary	21
3 Case study: Beneden Merwede bridge	22
3.1 Renovation design	25
3.1.1 FRP deck & material properties	25
3.1.2 FRP-to-steel connection design	27
3.1.3 Requirements for the FRP-steel connection	27
3.2 Summary	29
4 Connection level	30
4.1 Modelling technique	30
4.1.1 Geometry & boundaries	30
4.1.2 Mesh & interaction	31
4.1.3 Loading & Analysis	32
4.1.4 Material models	33
4.2 Results	34
4.2.1 Force-displacement behaviour	34
4.2.2 Stiffness & ductility	36
4.2.3 Verification	37
4.3 Discussion & recommendation	38
4.4 Summary	39
5 Composite beam level	40
5.1 Modelling technique	40
5.1.1 Geometry & boundaries	40
5.1.2 Mesh & interaction	41
5.1.3 Loading & analysis	41
5.1.4 Material models	42

5.2	FRP-to-steel interaction	43
5.3	Results	46
5.3.1	Force-displacement behaviour	46
5.3.2	Stresses and strains evaluation	49
5.3.3	Verification	50
5.4	Comparison of modelling techniques	51
5.4.1	Abaqus composite beam model simplification	51
5.4.2	GSA composite beam model simplification	51
5.4.3	Influence of friction on connection forces	53
5.5	Discussion of results	56
5.5.1	Composite action of the FRP panel	56
5.5.2	Effective width	61
5.5.3	Connector spacing	62
5.6	Summary	65
6	Bridge level	67
6.1	Modelling technique	67
6.1.1	Permanent loads	69
6.1.2	Variable loads	69
6.2	Analysis of the deck-to-girder connections	72
6.2.1	Serviceability limit state	73
6.2.2	Ultimate limit state	77
6.3	Connecting the main-girder	82
6.4	Comparison with timber deck	86
6.4.1	Cross- to main-girder connection	86
6.4.2	Main-girder bending and displacements	88
6.5	Summary	89
7	Conclusions & recommendations	91
7.1	Conclusions	91
7.2	Recommendations for further research	94
	Bibliography	95
	List of Figures	98
	List of Tables	101
A	Beneden Merwede bridge	102
B	Connection model	104
B.1	Material models	104
B.2	Results	107
B.3	Verification connection model	109
C	Composite beam model	111
C.1	Influence of foam core	111
C.2	Connection simplification	112
C.3	Steel beam model	113
C.4	Verification composite beam model	114
C.5	Transverse bending effect	120
C.6	Secondary moment effect	121
C.7	Connector spacing $c_w = 1200mm$	122
D	Bridge model	123
D.1	Permanent loads	123
D.2	Connector forces: Cross-girder	125
D.3	Connector forces: Cross- and main-girder	132

Symbols & abbreviations

List of Symbols

$\alpha_{friction}$	Friction force factor
α_r	Coefficient of thermal expansion of the resin
δ_{uk}	Ultimate slip
ϵ_L	Longitudinal strain
ϵ_T	Transverse strain
γ	Shear lag factor, degree of composite action or safety factor
μ	Friction coefficient
ψ	Combination factor
σ_L	Longitudinal stress
σ_T	Transverse stress
A	Area
A_s	Stress area
$b_{f,a}$	Steel flange width
b_{eff}	Effective width
c_w	Connector spacing
E	Young's modulus
$F_{p,C}$	Prestress force
f_{ub}	Ultimate stress
F_s	Slip force
F_v	Shear force
F_x	Force in x-, longitudinal- or axial direction
F_y	Force in y- or transverse direction
G	Shear modulus
$h_{w,a}$	Steel web height
h_c	FRP core height
h_d	FRP deck height
I	Moment of inertia
k	Stiffness
k_{sc}	Secant stiffness

L	System length
q	Pressure load
Q	Variable load
s	Slip displacement
s_w	FRP web spacing
$t_{f,a}$	Steel flange thickness
$t_{w,a}$	Steel web thickness
t_f	FRP facing thickness
t_w	FRP web thickness
ν	Poisson ratio
V_f	Volume fraction

List of Abbreviations

<i>BBM</i>	Beneden Merwede bridge
<i>CG</i>	Cross-Girder
<i>FEA</i>	Finite Element Analysis
<i>FEM</i>	Finite Element Modelling
<i>FLM</i>	Fatigue Load Model
<i>FRP</i>	Fibre Reinforced Polymer
<i>iSRR</i>	injected Steel Reinforced Resin
<i>JRC</i>	Joint Research Centre
<i>LM1</i>	Load Model 1
<i>POT</i>	Push-Out Test
<i>PU</i>	Polyurethane
<i>RWS</i>	Rijkswaterstaat
<i>SLJ</i>	Single-Lap Joint
<i>SLS</i>	Serviceability Limit State
<i>SRR</i>	Steel Reinforced Resin
<i>TS</i>	Tandem System
<i>UDL</i>	Uniformly Distributed Load
<i>ULS</i>	Ultimate Limit State
<i>VARTM</i>	Vacuum Assisted Resin Transfer Molding

1

Introduction

1.1. Problem statement

During the 50s and 60s, large infrastructure investments were made to support the growing road use demand. Many bridges in the Netherlands, dating back from that period, are currently approaching their end of service life. In an effort to assess the structural reliability of those bridges, the Dutch highway authority (Rijkswaterstaat) classified that some of these bridges are in a structurally poor condition. Since their opening, the traffic intensity has increased yearly and environmental effects had the opportunity to deteriorate the bridges slowly.

In the past, many movable bridges were built having a lightweight timber deck. Their structural design comprises mostly four components: timber planks, supported by steel secondary-, cross- and main-girders respectively. After years in use, inspections uncovered that water was infiltrating between the timber planks which caused the corrosion of the secondary girders. The ± 5000 bolts that connect the timber planks to the secondary girders have to be retightened yearly. Consequently, the timber deck systems turned out to be maintenance and inspection demanding.

Recent developments suggest that fibre-reinforced polymer (FRP) bridge decks have become a good alternative compared to timber and orthotropic steel decks. The main advantages of using composites are their good fatigue resistance, high strength- and stiffness-to-weight ratio's. Furthermore, their freedom in design, fast construction time, low maintenance and good durability are all characteristics that make FRP bridge decks a worthy competitor for the refurbishment of movable bridge decks.

Because of the structural deficiencies of the timber deck system, Rijkswaterstaat is considering whether they should replace or renovate these movable bridges. As an alternative to the replacement of the entire bridge, prefabricated FRP deck panels can be used for the rapid replacement of the timber deck planks and the corroded secondary girders. Moreover, the decrease in self-weight of a new FRP deck system can reduce permanent stresses in the existing cross- and main-girders and prolong the service life of the movable bridge.

A challenge in designing composite bridges is connecting its components together. In the case of FRP composite structures, additional obstacles must overcome such as the orthotropic material properties and the lack of material plasticity. FRP-steel joints can be designed to engage or neglect the composite action between the deck and the underlying steel girders. The degree of hybrid interaction measures the level by which the steel girders work together with the FRP deck. Generally, FRP-steel hybrid bridges are designed without hybrid interaction. But by using slip-resistant connections such as shear studs and adhesive bonds, hybrid interaction between the FRP deck and steel superstructure can be exploited.

Engaging hybrid interaction leads to an increase in the structure's bending stiffness, which generally results in lower stresses and a reduction in effective material usage. This could be advantageous for the remaining service life of renovated bridges. On the contrary, an increase in hybrid interaction implicates larger forces in the FRP-steel connections. It is therefore important that the connections between the FRP deck and the steel superstructure are designed to cope with the interaction forces during their lifetime.

1.2. Aim of the research

The aim of this thesis is to...

...investigate the behaviour of deck-to-girder connections in FRP-steel composite bridges with the application of renovating movable highway bridges with timber decks.

In order to achieve interaction between the existing steel structure and FRP panels, slip-resistant injected steel-reinforced resin (iSRR) connections are considered. As physical tests are usually expensive and require careful preparations, the composite behaviour of the FRP-steel system will be numerically analysed by means of Finite Element Modelling (FEM). FEM can offer cost and time-efficient solutions for a large design space. Moreover, the ability to take a deep dive into performance drivers can help to focus test design efforts. To expand the main research aim, specific objectives are defined:

1. Propose and investigate a slip-resistant iSRR connection assembly suitable for the renovation of movable highway bridges with FRP deck panels
2. Investigate the mechanical performance of an FRP-steel composite system which is joined by slip-resistant iSRR connections
3. Develop an efficient numerical modelling method to determine the forces in bolted FRP deck to steel girder connections for global bridge analyses
4. Determine the forces in bolted FRP deck to steel girder connections under several traffic and thermal load cases for movable highway bridges and provide a recommendation for the distribution of the connections

In order to formulate these objectives in straightforward and answerable questions, the following research questions are considered:

1. What is the load-displacement behaviour of the iSRR connections and which one is most suitable as deck-to-girder connection in movable highway bridges with FRP deck panels?
2. Investigating the mechanical performance of an FRP-steel composite system, what is the failure mechanism, degree of composite action, and effective width of the system?
3. How can the forces in deck-to-girder connections be efficiently determined in engineering-oriented software? And, what is the influence of friction at the FRP-steel interface on the forces in the deck-to-girder connections?
4. Under a number of load cases, which forces can be expected in the deck-to-girder connections on a movable highway bridge and to which elements should the connections be attached?

1.3. Methodology

In order to investigate the behaviour of deck-to-girder connections in FRP-steel composite bridges, some starting points were defined:

- Recent studies performed by Csillag [1] on demountable deck-to-girder connections between steel and FRP, showed promising static, fatigue and creep results by the slip-resistant iSRR connection. Experimental test results of this type of connector will be used to verify numerical analyses.
- The analyses will be applied on a reference bridge, the 33x15 meter Beneden Merwede bridge near Papendrecht, which has a similar lay-out as other movable bridges owned by the Rijkswaterstaat.
- The design of the FRP deck will be based on the InfraCore deck system, manufactured by the Dutch company FiberCore Europe. FibreCore is a well known FRP deck producer in Europe which has its manufacturing facility near the Beneden Merwede bridge.

Using a series of finite element models, the application of the iSRR connection for the renovation of the Beneden Merwede bridge will be investigated on three levels: the connection, composite beam and bridge level. Starting from a highly detailed small-scale connection model, a process of simplifications and upscaling of the models will lead to a large-scale bridge model as can be seen in figure 1.1. In efforts to decrease modelling complexities in each simplification step, a level of detail will be lost. Accordingly, the differences in results will be studied as follows:

- Connection: With a highly detailed small-scale finite element model, the behaviour of the proposed iSRR connections is quantified. The main points of interest are: stiffness, ductility, ultimate resistance and failure mechanism.
- Connection simplification: In order to implement the iSRR connections on a medium-scale composite beam model, some modelling simplifications have to be made. The impact of these simplifications is investigated by comparing the behaviours of the simplified connection model and the highly detailed connection model.
- Composite beam: The behaviour of the FRP-steel composite beam system is studied by modelling an FRP deck strip on top of a steel girder which are connected by the simplified iSRR connections. The investigated areas are: stiffness, forces in the connections, failure mechanism, effective width and degree of composite action.
- Composite beam simplification: At this stage, a software switch is made. In the previously described steps, non-linear modelling was used in the research-oriented software Abaqus. To compare the behaviour of the composite beam system in engineering software, a linear model is created having identical geometries and properties as the composite beam model in Abaqus. The behaviour of the composite beam and more specifically the interaction between the FRP deck and steel girder, is compared between the software.
- Bridge: The last stage comprises the modelling of the large-scale bridge which is used by engineers to assess the bridge's structural performance under various bridge loadings. A full assessment of the bridge's components is out of the scope of this thesis but a critical look will be made to the deck-to-girder connection forces for governing loading schemes.

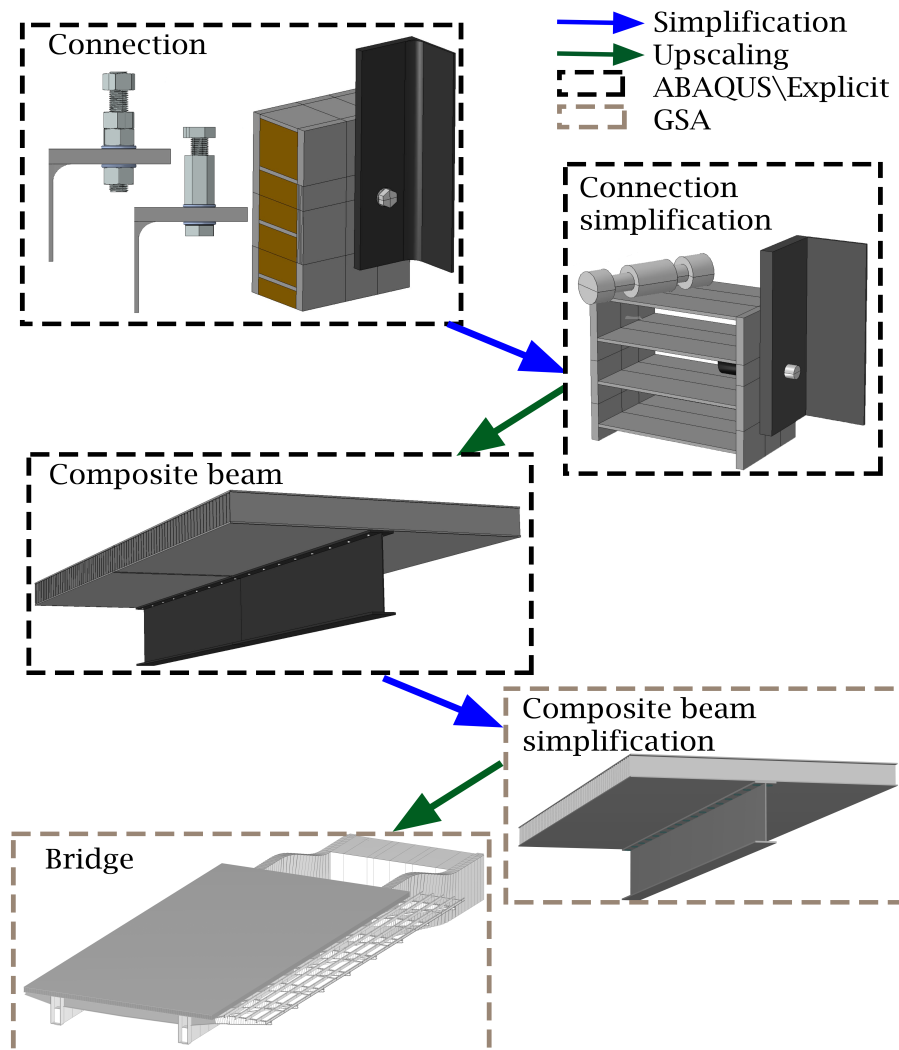


Figure 1.1: Numerical analyses overview

1.4. Outline

Firstly, the literature review summarises previously completed studies in the fields of FRP bridge deck systems, connection methods and FRP-steel composite beams.

In chapter 3, the case study of an existing movable highway bridge is introduced. The current structural design is portrayed together with its design flaws. Based on the present design issues, a renovation design is introduced.

By investigating the proposed connection techniques, chapter 4 tackles objective 1. Through the finite element modelling of push-out tests, connection techniques are characterised and validated. Results for the connection stiffness, ductility and ultimate resistance are compared to values suggested by literature and analytical calculations.

The investigation of objectives 2 and 3 are elaborated in chapter 5. The performance of the FRP-steel composite beam is analysed through finite element modelling. Connection modelling techniques are simplified to study the influence of friction on the connection forces.

Chapter 6 reflects on objective 4. The strengthening scheme portrayed in chapter 3, is modelled in a large-scale bridge model to analyse the connection forces under critical loads. The generated connection forces will be compared to results from chapter 4.

In the final chapter 7, the main conclusions are drawn and suggestions are made for future work.

2

Literature review

In the 1960s, the aerospace industry was looking for lightweight high-performance material. By combining high-strength fibres with light-weight, environmental resistant polymers, a Fibre-Reinforced Polymer was created that performed better than the two components alone. Nowadays, FRP composites are applied in many areas of the construction industry, including the rehabilitation of bridge decks. In the following chapter, the reader will be introduced to the application of FRP decks in FRP-steel hybrid bridges.

2.1. FRP bridge deck systems

Traditional bridge decks made of steel, timber and concrete are subject to environmental deterioration processes like corrosion, rot or freeze-thaw cycles. [2] Due to FRP's high environmental resistance and low future maintenance requirements, it has become a worthwhile competitor to the aforementioned traditional materials and an expanding area of research interest.

FRP offers several advantages in bridge deck applications. The high strength-to-weight ratio of FRP together with available prefabrication methods has proven to be efficient during the construction of new bridges and the renovation of existing bridges. When replacing old bridge decks, savings on dead weight can lead to an increased live load capacity to meet today's standards. Furthermore, the installation of lightweight FRP bridge decks can be rapidly done by simple equipment. This leads to cost savings, improved work-zone safety and a reduced bridge down-time. [3] In the long run, FRP decks have the potential to offer low life cycle costs due to several reasons. According to the layers of Brand, an FRP deck acts as the skin of a bridge's structure while protecting the underlying steel structure from environmental effects such as rain, frost, de-icing salts, etc. [4] As FRP has a high tolerance for these effects, it results in a reduction of inspection and repairing costs. [5]

Despite all the advantages, the application of FRP bridge deck systems is still limited compared to traditional alternatives. Both technical and institutional barriers have to be overcome to broaden the application of FRP decks. The material needs to gain traction in civil engineering applications with universally accepted design codes. Currently, only a limited amount of design applications are codified in international standards such as JRC reports. [6] A lack of data on the long-term in-service performance and high initial costs of FRP decks are also factors that make the implementation of FRP a challenging design choice. [7]

Nowadays, a wide range of prefabricated FRP decks are commercially available. Typically, these decks can be subdivided into pultruded panels and sandwich panels. Pultrusion is a continuous process where the reinforcement materials, like fibres or woven fabrics, are impregnated by the resin and pulled through a heated die which polymerises the resin. As the die has a constant profile, pultruded panels are unidirectional with a straight and constant depth. Usually, these panels are glued together to form the deck which spans between two or more girders. The deck is oriented with the pultrusion direction perpendicular to the girder since the panels can be considered as load-carrying in the direction of pultrusion only.

Sandwich decks are often made by Vacuum Assisted Resin Transfer Molding (VARTM) or the manual hand lay-up method. The hand lay-up method is a labour-intensive process where fibre reinforcements

are placed by hand in a mold and then impregnated with resin. The process is used for small production amounts and applications where high fibre-volumes or strict fabrication tolerances are unnecessary. The VARTM process is a more advanced molding technique which involves the use of a vacuum bag to facilitate the resin flow into the fibre lay-up. The process provides a high-quality product, fast resin injection and high fibre volume fractions. Both molding techniques are used to create sandwich decks which include two stiff facing plates joined to a core material. Compared to pultruded decks, sandwich panels have a great flexibility in cross-section configuration and can be formed in large deck sections. Moreover, the structural load-carrying behaviour can be regarded as bi-directional with span lengths up until 10 meters.

An important feature of FRP decks is that the deck geometry and material properties can be tailored to serve different needs when carefully designed. Factors such as fibre and resin material properties, fibre orientations and geometrical configurations can be tweaked to obtain desired stiffnesses in multiple directions. In such a way, a designer can optimise the deck geometry to maximise the effective material usage.

2.1.1. Deck geometry & performance

The cross-section geometry plays an important role in the structural behaviour of the FRP deck and influence the deck properties to a larger extent than the material properties. Typically, the core of an FRP deck is categorised into solid, thin-walled cellular and truss-like cores as indicated in table 2.1. Decks with solid cores are built-up from two stiff FRP face sheets that carry flexural loads and a bonded core material such as foam or balsa wood. The resistance due to patch loading of solid core panels is determined by the strength of the core material. As the strength is usually low, these types of panels suffer from local core crushing due to patch loads. [8] FRP decks with thin-walled cellular cores are also bonded to facing sheets. For the geometry of the cellular core, the common choices are sinusoidal- or honeycomb-shaped cells. Although thin-walled cellular cores have a larger capacity for local patch loads than solid cores, both core types are prone to debonding of the face sheets due to local impact. Their application for road bridges is therefore limited. [9]

A large geometrical variety of truss-like cores exist in both pultruded and VARTM produced FRP panels. The cross-section configuration of the facing sheets together with the web elements, can range from triangular to hexagonal shapes as can be seen in table 2.1. The cross-section configuration, the inclination angle of the webs as well as the thickness of the facings and webs have a major effect on the stiffness, strength and failure mode of the FRP deck. Shear experiments conducted by Gürtler [10] demonstrated that pultruded decks with triangular shapes (ASSET deck) have a higher in-plane shear stiffness in transverse direction than trapezoidal (DuraSpan) or rectangular shapes. This can be explained by the structural triangulation principle which dictates the use of triangular shapes to provide a stable structure. Shear and bending forces are replaced by compression and tension forces in the webs. When using non-triangular shapes, loads are transferred by Vierendeel action where strains between the top and bottom facings have to be transferred through bending and shear of the webs.

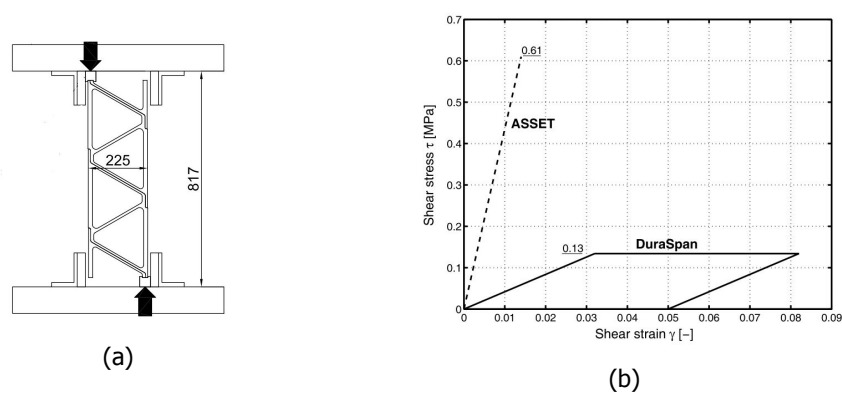


Figure 2.1: Shear experiment set-up of ASSET deck (a) and in-plane shear results for the ASSET and DuraSpan deck (b) [10]

Studies by Lee *et al.* [11] on the longitudinal and transverse flexural behaviour of three different VARTM produced FRP panels with triangular, trapezoidal and rectangular shapes, are in agreement with Gürtler [10]. As observed in graphs 2.2d and 2.2e, the longitudinal stiffness of the three shapes are similar whereas in transverse direction the triangular shapes are stiffer. In the strong longitudinal direction, the decks show almost linear elastic behaviour up to the brittle failure load whereas non-linear behaviour can be observed in the weak transverse direction. When loaded in transverse direction, the FRP panels with trapezoidal and rectangular configuration can dissipate energy during a progressive failure process, resulting in a more ductile failure compared to the brittle failure of the triangular configuration.

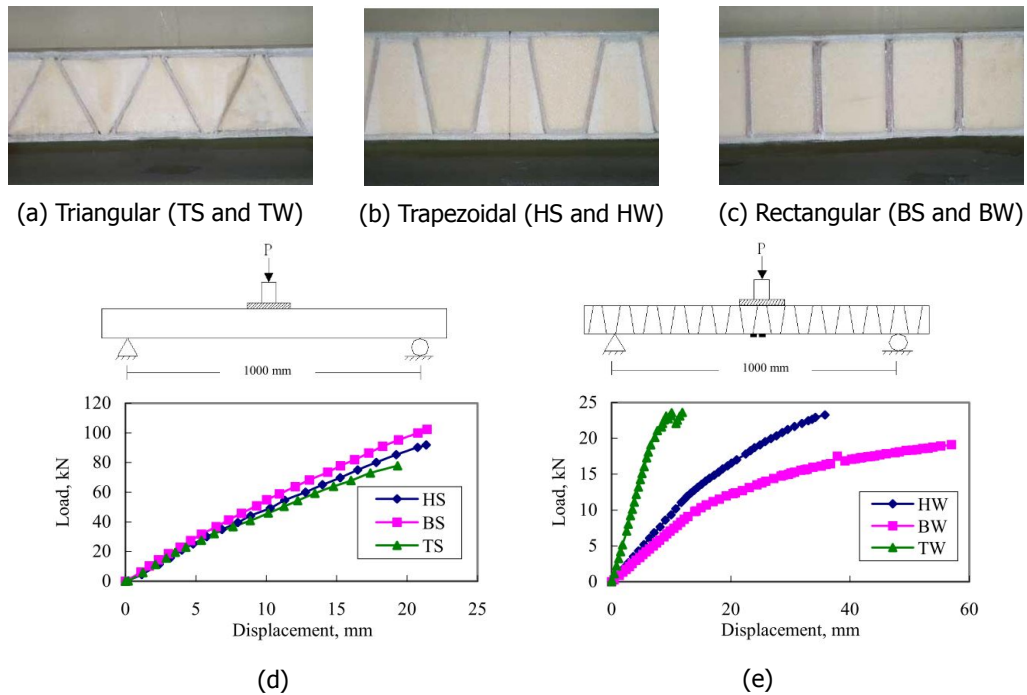


Figure 2.2: VARTM produced deck with triangular (a), trapezoidal (b) and rectangular (c) shapes and their longitudinal (d) and transverse (e) 3-point bending test results [11]

Failure modes of FRP decks often depend on their manufacturing method and geometrical configuration. Pultruded profiles mainly fail by local buckling of the webs, punching shear failure and delamination of the webs from the facings. Both local buckling of the webs and punching shear failure are caused by high local loads or impacts. Delamination often takes place at the location where the fibres change direction, i.e. at the intersection between the webs and facings. At these locations, a combination of interlaminar shear stresses and peeling stresses causes the lamina to separate. [12]

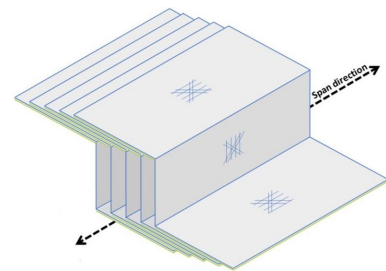
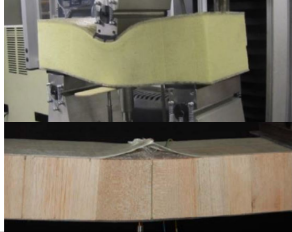
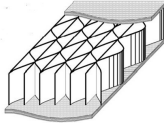
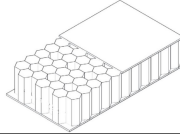


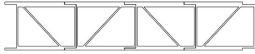



Figure 2.3: Z-shaped FRP laminates of InfraCore deck

As mentioned earlier, for sandwich decks where the facings are bonded to the core material, the most common failure is debonding of the facing sheets. This failure mechanism is triggered by shear stresses that overcome the bond strength in the interface of the core and facings. The VARTM produced InfraCore deck has overcome this type of failure by using a PU foam core surrounded by Z-shaped layers of FRP which prevent the initial cracks from spreading.

Table 2.1: Examples of different FRP panel configurations

Core configuration	Production	Deck height (mm)	Expected failure mode	Figure
Solid core				
Foam (MS&T, USA) [8]	VARTM	55	Local crushing of core due to patch loads	
Balsa wood (EPFL, CH) [13]	Hand lay-up	104	Debonding of top facing	
Thin-walled cellular core				
Sinusoidal or honeycomb (Kansas Structural Composites, USA) [14]	Hand lay-up	130	Debonding of top facing	 
Truss-like core				
Triangular (ASSET Fiberline, DK) [10]	Pultrusion	225	Flange + web buckling and delamination	
Rectangular+foam (InfraCore, NL) [15]	VARTM	Variable	Web buckling	
Trapezoidal (DuraSpan Martin Marietta, USA) [10]	Pultrusion	195	Web buckling and delamination	
Hexagonal (Superdeck Creative Pultrusions, USA) [16]	Pultrusion	203	Punching failure and delamination of pultruded shapes	

2.2. Connection methods

According to Zhou and Keller [17], the connection of FRP bridge decks to structural steel girders are system-level connections. Three levels of connections can be distinguished in FRP-steel bridge structures. The first are component-level connections between FRP profiles to form modular deck panels. Secondly, panel-level connections join the modular FRP deck panels to form the entire deck. Finally, system-level connections provide the connection between the entire FRP deck and the underlying girders. Designing system-level joints is a widely studied topic as it is one of the most challenging areas in the development of FRP-steel hybrid bridges. Common techniques of connecting FRP decks to steel girders are mechanical fastening, adhesive bonding or a combination of techniques. An appropriate design and ease of on-site constructability of the connection are important factors for the efficient load transfer from the deck to the supporting structure.

2.2.1. Deck-to-girder connections

Generally, deck-to-girder connections can be divided into concepts with composite action between the FRP deck and steel girders or without. For the case that no composite action is required, the connections should be designed to prevent vertical detaching and lateral movements of the deck. Mechanical fasteners such as traditional bolts and blind fasteners are usually used for this case. A strong advantage of using bolts and blind fasteners is their ease of on-site assembly and disassembly. But on the other hand, these types of connections cause high stress concentrations around the drilled holes of the FRP laminate due to a localised force transfer and only a limited redistribution of stresses as a consequence of delamination.

When composite action is desired in hybrid bridges, the connections are designed to withstand longitudinal shear forces between the deck and girder, vertical detaching and lateral movements of the deck. Often these types of connections are made by means of adhesive bonding or shear studs. As composite action is engaged, extra design efforts have to be made because higher shear forces have to be transferred through the deck-to-girder interface. In the following paragraphs, examples of deck-to-girder connections will be given related to projects.

Bolted fasteners

The use of bolted fasteners is mostly limited to bridges where composite action is not desired. This category of connections can be subdivided into traditional bolts and blind bolts. Due to practical reasons, traditional bolts can only be used having a long shaft penetrating the entire depth of the deck and flange of the girder. Using shorter shafts which only penetrate the bottom FRP facing and girder flange, is not practical since the nut or bolt head inside the panel core can not be accessed after the production. Park *et al.* [18] applied long traditional bolts between a pultruded deck and a steel girder to study the composite behaviour of the system. Temeles and Lesko [19] used a slightly different connection by implementing a steel sleeve around the long shaft which was partially preloaded.

Blind bolts, which only require one side of access, are more frequently used as deck-to-girder connections because they can be easily installed in pre-drilled holes from underneath the bridge. Csillag [1] investigated both experimentally and numerically the static shear resistance of two blind bolt connectors, i.e. M20 8.8 Ajax and Lindapter system. Five push-out tests concluded that the Ajax and Lindapter system provide good ductility (20 mm) due to excessive bearing damage and yielding of the bolts. Ultimate resistances of 207.4 kN and 164.3 kN were found for respectively the Ajax and Lindapter system.

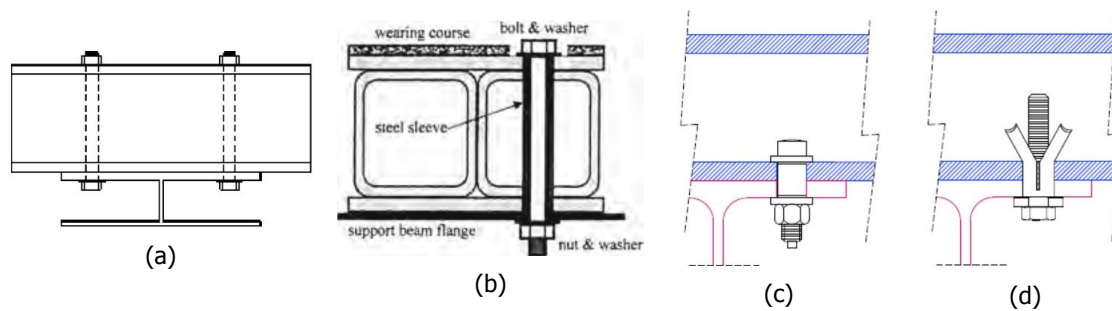


Figure 2.4: Bolted fasteners: long bolt penetrating the entire deck [18] (a) including a steel sleeve [19] (b), the Ajax (c) and Lindapter (d) system [1]

Adhesive bonding

Opposed to discrete bolted fasteners, adhesively-bonded connections can transfer shear forces between the deck and girders smoothly over a large surface resulting in smaller stress concentrations. Although the lightweight adhesives have a high static and fatigue resistance, they are mostly used in combination with mechanical fasteners due to durability concerns. Extreme temperatures and humidity can severely degrade the performance of adhesives. During on-site assembly, the quality control of the bond is limited and loads can be applied only after curing of the adhesive.

Large-scale experiments by Gürtler [10] on adhesively-bonded pultruded FRP bridge deck (ASSET and DuraSpan) to steel girders, have evidenced great static and fatigue performance under four-point bending. For both types of deck full shear load transfer between the deck and girder was achieved. However, Schollmayer [12] showed that the peeling (tensile) stress distribution is non-uniform, having the maxima under the webs of the FRP panel.

In September 2008, the 27 m Friedberg road bridge in Germany opened having an ASSET deck adhesively bonded to two steel main girders. The bridge was completely manufactured in a factory and installed on its foundations in a couple of hours. Three years after completion, Gabler and Knippers [20] reported that the adhesive layers had no signs of degradation.

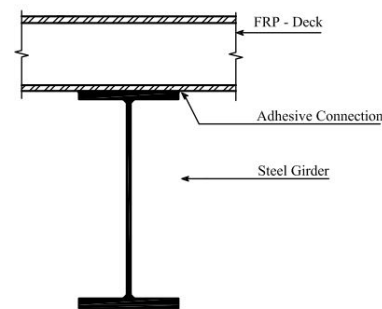


Figure 2.5: Adhesively-bonded connection [10]

Shear-stud connection

The usage of shear studs for FRP decks is closely related to those developed for concrete decks. In this system, shear connectors are pre-installed on the top flange of the steel girder. Afterwards, the FRP deck is placed on top of the girders with cut-outs at the matching locations of the shear connectors. Once the deck is well positioned, the cut-outs are fixed to the shear connector by a non-shrink grout or an exotic fixing mechanism. The cut-outs are localised discrete pockets which could introduce stress concentrations and may be vulnerable for fatigue and environmental exposure. Figure 2.6a displays a typical shear stud connection installed on the S655 road bridge in South Carolina, USA.

Grouted shear stud connections is a common connection technique mainly used in combination with pultruded deck systems. To facilitate the injection of the grout around the pre-welded shear stud, large cut-outs have to be made in the top facing of the deck and foam blocks have to be placed in the core cells to prevent leaking during curing. This makes the installation of grouted shear connections a difficult and time-consuming process. However, grouted shear connections have been used in a couple of road bridges, such as the S655 bridge in South Carolina, USA [21], the Darke County bridge [22] and Fairground bridge [23] in Ohio, USA. Large scale experiments on the 12.6 m Boyer bridge in Pennsylvania, USA with a DuraSpan deck and five steel girders, have concluded that full composite

action was achieved at service loads for a grouted shear stud spacing of 600 mm. [24] Moon *et al.* [25] developed and tested the shear resistance of this type of connection where three shear studs were grouped per cut-out. It was found that the connection had adequate fatigue properties, but the static resistance was 40% less than comparable concrete-steel shear studs. During the tests, delamination of the FRP facing was first observed prior to failure of the shear stud.

To avoid the use of grout, a couple of innovative connections have recently been developed. Davalos *et al.* [26] developed and experimented with a shear stud sleeve-type connection for honeycomb FRP bridge decks. The connection consisted of a threaded stud which was welded to a steel girder. Two steel sleeves are installed in pre-drilled hole in the top and bottom facings which then encloses the shear stud. To clamp the FRP deck, a nut is screwed onto the threaded nut which pulls down the top sleeve. The height of the stud and sleeve can be changed in case the dimensions of the FRP panel differ. The cavity in the top sleeve is filled with a cap or a removable granular material. Shear tests were conducted and concluded that the displacement of the connection is governed by bending of the shear stud. This results in a low initial stiffness until the moment where the shear stud starts bearing in the bottom FRP facing. Due to the low initial stiffness, it was shown that this type of connection could provide partial composite action of 25% and sustain a cyclic fatigue loading equivalent to 75 year bridge service span. [27]

Recently, Csillag [1] expanded the range of shear stud types with a novel, hybrid connector referred to as the injected steel-reinforced resin (iSRR) connector. It consists of a mechanical shear stud which is located in the middle of a cylindrical cut-out in the bottom facing of the FRP deck. The mechanical shear connection is surrounded by steel-reinforced resin (SRR) which fills the cavity inside the FRP deck. The steel-reinforced resin is composed of a lattice of steel shot particles ('reinforcement') embedded in a polymer resin. A strong advantage of this type of connection is the ease of disassembly and potential reusability of the FRP deck. Moreover, static, fatigue and creep experiments, performed by Csillag [1] and Olivier and Csillag [28], showed promising results. In the following section these test results will be further discussed.

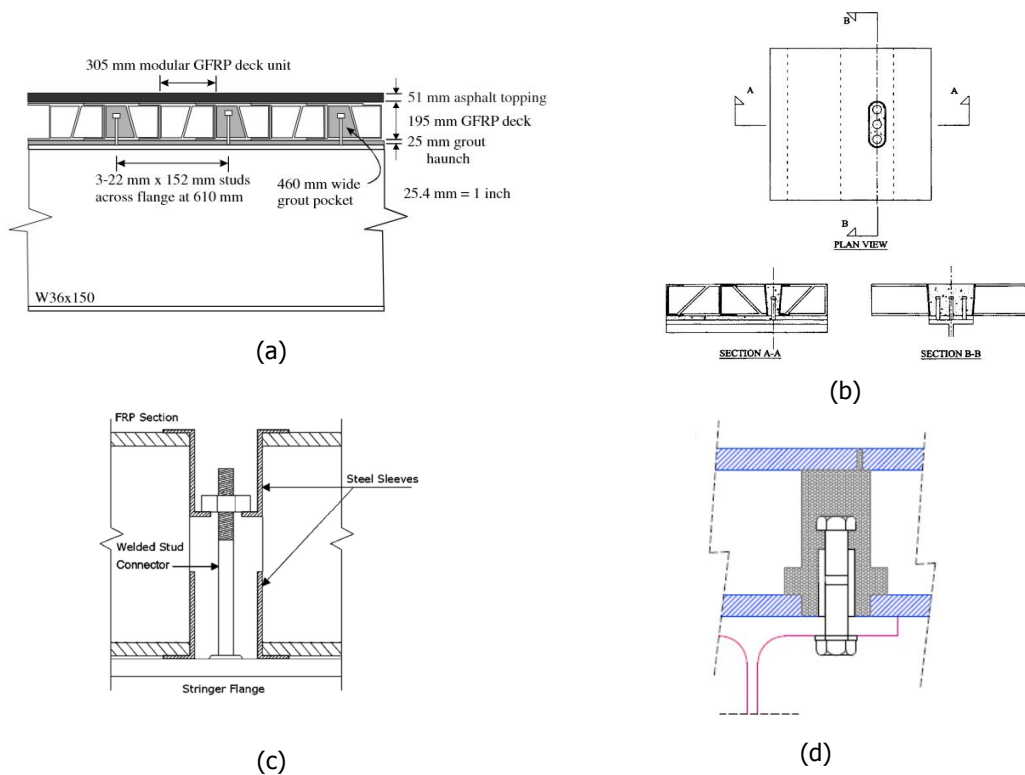


Figure 2.6: Shear studs: Cross-section of S655 bridge [21] (a), grouted shear connection by Moon *et al.* [25] (b), threaded shear stud by Davalos *et al.* [26] (c) and iSRR connector by Csillag [1]

2.2.2. iSRR connector

The use of steel-reinforced resin was firstly explored by M. P. Nijgh [29], who performed steel double lap shear tests with different types of resin injected bolts. The SRR proved to have a 1.5-2 times higher stiffness and 40% reduced creep deformation compared to resin injected connections without steel shots. A recommendation was to explore the application of the SRR in other connections with oversized holes. This led to the concept of using the SRR in FRP-steel connections to reduce stress concentrations in the FRP facings.

Eventually, Csillag [1] and Olivier and Csillag [28] studied the structural performance of the novel iSRR connectors in FRP-steel connections. The first study by Csillag [1], served as a step towards new demountable deck-to-girder connections. The static performance (time-independent behaviour) of three different types of shear connections, including the Ajax and Lindapter connections, was compared by push-out experiments and numerical studies. The shear connectors demonstrated shear resistances ranging from 120 kN to 200 kN, which is comparable to shear stud connectors in hybrid concrete-steel bridges. Compared to the two other blind bolt connections, the iSRR connections showed considerably less slip displacements under low-cycle loading in the initial stage of the push-out tests. This was an indication that the iSRR connection had great potential for applications where a high fatigue endurance is necessary.

The follow-up study by Olivier and Csillag [28] is expanding the scope of the initial study to the time-dependent behaviour (fatigue and creep). Single-lap shear tests were performed on three connector types: Lindapter, iSRR and regular injected bolts. The experimental research concluded that the iSRR connection provided superior structural performance compared to the two other connection types.

Time-independent behaviour

The first series of tests to characterise the static resistance of the iSRR connections was performed by Csillag [1]. In total, three push-out tests (POT) were conducted consisting of two FiberCore FRP panels, a HEB260 steel profile and the four iSRR shear connectors as can be seen in figure 2.7. The FiberCore panels were built-up from 19 mm facings, 8 mm webs with a spacing of 110 mm, and a PU foam core.

For the assembly of the iSRR connections, it was chosen to use a novel type of coupler system. The coupler system was introduced during the REDUCE project on the demountability and reusability of steel-concrete composite structures. The coupler system is composed of two M20 bolts of grade 8.8, an external washer and an M20 coupler having of grade 10.9. The higher bolt grade of the coupler was chosen to ensure that the system failed in the replaceable bolt. Tightening of the bolts was executed with a small amount of torque in order to cease clearances. To accommodate the bearing of the bolt in the hole and eliminate friction between the steel flange and the connector, initial cycling was implemented during the elastic phase where degradation is still insignificant. Subsequently, a displacement controlled loading was applied until failure.

The three iSRR push-out tests resulted in only bolt shear failures at an average shear resistance of 120 kN per connector which was well predicted by the nominal shear resistance of an M20 8.8 bolt. The connectors which remained intact after failure could be removed from the coupler.

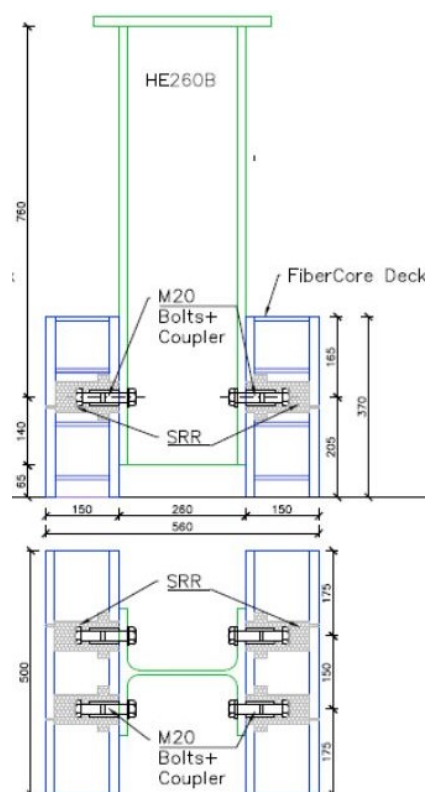


Figure 2.7: iSRR push-out specimen [1]

The large diameter (62 mm) of the hole in the FRP facing resulted in limited damage to the FiberCore panel which proves the reusability of the panel and steel beam in circular structures. The shear failure resulted in a low ductility of 3.2 mm ultimate slip. The averaged load-displacement behaviour of the iSRR push-out tests can be found in figure 2.9.

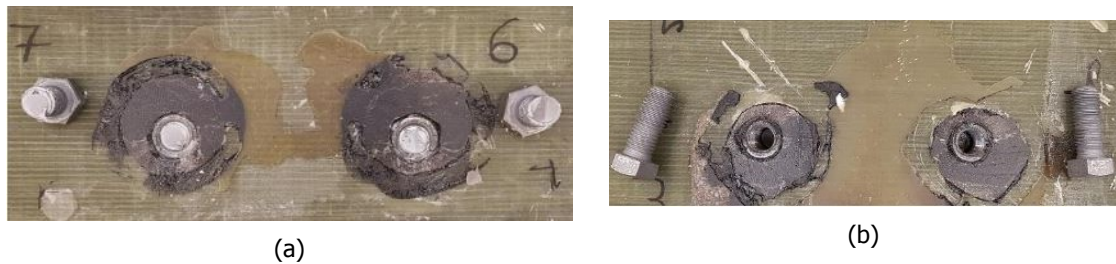


Figure 2.8: Typical pure bolt shear failure (a) and unfastened bolts (b) of the iSRR push-out test [1]

Compared to the steel-concrete shear connections from the REDUCE project which had the same coupler system, the FRP-steel iSRR connection showed nearly identical shear behaviour and initial stiffness of 90 kN/mm. However, a lower shear resistance of 18% was observed.

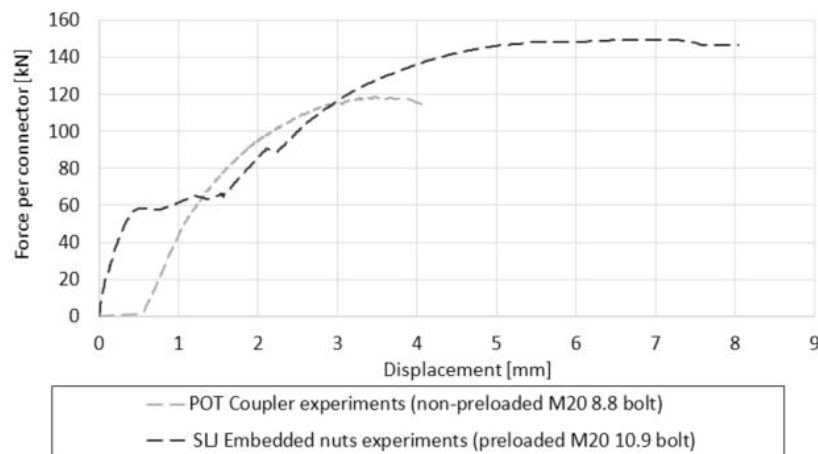


Figure 2.9: Experimental force-displacement curves of the coupler [1] and embedded nuts [28] configuration

Time-dependent behaviour

In order to characterise the time-dependent behaviour, such as fatigue and creep, a second series of experiments was conducted in the form of single-lap joints (SLJ) by Olivier and Csillag [28]. Static, fatigue and creep experiments were performed for three connection types, namely the iSRR connection, Lindapter and regular injection bolts. The iSRR specimens consisted of two 20 mm steel plates connected with two connectors to a 20 mm FRP laminate.

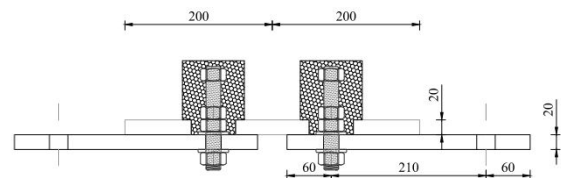


Figure 2.10: iSRR single-lap joint specimen [28]

During the SLJ tests, a different iSRR connection configuration was employed than the coupler system. As research from Pavlovic [30] showed that bolts with embedded nuts offer a similar structural performance as headed studs in steel-concrete structures, it was chosen to use an M20 threaded rod of grade 10.9 which is fixed to the steel flange by washers and nuts. Another difference between the first test series and the second is the preloading of the connection to the steel plate. While during the first

test series [1] preloading was excluded, the second series included full preloading of the connection. In such a way, a slip-resistant connection is obtained suitable for structures where load-reversals are occurring.

The static experiments resulted in only shear failure of the threaded rod at the FRP-steel interface. Due to the high energy release of fracture and the unconstrained condition of the SRR, spalling of the SRR injection piece was observed. Normally, the SRR is surrounded by the foam core of the FRP panel which restricts the SRR from spalling. The four tests resulted in an average ultimate resistance of 154 kN with slip occurring at 60 kN as can be seen from graph 2.9. Despite the brittle shear failure, the connection demonstrated ductile behaviour, having ultimate slip ranges of 7-10 mm.

The creep performance of the iSRR connections was assessed by measuring the displacement of an individual connector under a sustained creep loading of 40 kN during two months. In total, three specimens (six connectors) resulted in an average total displacement of 0.1 mm which was the lowest compared to the Lindapter and injected bolts. After recording two months of creep displacements, the specimens were used to assess the remaining fatigue performance.

To analyse the fatigue performance of the connections, ± 40 kN cyclic loading was applied until a displacement increase of 0.3 mm was achieved. Three experiments were tested under cycling loading only (F-series) whereas three other experiments were loaded under sustained creep loading (C-series) prior to cyclic loading. The specimens from the F- and C-series sustained on average 2.31 and 1.85 million reversed load cycles, respectively. During those cycles, the iSRR connection suffered from a stiffness decrease of 45% due to cyclic loading only and 44% when creep loading was included. This demonstrated that creep has a negligible effect on the fatigue performance of iSRR connector. Compared to the Lindapter and regular injection bolts, the fatigue performance of the iSRR connection was by far superior.

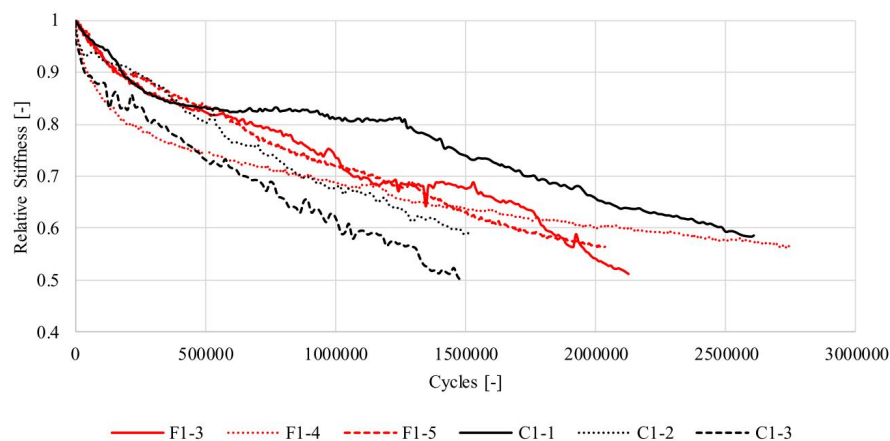


Figure 2.11: Relative stiffness decrease under cyclic loading only (F-series) and combined cyclic+creep loading (C-series) [28]

As the six F- and C-series specimens didn't fail after the cyclic loading test, the remaining static strength of the iSRR connection was assessed. It was concluded that regardless of prior long-term sustained and/or cyclic loading, the iSRR connections reproduced similar static behaviour. The initial linear stage is followed by slipping of the connections at a force level of approximately 60 kN. After slipping the connections start bearing in the steel plate before ultimately shearing off at a ± 150 kN load level.

The study of Olivier and Csillag [28] concluded that the iSRR connections provided superior structural performance compared to Lindapter and injection bolts. With the highest static resistance of 154 kN and a x100 increase on the number of fatigue loading cycles compared to injected bolts, the novel iSRR connector showed great potential as slip-resistant connector for hybrid FRP-steel bridges.

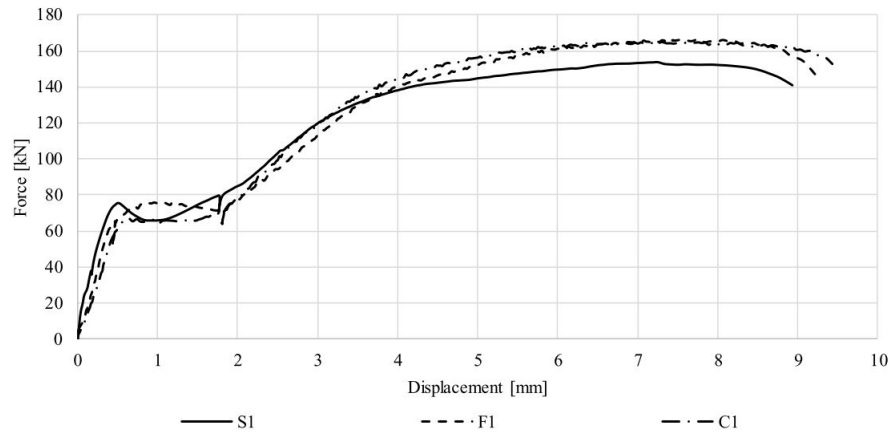


Figure 2.12: Static resistance after production (S1), after cyclic loading (F1) and after creep+cyclic loading (C1) [28]

2.3. FRP-steel composite beams

Conventionally, composite construction was introduced during the 1920s using steel beams and concrete slabs and by the 1950s it was a common construction method for multi-story buildings and bridges. Over the past decades, the interest of replacing the concrete slabs with FRP decks because of their strength-to-weight ratio and durability. Despite the growth in interest, few literature reported the behaviour of FRP-to-steel connections regarding the composite action of the system. One of the obstacles is that the load-bearing behaviour is complicated and hard to describe analytically. Consequentially, the design of the FRP deck and steel girders are carried out conservatively. Two limiting conditions dictate the design: no composite action is regarded when designing the steel girders and full composite action is accounted for the design of FRP deck. [10]

The degree of hybrid interaction, also called the degree of composite action, mainly relies on the structural behaviour of the shear connection joining the components. When using connections which transfer 100% of the shear forces between the deck and the girder, full hybrid interaction is achieved. A system that provides full composite action experiences limited slip at the outer ends of the system and has a continuous strain distribution over the height of the system. Contrarily, zero hybrid interaction is obtained when no shear forces are transferred by the connections. Due to the slipping at the interface, the strain distribution is composed of two linear parts. An intermediate state of partial hybrid interaction exists when the connections partially transfer the shear force.

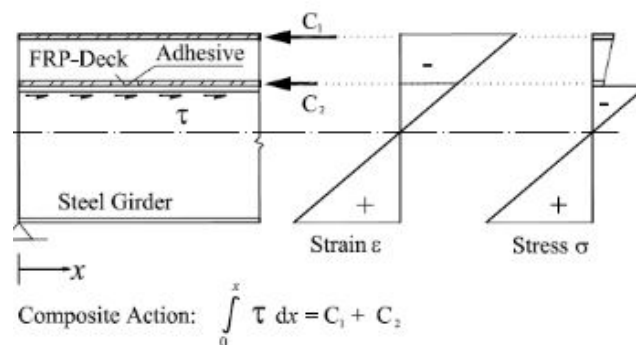


Figure 2.13: Theoretical full hybrid interaction of a composite beam [10]

The primary advantage of including hybrid interaction during the design of composite bridges is that the overall stiffness and resistance can be increased, resulting in a more economical material usage compared to the case without hybrid interaction. Disregarding hybrid interaction, only vertical forces

are transferred from the deck to the steel structure. This means that the load-bearing capacity of the superstructure is dictated by the capacity of the steel members.

2.3.1. FRP-steel composite beam tests

The structural behaviour of composite beams is usually quantified using beam tests under three- or four-point loading conditions. Compared to push-out tests, which characterises the structural behaviour of shear connectors, beam tests predict the real structural performance better. Using full or reduced scale specimens of a composite beam, the stresses and strains can be measured at multiple points on the structure. Main areas of interest are the effective width of the deck, level of hybrid interaction and ultimate resistance. Compared to concrete-steel beams, few researchers have investigated these areas for FRP-steel composite beams. The following paragraphs present chronologically the results from experiments performed in lab conditions.

One of the first to study the behaviour of FRP-steel beam was Gürtler [10] in 2004. Four-point bending tests were performed of a 7.5 m composite beam having an ASSET and DuraSpan deck adhesively bonded to an underlying girder. For both deck types, full composite action was always achieved by the adhesive layer. Normally, a linear strain distribution is expected over the whole beam height as in figure 5.1. However, it was observed that the FRP deck itself provided only partial hybrid interaction due to the limited in-plane shear stiffness of the panels. As discussed in section 2.1, the in-plane shear stiffness of a panel with a trapezoidal (DuraSpan) cross-section geometry is lower than a panel with a triangular (ASSET) cross-section geometry. This is why the upper facing of the DuraSpan deck participated less than the upper facing of the ASSET deck, which is shown in figure 2.14.

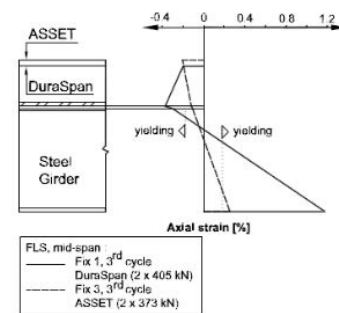


Figure 2.14: Mid-span strain distribution over the composite beam height: DuraSpan VS ASSET [10]

Failure of the composite beam system manifested when the compressed deck detached and buckled between the points of load application. Before the point of failure, tensile yielding was already occurring in the bottom flange of the steel girder. Overall, the hybrid interaction increased the ultimate resistance of the system by 56% and 46% for respectively the DuraSpan and ASSET composite system compared to the resistance of the steel girder alone. The mid-span deflections under SLS loads were also reduced by 23% and 56% in case of the DuraSpan and ASSET decks, respectively. At SLS load levels, the longitudinal strain distribution along the width of the FRP deck was nearly uniformly distributed in contrast to the noticeable shear lag effect at failure.

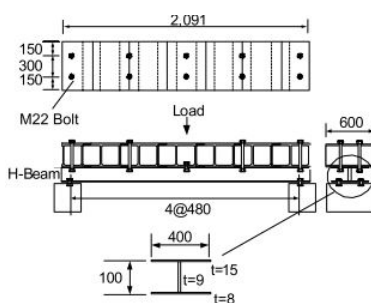


Figure 2.15: Three-point bending specimen from Park *et al.* [18]

In 2006, Park *et al.* [18] performed small-scale three-point bending tests on a composite system having a pultruded cellular FRP deck connected by bolts every 48 cm to a steel girder. The height of the steel girder was chosen to be small compared to the FRP deck in order to allow larger deflections and an easier estimation of the level of hybrid interaction. As the bolted connections (see figure 2.4a) allowed some initial slipping at the FRP-steel interface, an average level of hybrid interaction was measured of 46.1%. The added stiffness of the FRP deck to the system increased the bending stiffness by 25.4% compared to the regular steel beam.

2012 marks the year that Davalos *et al.* [27] performed three-point bending tests on a 1:3 scaled bridge model with a span of 5.5 m. A honeycomb FRP panel with a width of 1.2 m was attached to a steel girder using a prototype shear stud connection as seen in figure 2.6c. Applying a connection spacing of both 600 mm and 1200 mm, a level of hybrid interaction was found of 25% using the prototype connection. Moreover, the novel connection and composite beam were able to sustain a fatigue loading equivalent to a 75 years bridge life span with minimal degradation for static and fatigue tests. The composite beam had linear elastic behaviour until the steel girder started to fail. Eventually, the composite beam failed by local buckling of the steel top-flange. During the experiments, the longitudinal strains of the FRP deck were measured in order to determine the effective width of the deck as 0.63 m which corresponds to a shear lag factor of about 50%.



Figure 2.16: Three-point bending specimen from Davalos *et al.* [27]

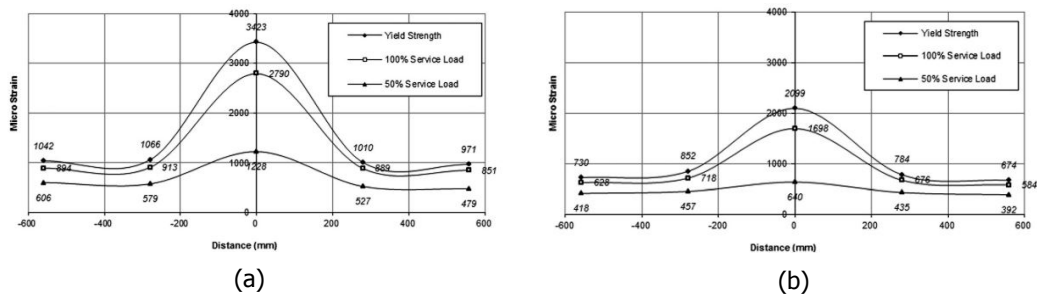


Figure 2.17: Longitudinal strain distribution on the top (a) and bottom (b) facing of the FRP deck [27]

One of the most recent studies on FRP-steel composite beams were conducted by Satasivam [31] in 2012. Under a four-point bending tests, the mechanical performance of modular FRP panels connected by blind bolts to an underlying 2.7 m long steel girder was determined. The FRP deck was composed of pultruded box profiles which were adhesively bonded to the top and bottom facings. The FRP deck was connected to the steel girder by a pair M10 blind bolts every 105 mm which can be seen in figure 2.18b.

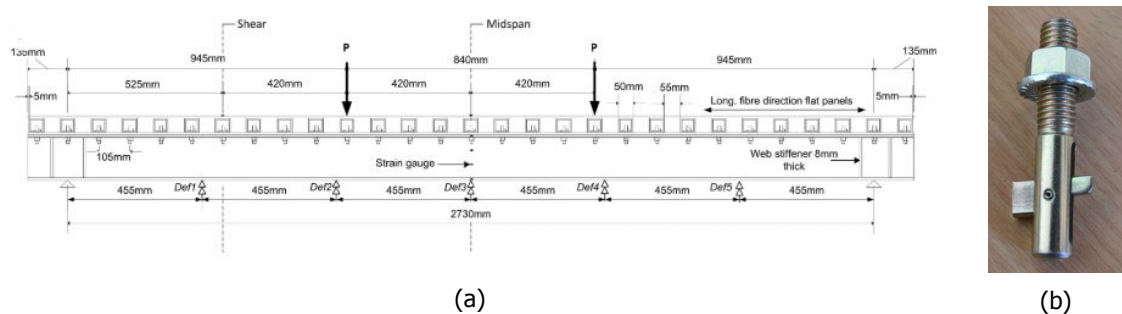


Figure 2.18: Specimen geometry of the FRP-steel composite beam (a) using blind bolts (b) [31]

The experimental results showed that the bending stiffness of the composite beam was increased by 55% compared to the steel girder alone. The specimens showed linear-elastic behaviour followed by a non-linear phase which was initiated by yielding of the steel beam. The load at which yielding was initiated was 20% higher than the steel beam. Prior to yielding, all connections were still intact. Eventually, the composite beam failed when shear stresses became excessively large in the adhesive bond between the box profiles and the facings due to large in-plane shearing of the FRP deck.

As can be seen from figure 2.19b, continuous strains over the height of the composite beam indicate that full composite action was achieved at the FRP-steel interface. However, the composite action offered by the panel itself was different due to the low in-plane shear stiffness of the box rectangular box profiles. This means that the top facing of the panel contributes partially to the overall bending stiffness of the system. This also confirms the findings from Gürtler [10] for the partial composite action of the DuraSpan deck. An average shear lag factor of 0.9 was calculated for the 500 mm wide FRP deck.

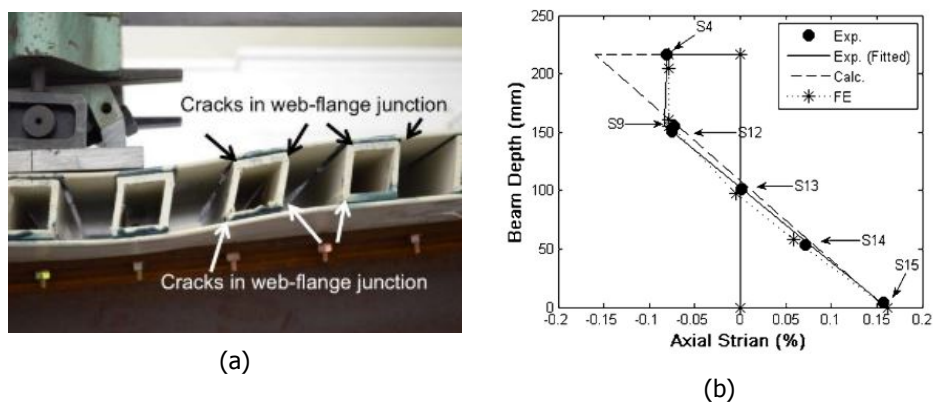


Figure 2.19: Failure (a) and strain distribution along the height of the composite beam (b) [31]

2.3.2. Analytical approximations

Both Gürtler [10] and Satasivam *et al.* [32] proposed analytical methods for the determination of cross-sectional stress-strain distribution and deflections in FRP-steel composite beams. The first method was proposed by Gürtler [10] and was based on the work of Natterer and Hoeft [33]. The second method was based on the "mechanically jointed beam method" from Eurocode 5 and was used by both Gürtler [10] and Satasivam *et al.* [32] to predict the mid-span deflections. While the first method requires the solving of differential equations, the second method is more straightforward. The main difference between the two methods lays in the derivation of the differential equations. The solved equations from the Eurocode can only be applied to single-span beams with sinusoidal loadings. But, they provide also good approximations under linearly distributed loads. As the Eurocode 5 method provided good deflection approximations in both studies, the method is presented below.

The simplified method suggested by Annex B from Eurocode 5 is based on the theory of linear elasticity and the following assumptions [34]:

1. The beams are simply supported with a total span l
2. The individual components of the composite beam are full length or made with glued end joints
3. Mechanical fasteners with a slip modulus K connect the individual components together having a constant spacing s or a spacing that varies uniformly
4. The load is acting in z -direction producing a moment which varies sinusoidally or parabolically

The method is capable of taking into account partial composite action of the shear connectors at the FRP-steel interface. Moreover, the partial composite action of the FRP deck itself due to the weak in-plane stiffness can be considered. Gürtler [10] disregarded the shear stiffness of the adhesive bond during the design process as it provided full composite action. However, when using bolted connections

this might not be the case. Hence, Satasivam *et al.* [32] incorporated the slip surface between the steel girder and bottom facing. This means that Gürtler [10] divided the composite section in two regions while Satasivam *et al.* [32] partitioned the section in three regions.

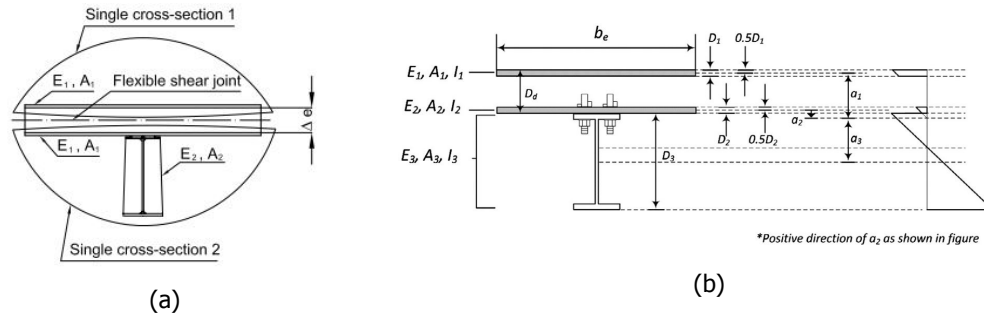


Figure 2.20: Cross-section analysed by Gürtler [10] (a) and Satasivam *et al.* [32] (b)

Following the analogy of Satasivam *et al.* [32], the bending stiffness of the composite beam is calculated using three regions:

$$EI = \sum_{i=1}^3 (E_i I_i + \gamma_i E_i A_i a_i^2)$$

The γ_i factors indicate the degree of composite action provided by the FRP deck itself (γ_1) and by the shear connectors at the FRP-steel interface (γ_3). A $\gamma = 1$ indicates full composite action between the components whereas $\gamma = 0$ implies no composite action. The factors a_i indicate the distance from the geometrical centroid of the component to its neutral axis as can be seen in figure 2.20b.

In order to calculate the partial composite action of the deck itself γ_1 , Gürtler [10] proposed a slight alteration of the normal formula from Eurocode 5:

$$\gamma_1 = \left[1 + \frac{\pi^2 E_1 A_1}{k_d L^2} \right]^{-1}$$

The in-plane stiffness of the deck k_d is calculated by multiplying the normalised in-plane shear stiffness \hat{k} with the effective width of the deck. The normalised in-plane shear stiffness \hat{k} is equivalent to a shear stress τ_{xz} caused by a unit displacement of 1 mm between the top and bottom facings determined by testing or finite element modelling.

$$k_d = \hat{k} b_{eff} = \tau_{xz} b_{eff}$$

As $\gamma_2 = 1$, the last factor γ_3 is calculated as giving in the Eurocode to determine the composite action at the FRP-steel interface:

$$\gamma_3 = \left[1 + \frac{\pi^2 E_3 A_3 s_3}{K_3 L^2} \right]^{-1}$$

Where K_3 is the stiffness modulus of the bolted connections and s_3 indicates the longitudinal distance between the discrete fasteners.

Following the Eurocode 5 method, Satasivam *et al.* [32] calculated a bending stiffness of $2.29 * 10^{12} mm^2$ which corresponded to a 5% difference in mid-span displacement compared to the experimental results. Using the two-region variant of the Eurocode 5 method, analytical calculations for mid-span deflections from Gürtler [10] also showed good agreements with the experimental results for both the DuraSpan and ASSET deck.

2.4. Summary

This chapter reflected on the background of FRP-steel hybrid bridges and its components. Firstly, the performance of different types of FRP decks was evaluated. Secondly, an overview of deck-to-girder connections was presented including the iSRR connections. And finally, the structural behaviour of composite beams was examined. The three main subjects are summarised in the following list:

- The geometry and material properties of an FRP deck can be tailored to serve the needs of the designer. For road bridges, FRP decks with triangular, trapezoidal and rectangular core geometries are the most popular and are produced by pultrusion and vacuum assisted resin transfer molding. The longitudinal stiffnesses of the three core shapes are comparable whereas in transverse direction, the triangular shapes are stiffer. In the stiff longitudinal direction, the decks offer linear elastic behaviour up until brittle failure. The decks behave non-linearly in the weak transverse direction. When loaded in transverse direction, the FRP panels with a trapezoidal and rectangular configuration can dissipate energy during a progressive failure process. This results in a more ductile failure compared to the brittle failure of the triangular configuration.
- Deck-to-girder connections can be categorised into connection types that provide composite action between the FRP deck and steel girders, or neglect composite action. In the case that no composite action is required, mechanical fasteners such as traditional bolts and blind fasteners are usually used. Although their on-site assembly and disassembly is simple and fast, they cause high stress concentrations around the drilled holes of the FRP laminate due to a localised force transfer. Connections that can provide high levels of composite action are shear stud connections and adhesive connections. Recently, the range of shear stud types was expanded by a novel, hybrid connector referred to as the injected steel-reinforced resin (iSRR) connector. The iSRR connector is a slip-resistant demountable shear connection suitable to engage composite action between an FRP deck and steel girder. Two types of iSRR connectors are investigated up-to-date:
 1. The first type includes a coupler which connects two non-preloaded M20 8.8 bolts. Static push-out tests were performed resulting in the rupture of the bolt at an ultimate resistance of 120 kN and an ultimate displacement of 3.2 mm. Minimal bearing damage was found in the FRP laminate which enables the reuse of the FRP panel.
 2. The second type of iSRR connector is composed of a 10.9 M20 threaded rod and nuts which are embedded in the steel-reinforced resin (SRR). The external nut is used to fully preload the connection. Experimental single-lap shear tests were performed to evaluate the static, fatigue and creep performance of this type of iSRR connection. It was shown that creep, had no impact on the fatigue performance of the connector. After a sustained loading of 40 kN during two month, the connector endured the same amount of cycles as a connector which excluded creep loading. Around two million cycles were achieved when a displacement increase of 0.3 mm was measured under a cyclic loading of ± 40 kN. As the specimens did not fail after the creep and fatigue tests, the remaining static strength of the connection was assessed. It was concluded that regardless of prior long-term creep and/or cyclic loading, the iSRR connections reproduced similar static behaviour. Bolt rupture was consistently observed around a failure load of 150 kN and an ultimate displacement of 7-10 mm. The average slip force was 60 kN.
- Compared to concrete-steel beams, few researchers have investigated the structural behaviour of FRP-steel composite beams by lab experiments. A couple of composite beam tests have been performed using traditional mechanical fasteners where slipping at the FRP-steel interface was allowed. The large scatter of design variables between the tests reflected in a large range of test results. Levels of composite action ranged from 25% to 46% and shear lag factors ranged from 50% and 90%. Only one experiment was presented that included a slip-resistant connection between the FRP deck and steel beam by means of adhesion. Full composite action was delivered by the adhesive layer and the stiffness of the system was increased by 23% when an FRP deck with a trapezoidal core geometry was applied.

3

Case study: Beneden Merwede bridge

In order to demonstrate the feasibility of renovating movable highway bridges with FRP deck panels and iSRR connections, a case study bridge is chosen. The objective of this chapter is to firstly introduce the reader to the current state of the case study bridge, and secondly propose the basis for the renovation design.

Movable highway bridges with timber decks have often the same characteristic structural lay-out, and therefore suffer from similar issues. The Dutch highway authority Rijkswaterstaat owns and maintains about 100 movable highway bridges, including 14 bridges with a timber deck. [35] Five of those movable highway bridges with timber decks are being assessed by the engineering company Arup. After consulting the structural plans of these bridges, the main structural dimensions are summarised in table 3.1. Other noticeable bridges from the list of 14 are: Koningsbrug (Harlingen), Kruiswaterbrug (Bolsward), Algerbrug (Krimpen aan den IJssel) and Uitwellingerga-brug (Uitwellingerga).

Table 3.1: Movable highway bridges in the Netherlands with a timber deck (Haringvliet was recently retrofitted with an aluminium deck)

	Unit	Beneden Merwede	Volkerak small	Volkerak big	Haringvliet	Van Brienenoord	Average
Opening year		1967	1965	1965	1964	1965	
Connection road		N3	A29	A29	A29	A16	
# daily vehicle passages		70000	54300	54300	63100	230000	
Deck length	[m]	33	30	30	38	52.6	36.72 m
Deck width	[m]	15	11.5	17.5	25.5	16.75	17.25 m
C.t.c Main-girders	[m]	10	7.2	13.3	16.2	9.4	11.22 m
C.t.c Cross-girders	[m]	4.4	4.6	4.6	4.5	5	4.62 m
C.t.c Secondary girders	[mm]	750	720	700	900	970	808 mm
Height timber planks	[mm]	110	110	110	130	130	118 mm
Height secondary girders	[mm]	360	360	360	290	330	340 mm

The bridge over the Beneden Merwede is a 1032 meter long bridge composed of a 203 m steel tied-arch bridge, a 33 m movable bridge and large concrete approach viaducts. It was opened in 1967 by the province of South-Holland opened with the function to connect Dordrecht to Papendrecht. Later in the 90s, Rijkswaterstaat took over the supervision of the bridge when they decided to elongate the N3 provincial road in order to off-load large vehicles from the Drechtunnels. Being used by 70.000 vehicles daily, the bascule bridge is designed as a class 60/A bridge. Class 60/A is the strongest class for bridges in the Netherlands and is appointed to principal road bridges where road closure should always be avoided.

Like many bascule bridges owned by Rijkswaterstaat, the Beneden Merwede bridge is an excellent example of a typical bascule bridge with a timber deck. The main structural components of the bridge leaf are: two main-girders, eight equally spaced cross-girders, 21 equally spaced secondary girders, timber deck planks and a 426 ton counterweight. When the timber deck and secondary girders are removed, the top flanges of the main-girders and cross-girders are on the same level. The main- and cross-girders are connected by rivets. Appendix A contains drawings of the structural design of the

Beneden Merwede bridge.

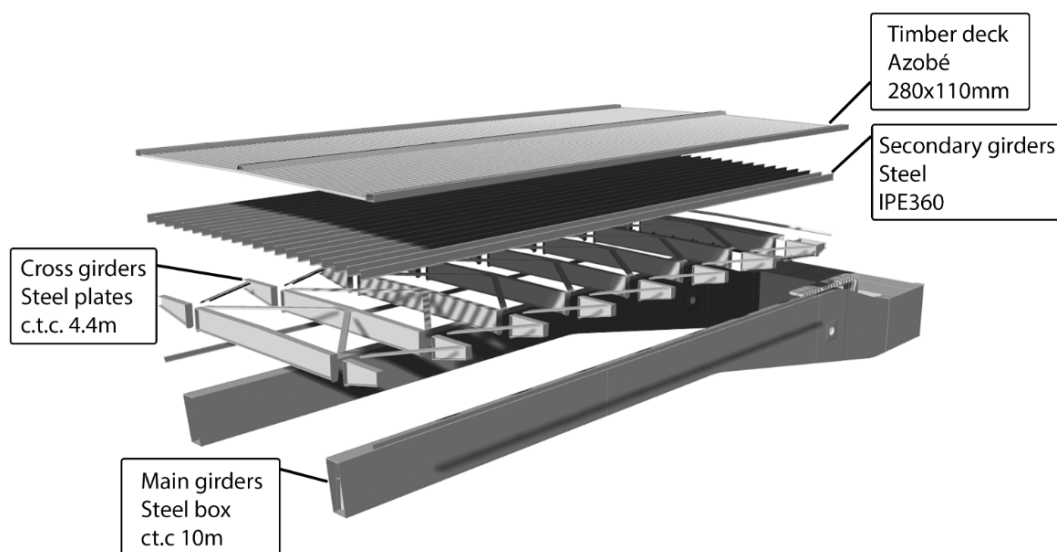


Figure 3.1: Exploded bridge structure of the Beneden Merwede bridge

Recent inspections of the bascule bridge have revealed that the leakage of rain water between the timber planks, is causing the secondary girders to corrode. After determining the remaining strength or effective cross-section of the deteriorate members, the complete bridge was reassessed. Conclusions of the recent inspections and reassessment [36] are:

- **Visual inspection:**

1. **Timber deck:** Across the entire surface of the deck, leakage of water between the timber planks was observed. The dripping water causes corrosion traces on several components of the underlying steel superstructure which are not in direct contact with the timber deck, i.e. wind bracing, cross- and main-girders. Most of the bolted connections between the timber deck and the steel secondary girders are heavily corroded. Although these ± 5000 bolts are retightened annually, some bolts were missing.
2. **Secondary girders:** Over the whole length of the bridge, the top and bottom flange of the secondary girders are heavily corroded as can be seen in figure 3.2. Mainly the top flange has taken its toll over time, resulting in the delamination of the steel. Based on this visual inspection, the top flange thickness was estimated at 50%. Non-destructive testing later found a remaining thickness of 16%.
3. **Cross-girders:** Some corrosion was found at the top and bottom flange near notches where water accumulates.
4. **Main-girders:** Water accumulates around the riveted cross- to main-girder connection causing corrosion of mainly the round rivet heads.

- **Reassessment:**

1. **Static:** The analysis of the remaining static strength of the bridge's cross-sections showed that, apart from the timber deck, all components have sufficient capacity. The timber deck failed in shear under LM2 loadings with a unity check of 2.12. Considering the deck's state, it was advised to take into account the replacement of the deck in the renovation design. When the connections of the bridge were verified, it was found that the yield strength of cross- to main-girder connection was exceeded. This was due to a combination of weak-axis bending and strong-axis bending caused by load cases where permanent and traffic loading were dominant.

2. Fatigue: For some welding details in the bridge, fatigue damages were calculated in 2055. At a couple of cross- to main-girder connections, the weld connecting the bottom flange to the endplate is having minor damages due to weak axis bending of the cross-girders. The weak axis bending of the cross-girders is caused by both traffic loading as the opening cycles of the bridge.
The most problematic fatigue damages were calculated in the secondary girders. These girders, which are welded to the cross-girders and bracing, count a large number of welds which don't meet fatigue requirements. Mainly the welds between the cross- and secondary girders have a critical nature, since they are part of the vertical load-bearing structure.



Figure 3.2: Timber deck to secondary girder connections

Based on the inspections and reassessment of the bridge, it can be concluded that the permeable timber deck and welded secondary girders are not meeting today's standards. Furthermore, the annual retightening of approximately 5000 bolts make it a maintenance expensive deck design. Yet, the bridge's other major components, such as the cross- and main-girders, are in a better condition to fulfil its future service life.

3.1. Renovation design

Considering the design flaws described above, it is proposed to renovate the Beneden Merwede bridge by the replacement of timber deck and secondary girders. These components are substituted by an FRP deck spanning between the cross-girders. This renovation method has several advantages:

- The FRP deck acts as a shell around the structure, protecting the underlying steel girders from environmental effects such as de-icing salts and rainwater.
- By removing the secondary girders, all fatigue issues regarding the welds are eliminated as well.
- The monolithic plate action could reduce weak axis bending of the cross-girders up to 60% as suggested by Klomp [37].
- As other structural components are in adequate condition for their future service life, they will remain in their original state.
- The flexibility of the FRP deck design allows the construction height to match the original road alignment. In such a way the smooth transition between the FRP deck and abutments is secured.

3.1.1. FRP deck & material properties

A vacuum infused sandwich panel with integrated vertical webs is considered for the design. This type of panel is based on FiberCore's Infracore panels described in 2.1. Fibrecore is a well-known FRP deck producer in Europe which has its factory near the Beneden Merwede bridge. A large bridge deck section could be transported 15 km from their production facility in Rotterdam, over the rivers Nieuwe Maas and Noord, to Dordrecht.

The sandwich panel consists of facing and web laminates, both will have a separate layup made from glass fibres and polyester resin. The total height of the new FRP deck is chosen to match the original road profile. This means that the heights of the FRP panel, adhesives and wearing surface sum up to 470 mm. If it was chosen to have a lower cumulative height, the entire leaf of the bridge should be jacked up. This would result in high costs since the bascule chamber and bearings should be adapted for the new alignment. Between the cross-girder flange and the FRP panel, a low-stiffness adhesive will be placed to account for geometrical irregularities. On top of the FRP panel, a flexible heavy-duty wearing surface is glued. Figure 3.3 displays a section of the new FRP decking system supported by the cross-girders.

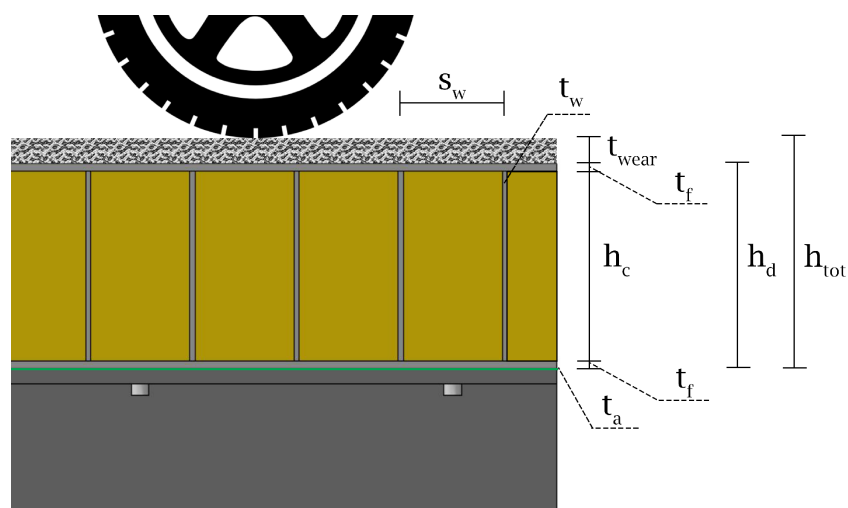


Figure 3.3: Cross-section of the FRP panel

Table 3.2: Geometrical parameter values of figure 3.3

Geometry	Parameter	Value [mm]
Total deck height	h_{tot}	470
FRP panel height	h_d	400
Core height	h_c	360
Web spacing	s_w	120
Facing thickness	t_f	20
Web thickness	t_w	10
Wearing surface thickness	t_{wear}	60
Adhesive thickness	t_a	10

The FRP deck is built-up from mainly three components: the FRP facings and webs, and the foam core. The purpose of these components and corresponding design choice are listed below:

- **Facings:** The structural purpose of the facings is to ensure the transfer of loads in longitudinal direction (0°) between the cross-girders. It is therefore desired to have as many fibres as possible in the 0° -direction. This results in an anisotropic layup. In this case, the standard anisotropic layup ($V_f = 50\%$) according to [38] has been chosen [$0^\circ(55\%) / 90^\circ(15\%) / +45^\circ(15\%) / -45^\circ(15\%)$]. This choice is a result of a recommendation stated in the JRC that in each main direction [$0^\circ / \pm 45^\circ / 90^\circ$] a minimum fibre content of 12.5% must be present. This minimum will ensure that fatigue, creep and impact loads will not have the resin as a sole resisting member. A symmetric lay-up is chosen to prevent torsion in the panel.
- **Webs:** For the webs, the structural purpose is to transfer loads between the top and bottom facings. Since mainly shear stresses are transferred through the webs, a quasi-isotropic laminate is preferable. This results in a lay-up that has the same percentage of fibres in each direction: [$0^\circ(25\%) / 90^\circ(25\%) / +45^\circ(25\%) / -45^\circ(25\%)$].
- **Foam core:** To fill the volume between the webs, a polyurethane (PUR) foam core is used. Although the foam is mainly used during the production of the vacuum infused panels, they also provide some out-of-plane stability to the webs.

Table 3.3 summarises the material properties of the components described above. For the facings and webs, equivalent stiffnesses are calculated according to the classical laminate theory. The thermal coefficients are the result of using a resin with a low coefficient of thermal expansion equal to $\alpha_r = 50 * 10^{-6} K^{-1}$. The x- or 0° -direction denotes the traffic/longitudinal direction while the y- or 90° -direction denotes the transverse direction.

Table 3.3: Stiffness values for facing and web laminates ($V_f = 50\%$)

Material properties	Facings [38]	Webs [38]	PUR foam [8]
$E_x [GPa]$	25.8	18.6	0.0021
$E_y [GPa]$	15.9	18.6	0.0021
$G_{xy} [GPa]$	5.6	7.0	0.000875
ν_{xy}	0.32	0.33	0.2
$\alpha_x [10^{-6} K^{-1}]$	9	11.5	-
$\alpha_y [10^{-6} K^{-1}]$	15	11.5	-
$\rho [kN/m^3]$	18.2	18.2	0.314

Structures made from various materials can be susceptible to thermal loading. The heating of restrained structural components can cause internal stresses due to relative expansion. The coefficient of thermal expansion α is therefore an important thermal property that expresses the amount of material change in dimension per temperature change. Glass fibres and steel have lower coefficients of thermal expansion than polymers like polyester. Accordingly, it can be observed from table 3.3 that the facings have a larger thermal expansion coefficient in the weak α_y direction than in the strong fibre direction

α_x . Compared to steel, which has a coefficient of thermal expansion of $12 * 10^{-6} K^{-1}$, the FRP facings have larger expansions under the same heating. When using slip-resistant connectors, the FRP deck is restrained to the steel superstructure. It is therefore crucial to design the connections in such a way that they can cope with the large forces caused by the differences in expansion.

3.1.2. FRP-to-steel connection design

The literature review given in the previous chapter suggested the high potential of iSRR connectors being used as the binding element between FRP deck panels and steel girders. Subsection 2.2.2 described two different iSRR connection configurations which showed promising static and fatigue results. The first connection configuration had a coupler that was embedded in the SRR and the second configuration had three nuts embedded in the SRR.

It was chosen to investigate the behaviour of the two connection configurations. The configuration with the coupler from Csillag [1] is slightly altered to be comparable with the configuration with the embedded nuts. A internal washer is added and the bolt grade is increased from 8.8 to 10.9. The configurations are visualised in figure 3.4a and 3.4b. In order to engage the FRP deck with the steel superstructure, the connections are preloaded to their full preload force. As both configurations are grade 10.9 and M20, this results in a characteristic preload force of $F_{p,c} = 0.7 * 245 * 1000 = 171.5 kN$. Another reason for preloading the connections is their superior fatigue resistance. In the case of bridge deck connections where large fatigue stress fluctuations are inevitable, preloading is a major advantage. This is because in the case of preloading, the shear forces are transferred through friction and the bolt shaft is solely loaded by the pretension force.

The longitudinal spacing of connectors can have an influence on the resistance and ductility. If connector pairs are positioned too close to each other, they might behave together and lower the individual connector resistance. That's why [39] requires a minimum longitudinal spacing of $5d$ for welded steel-concrete connectors. In the case of the bolted M20 connectors, this would result in a minimum spacing of $5 * 20 mm = 100 mm$. For the maximum spacing of steel-concrete connectors it is assumed that if in the design phase the stability of either the steel or the concrete member is ensured, the spacing shall be sufficiently close. In buildings, this maximum spacing is concretized by a value of 800 mm. Eventually, the longitudinal spacing is set to a centre-to-centre distance of 600 mm. This distance was also chosen for grouted shear stud connections which were used on the Boyer Bridge in Pennsylvania, USA. The 12.6 m bridge was renovated with a DuraSpan FRP deck supported by five steel girders spaced at 1.8 m. Full composite action was achieved at service load levels with longitudinal connector spacing of 600 mm. [24]

3.1.3. Requirements for the FRP-steel connection

In order to apply the proposed FRP-to-steel connections in composite decks, three properties need to be considered: ultimate resistance, stiffness and ductility. As no design codes are available for FRP-steel connections, the nearest codes are the ones for concrete-steel connections. In the following paragraphs the three properties are discussed

The ultimate resistance is one of the least important factors because in order to resist the longitudinal shear forces, a sufficient amount of shear connectors can be applied. For the application of preloaded mechanical shear connections in concrete-steel composite beams, the British Standard [40] gives recommendations for SLS and ULS design of these connections under static loading. The standard states that the longitudinal shear resistance per unit length developed by friction between a concrete slab and a steel beam should be greater than the longitudinal shear force per unit length at SLS. The design frictional resistance developed by each connector at the interface is calculated by $F_s = \frac{\mu * F_{p,c}}{1.1}$ where μ is the friction coefficient which can be taken as 0.35 and $F_{p,c}$ is the preloading force in the bolt. Further, it is assumed that ULS is satisfied with F_s limited by loads for the serviceability load level.

The stiffness of the shear connectors has an influence on the behaviour of the composite beam system. To ensure composite action between the FRP deck and the steel girder, the stiffness of the

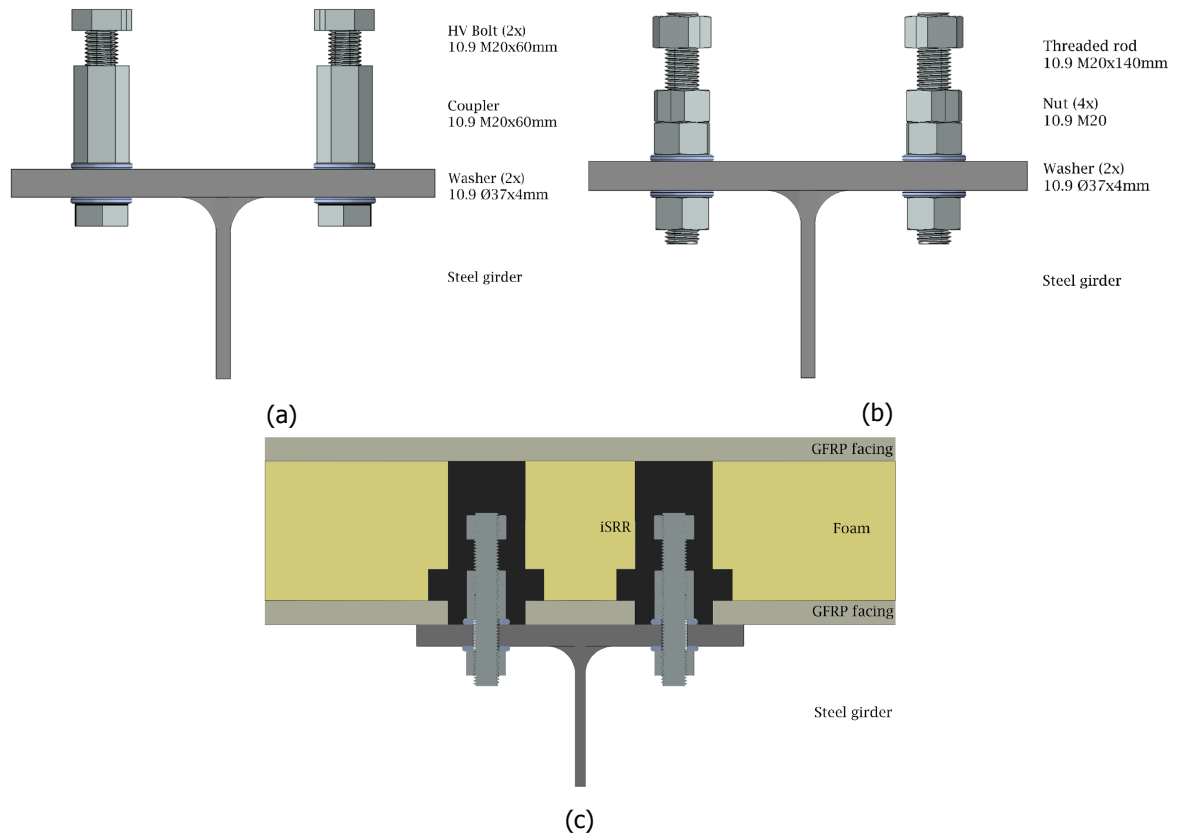


Figure 3.4: Connection configuration with coupler (a) and embedded nuts (b) with FRP deck panel (c)

shear connectors should be sufficiently large to provide a stiff interaction. Unfortunately, design codes do not provide limiting values for stiffness requirements. However, the stiffness of a shear connector is discussed in the appendices of Eurocode 4. [39] The Eurocode states that the stiffness of a shear connector can be approximated by a secant shear connector stiffness $k_{sc} = \frac{0.7 \cdot F_R}{s}$ where F_R is the resistance of the shear connector acquired from push-out tests and s is the slip at $0.7F_R$.

Ductility of the shear connection is important to provide sufficient deformation capacity in order to justify the inelastic redistribution of the longitudinal shear flow between the deck and steel girder. According to Eurocode 4 [39], a shear connector can be described as ductile if the ultimate slip δ_{uk} is greater than 6 mm. When a connector is classified as brittle, e.g. $\delta_{uk} < 6\text{mm}$, their application is limited to cases where only the elastic redistribution of longitudinal shear flow is possible.

3.2. Summary

The aim of this chapter was to present the case study of an existing movable highway bridge. The existing structural design was portrayed together with its design flaws. Based on the present design issues, a renovation design was introduced. The main outcomes of this chapter were:

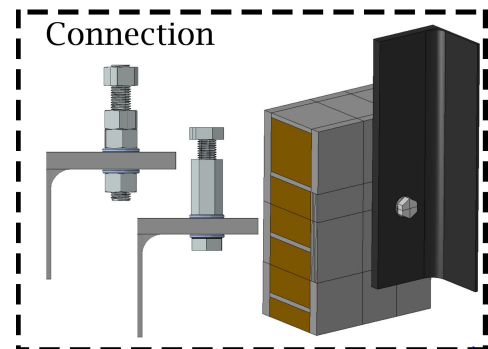
- The Beneden Merwede bridge is an existing highway bascule bridge with a familiar structural layout compared to other bridges with a timber deck. Based on the inspections and reassessment of the bridge, it could be concluded that the permeable timber deck and welded secondary girders are not meeting today's standards. Furthermore, the annual retightening of approximately 5000 bolts makes it a maintenance expensive deck design. Yet, the bridge's other major components, such as the cross- and main-girders, are in a better condition to fulfil its future service life.
- By replacing the timber deck and secondary girders with an FRP deck, the issues with the permeable timber deck and secondary girders are eliminated. The FRP deck acts as a shell around the structure, protecting the underlying steel girders from environmental effects such as de-icing salts and rainwater.
- A vacuum infused FRP deck panel is considered for renovation design. The FRP deck is spanning in longitudinal direction having a top and bottom facing, vertical webs and a foam core. The FRP deck is composed of top and bottom facings with anisotropic properties and a thickness of 20 mm. The 10 mm vertical webs are spaced 120 mm and have quasi-isotropic properties. The properties of FRP are chosen to match the recommendations of the JRC guidelines. [38]
- The FRP deck is attached to the underlying steel structure using a pair of iSRR connections every 600 mm. Two types of iSRR connections are considered: the coupler system and the configurations with embedded nuts. (figures 3.4a and 3.4b) Both configurations are assembled applying preloaded M20 10.9 fasteners. The characterisation of the connection configurations is based on the guidance of Eurocode 4 on processing push-out test results for concrete-steel connections. [39]

4

Connection level

The aim of this chapter is to characterise the performance of the two connection configurations presented in section 3.1.2. In the studies presented in section 2.2.2, the static performance of the two configurations were investigated in different test set-ups (POT vs SLJ) and having different bolt assemblies (non-preloaded M20 8.8 vs preloaded M20 10.9). Based on the results presented in these studies, it is hard to form a recommendation whether the configuration with the coupler or the configuration with the embedded nuts is best suited as an FRP-steel connector. Therefore, the original connection with the coupler from Csillag [1] was altered by increasing the bolt class to 10.9, adding a washer and applying full preloading as presented in section 3.1.2.

In order to compare both connection configurations, detailed finite element models are developed to analyse the connection's stiffness, ductility and ultimate resistance.



The first section of this chapter introduces the reader to the finite element models that were developed in the FEA software Abaqus/Explicit 6.14. In the second section, the results from the analyses are presented and verified. The chapter is finalised by a discussion of the results and the recommendation of the connection configuration which is most suitable for further investigation.

4.1. Modelling technique

A starting point for the modelling techniques used to develop the connection model, are the numerical studies performed by Csillag [1] and Pavlovic [30] on the shear characteristics of FRP-to-steel and concrete-to-steel connectors, respectively. If the reader needs a more detailed background of this model, the aforementioned references can be consulted.

4.1.1. Geometry & boundaries

The FE connection model consists of the same connection components used in the push-out tests performed by Csillag [1]: an FRP sandwich panel, HEB260 steel section, and the components of coupler or embedded nuts connection configuration. The geometry design was slightly altered from the Eurocode 4 recommendations for concrete-steel push-out tests, by halving the number of shear connectors. As the push-out tests are double-symmetric in terms of geometry, constraints and loading, only a quarter of full-scale push-out specimen is modelled.

Nodes of the top steel surface are tied to a reference point where later a displacement-controlled failure loading is applied. The nodes of the bottom side of the FRP sandwich panel are also tied to a reference point that acts as a support. The reaction forces in this point are later used to obtain the force-displacement curves. In order to simulate the lateral restraint of the sandwich panel, which is held together by hollow section connected by threaded rods, an elastic stiffness in y-direction is assigned to the support boundary condition equally to the axial stiffness of the rods.

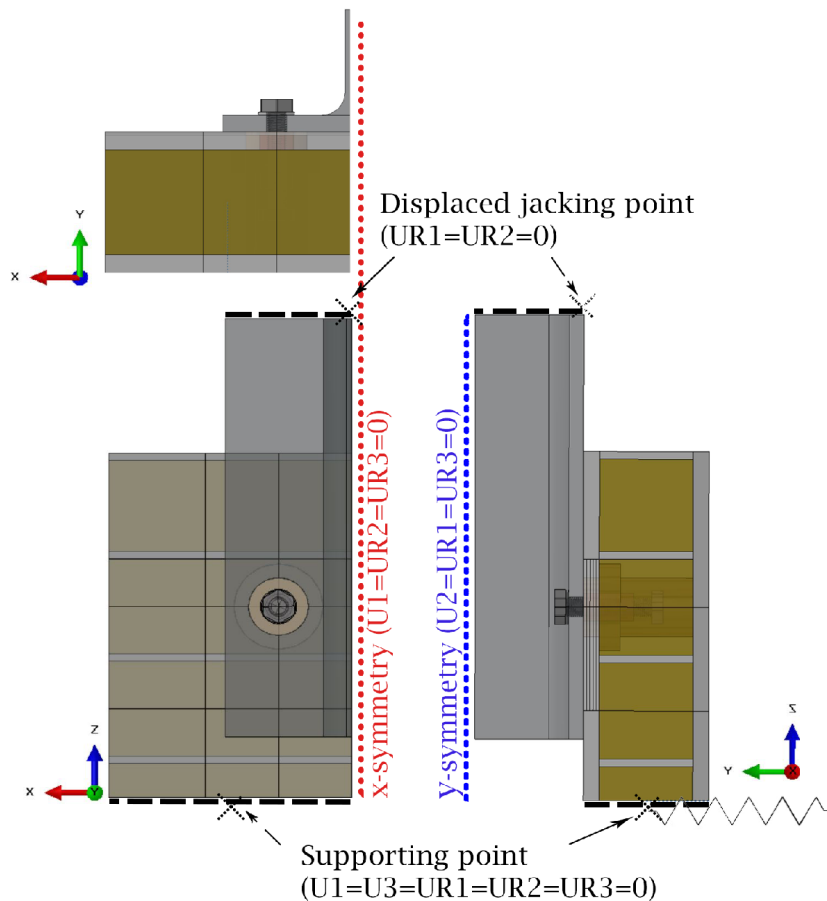


Figure 4.1: Connection model overview with boundary conditions

4.1.2. Mesh & interaction

For the FRP laminates, 2.5D continuum shell elements are used. The facings and the webs of the sandwich panel are modelled using eight-noded quadrilateral continuum shell elements (SC8R) with reduced integration and enhanced hourglass control. In the region around the shear connector where delamination is expected, five continuum shells are stacked through the total thickness of the laminate. In other regions, only one continuum shell element is modelled through the laminate thickness.

For the steel parts, SRR and foam core, 3D solid elements are used. The steel beam is meshed in linear eight-noded brick elements (C3D8R) with reduced integration and hourglass control. The complex geometries of the connector and the SRR, are meshed in four-noded linear tetrahedron elements (C3D4). In the circular region of the SRR, the foam core is meshed using the same elements as the connector and SRR, while outside of that region it's meshed using eight-noded linear brick elements (C3D8R) with reduced integration and hourglass control.

The interaction between surfaces is defined by the general contact interaction procedure in Abaqus/Explicit with normal behaviour (hard formulation) and tangential behaviour (penalty friction formulation). Between the FRP, SRR and steel surfaces a friction coefficient is set to 0.2. [41] For the contact surfaces of the bolt (rod) threads and coupler (nuts), a friction coefficient of 0.14 is used. [30] The contact surfaces of the connector which are compressed due to preloading of the high strength bolts are assigned with a friction coefficient of 0.35. The surfaces between the foam core and other components are tied together as well as the surface of the connector to the SRR.

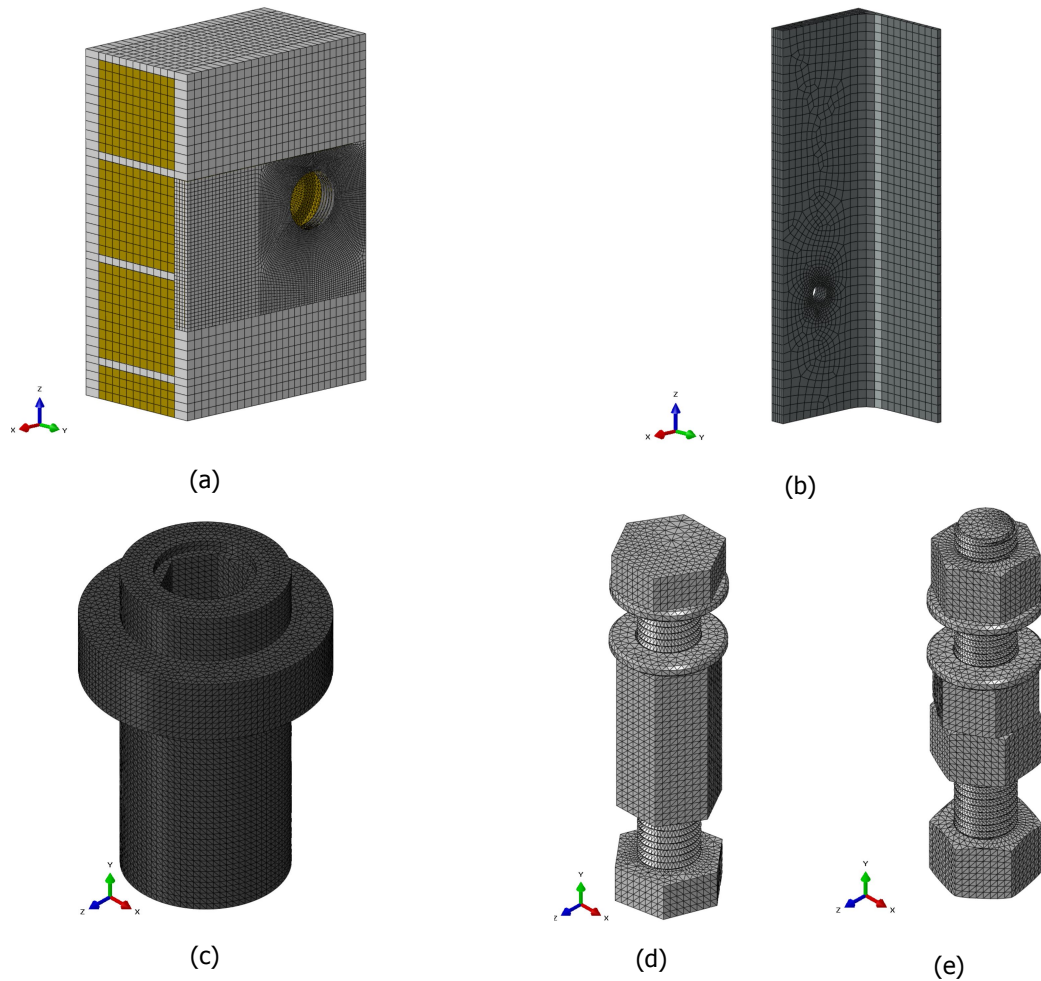


Figure 4.2: Meshing of the FRP panel (a), HEB260 (b), SRR (c), coupler (d) and embedded nuts connector (e)

4.1.3. Loading & Analysis

The loading was defined in two subsequent steps: bolt preloading and failure loading. Both loading steps are displacement controlled and applied under a smooth step function in order to avoid large inertia forces.

The bolt or rod was preloaded by applying a tangential displacement on the bolt head or nut edges. This method is also referred to as the 'turn-of-nut' method. [30] In order to achieve a full preloading force of $F_{p,c} = 170kN$, a tangential displacement of 11.8 mm and 16.5 mm was applied to the bolt head or nut edges, respectively. The preloading torque is counteracted by preventing the tangential displacement on the coupler or embedded nut edges. After preloading, the failure loading step is initiated. A vertical displacement of 8 mm is applied to the top surface of the steel section.

Abaqus/Explicit is used to solve this highly geometric and material nonlinear problem as it does not have convergence issues like the Abaqus/Standard solver. Since the model has a large variety of element sizes, nonuniform semi-automatic mass-scaling is applied on the whole model to prevent large computation times. The time period of the preloading step is set to 20s with a target time increment of 0.005s. For the failure loading step, a time period of 800s is chosen with a target time increment of 0.005s.

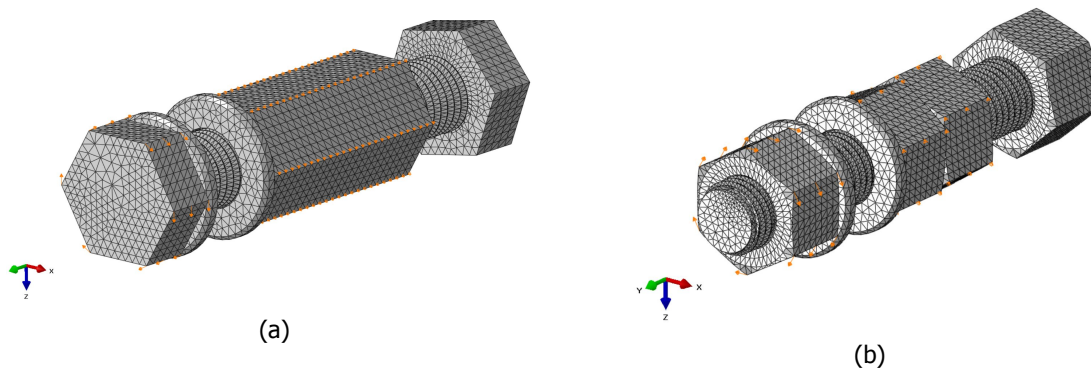


Figure 4.3: Preloading of the coupler (a) and embedded nuts connector (b) by the 'turn-of-nut' method

4.1.4. Material models

In the following paragraphs, the material models used in the connection model are briefly described. In appendix B.1, all material properties are summarised in tables and graphs.

The FRP material models were set to findings of Csillag [1]. Double-lap shear tests were performed to calibrate the linear and non-linear material properties of the FRP laminates. In order to capture the progressive damage of the in-plane ply failure, the Hashin damage model was used. The interaction surface between the stacked 2.5D plies was modelled using cohesive surface interaction modelling.

The steel material models were based on Pavlovic [30]. For the bolts and the steel section, an isotropic plasticity was applied with a initial Young's modulus of 210GPa and a Poisson ratio of 0.3. Based on tensile coupon tests and shear tests, the ductile and shear damage parameters were calibrated for the 10.9 bolts and only ductile damage parameters for the S355 steel section.

The steel-reinforced resin was modelled using the concrete damage plasticity model which matches calibrated parameters of Nijgh *et al.* [42] and Csillag [1]. The latter performed cylinder tests to determine the compression strength and elastic moduli whereas the tensile strength was verified by tensile splitting tests.

The low-density PUR foam was modelled with the crushable foam model including volumetric hardening. The elastic and parameters to define the constitutive relation were taken from the research of Tuwair *et al.* [8] on core alternatives for foam-core sandwich panels.

4.2. Results

4.2.1. Force-displacement behaviour

Figure 4.4 presents the force-displacement curves collected from the FEA analyses on the two connection configurations. The embedded nut model resulted in bolt fracture which was also observed in Olivier and Csillag [28]. Unfortunately, early termination of the coupler model prevents the discovery of the failure mode. The termination of the analysis was caused by the ratio of deformation speed to wave speed that exceeded one in the iSRR.

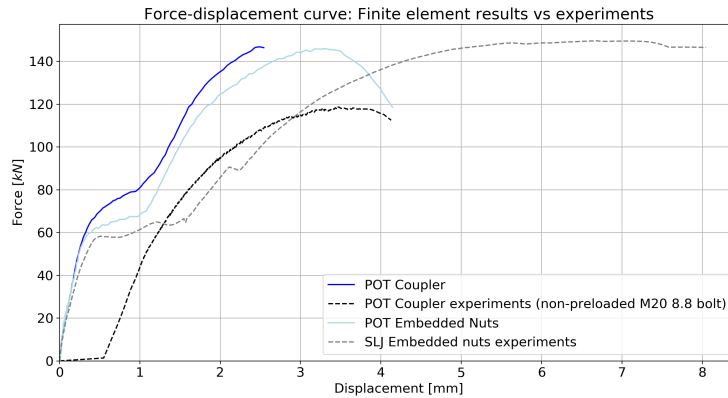


Figure 4.4: Force-displacement curves of the coupler and embedded nuts FEA models compared to the single lap joint (SLJ) experimental results from Olivier and Csillag [28] and push-out tests (POT) from Csillag [1]

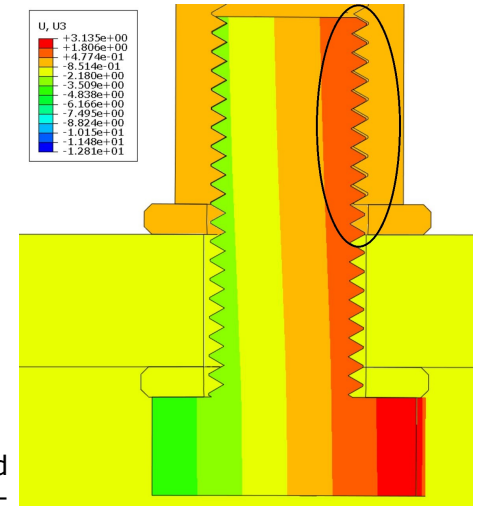


Figure 4.5: Slip of the threads

The force-displacement curves of both configurations can be subdivided into three regions:

1. Linear region (0-0.3 mm): Both configurations showed the same initial stiffness up until a displacement of 0.3 mm. During this displacement, minimal damages are observed as can be seen in appendix B.2.
2. Slip region (0.3-1.1 mm): In this region, the shear force is overcoming the friction resistance. The length of region is equal to the clearance between the bolt thread and hole in the steel flange $\frac{21mm-19.4mm}{2} = 0.8mm$. A distinct difference between the two configurations is that the coupler model shows a gradual change in stiffness whereas the embedded nuts configuration changes more abrupt. This is caused by the slipping in the thread between the preloaded bolt and the coupler. Figure 4.5 shows the gap between the bolt thread and coupler thread which opens gradually during the slipping stage. Appendix B.2 contains figures which depict the damages in the connector at this stage.
3. Non-linear region (1.1 mm+): During this stage, substantial damage of the SRR and bolt takes place as can be seen in figure 4.6 and 4.7. The SRR shows two possible areas of failure: the crushing of the SRR in front of the connector and tension cracking behind the connector. In both analyses, a tensile crack originating from the corner where the SRR cross-section enlarges, grows to the backside of the connector and compression damage is accumulating in front of the connector.

Because of the large hole in the FRP, little bearing damage can be observed for both connection configurations. Minor delamination and FRP shear damage can be located around the compressed edge of the hole.

At the ultimate load of the embedded nuts configuration, the critical value of the ductility damage criterion is reached in the entire cross-section of the rod. This leads to the brittle shear failure of the connector. The configuration with the coupler also exhibits considerable ductile damage but no critical values before termination of the analysis.

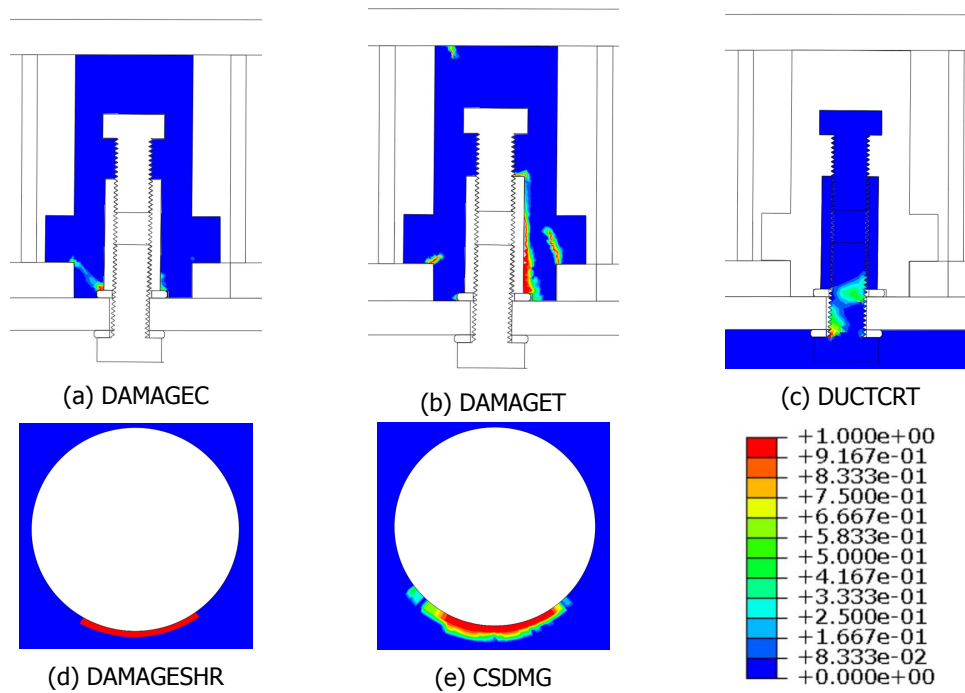


Figure 4.6: Damage indices of the coupler configuration at failure in the following order: SRR compression damage (a), SRR tensile damage (b), ductile damage initiation (c), FRP shear damage (d), FRP contact damage (delamination) (e)

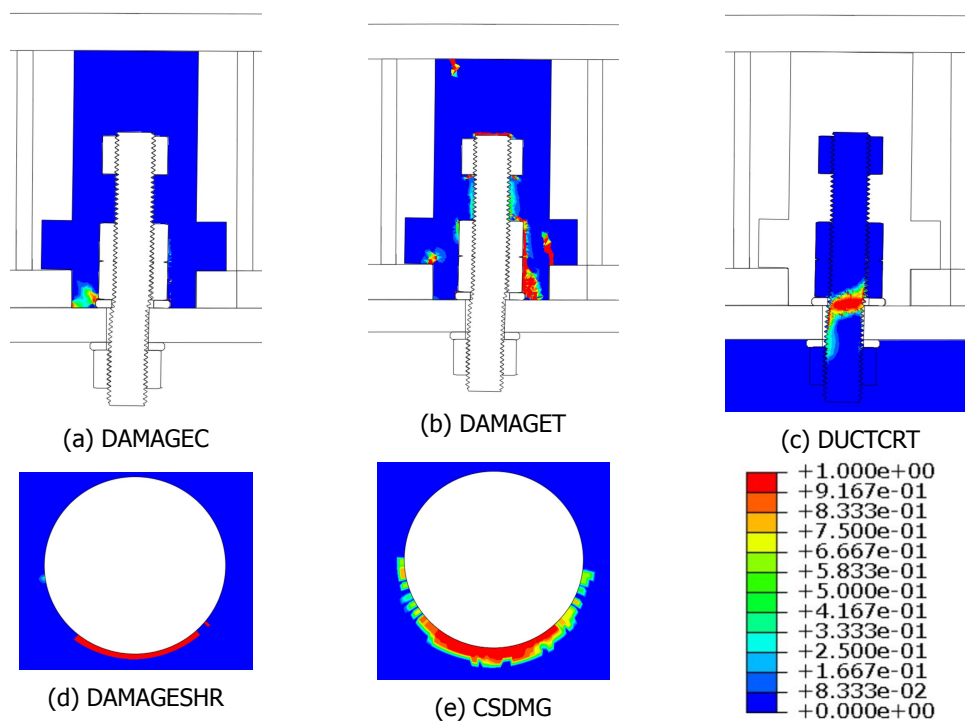


Figure 4.7: Damage indices of the embedded nuts configuration at failure in the following order: SRR compression damage (a), SRR tensile damage (b), ductile damage initiation (c), FRP shear damage (d), FRP contact damage (delamination) (e)

4.2.2. Stiffness & ductility

The numerical push-out tests from the coupler and embedded nuts configurations exhibited a similar initial stiffness as experimental results from Olivier and Csillag [28]. Using the recommendations from Eurocode 4, secant stiffness moduli are determined. A secant stiffness modulus is defined as:

$$k_{sc} = \frac{0.7 * F_R}{s}$$

where F_R is the resistance of the shear connector acquired from push-out tests and s is the slip displacement at $0.7F_R$. As the investigated connections are preloaded bolted connections, a secant stiffness is defined before and after slipping of the connection. Because a higher stiffness leads to a more conservative design of the connectors, the stiffness before slipping is called the upper bound stiffness and it's determined using the slip force F_s . The contrary applies for the stiffness after slipping which is called the lower bound stiffness and is measured using the ultimate force F_v .

- Upper bound stiffness $k_{sc,upper}$: Under service limit state (SLS) load levels this stiffness will be used to determine the deformations of the structure and forces in the bolt. Using this upper bound stiffness, bolt forces need to stay below the slip force F_s which leads to an upper bound design.
- Lower bound stiffness $k_{sc,lower}$: Under ultimate limit state (ULS) load levels, this stiffness is used to determine whether or not the bolt forces exceed the design strength of the shear connection. In reality not all bolts will have slipped at this load level. Some connectors will still have a higher stiffness before slipping and will take more of the shear forces than the connectors that have slipped. It is therefore safe to assume that when all connections have the lower bound stiffness and the connector forces at ULS load levels do not exceed the design strength of the shear connection, the design suffices.

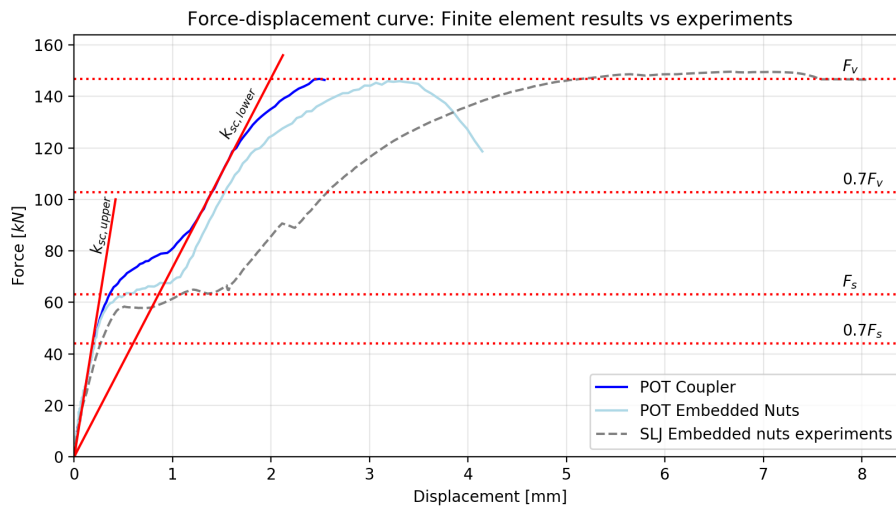


Figure 4.8: Secant stiffness determined according to Eurocode 4 [39] for the FEA of the coupler push-out tests

The FEA analyses demonstrated that the two connection configurations had similar ultimate displacements of 2.5-3.2 mm. The difference with the single lap shear experiments [28], where an ultimate slip of 8 mm was measured, could be explained by the change in test set-up or the model underestimated the ductility. A single lap shear tests induces more out-of-plane effects than a push-out test which could cause a combination of shear and tension. The ultimate slip of the push-out test with the embedded nut configuration (for which the FEA was completed) is similar to the push-out experiments performed by Csillag [1]. According to Eurocode 4, concrete-steel shear connections are classified as brittle when the ultimate slip $\delta_{uk} < 6mm$. This means that the two connection configurations are classified as brittle.

Table 4.1: Secant stiffness corresponding to figure 4.8

Stiffness in [kN/mm]	$k_{sc,upper}$	$k_{sc,lower}$	F_s [kN]	F_v [kN]
POT coupler FEA	221.6	73.6	63.2	146.8
POT embedded nuts FEA	212	67.2	59.8	145.6
SLJ embedded nuts experiments	171.4	40.1	57.6	149.7

4.2.3. Verification

An effort was made to compare the results of the two FEA models with hand calculations and experimental results from Olivier and Csillag [28] and Csillag [1]. Tests from Olivier and Csillag [28] considered single lap shear tests of the preloaded embedded nut configuration whereas tests from Csillag [1] examined push-out tests of the non-preloaded coupler configuration with a 8.8 M20 bolt. This makes the latter experimental results hard to compare. Analytical hand calculations can be found in B.2.

Table 4.2: Distinctive values in force-displacement curves

Property	Unit	FEA Coupler configuration	FEA Embedded nut configuration	SLJ test [28]	Hand calc B.2	POT test [1]
Ultimate shear force	[kN]	146.8	145.6	149.7	147 ($\alpha_v = 0.6$) 122 ($\alpha_v = 0.5$) 142 (pure shear)	120
Ultimate displacement	[mm]	2.5	3.3	8	-	3.2
Slip force	[kN]	63.2	59.8	57.6	60 ($\mu = 0.35$)	-
Slip length	[mm]	0.7	0.7	1.3	-	-
Stiffness	[kN/mm]	221.6	212	171.4	-	89.5

Approximately the same ultimate shear force is achieved for both the coupler and embedded nuts configurations and the experiments from Olivier and Csillag [28]. The experiments and the FEA analysis of the embedded nuts revealed that bolt shear failure was governing. This is confirmed by analytical calculations. The design resistance of bolted shear connectors is not defined in Eurocode 4 [39] for concrete-steel connections. Therefore, Eurocode 3 [43] is consulted to compute the shear resistance of high strength bolts in bolted connections of steel structures. The characteristic shear resistance is calculated by:

$$F_{v,Rk} = \alpha_v f_{ub} A_s$$

For 10.9 M20 connections the stress area $A_s = 245 \text{ mm}^2$, the ultimate stress $f_{ub} = 1000 \text{ MPa}$ and $\alpha_v = 0.5$ is taken. The coefficient $\alpha_v = 0.5$ is based on the statistical evaluation of a large number of tests. For steel grades 4.6, 5.6 and 8.8 a factor of $\alpha_v = 0.6$ is normally taken but it appeared that 10.9 bolts were less ductile and rupture occurred suddenly. Compared to the numerical FEA results, the analytical approximation with a coefficient of $\alpha_v = 0.5$ underestimates the ultimate resistance of the connectors. Using the coefficient $\alpha_v = 0.6$ or the pure shear failure criterion, which is given by $F_v = \frac{1}{\sqrt{3}} f_{ub} A_s = 0.58 f_{ub} A_s$, a better prediction is made.

The slip force from the FEA analyses matched the results from Olivier and Csillag [28] and analytical approximations. Eurocode 3 prescribes the calculation of the characteristic slip force as:

$$F_{s,Rk} = k_s n \mu F_{p,C} = 60 \text{ kN}$$

Where $k_s = 1$ for normal bolt holes, $n = 1$ for one friction plane, $\mu = 0.35$ is determined in tests from Olivier and Csillag [28] and $F_{p,C} = 0.7 f_{ub} A_s = 171.5 \text{ kN}$ is the bolt pretension force.

4.3. Discussion & recommendation

The results presented in the previous chapter showed that both connectors behave alike during the finite element analyses. The slip and failure behaviour were well predicted by the analytical approximations and matched the values from experimental tests by Olivier and Csillag [28]. An aspect which still needs discussion is the ductility and the connection configuration recommendation.

The finite element analyses of both connection types never achieved the ductility limit of 6 mm which characterises them as brittle. This is not in line with the results from the single lap joint (SLJ) tests from Olivier and Csillag [28]. In those tests, the embedded nuts configurations with an M20 10.9 rod failed in shear after an ultimate displacement of ± 8 mm. This is about 2.5x times higher than the initial push-out tests with the M20 8.8 coupler by Csillag [1]. So, the question remains whether the ultimate displacement of the SLJ shear tests would be the same in a push-out test having the embedded nuts configuration or if the finite element analyses underestimated the deformation capacity of the joint. What is certain is that both configurations showed a brittle failure of the bolt with limited damage to the FRP.

To form a recommendation on which connection configuration is best suited to fulfil the slip-resistant joint between an FRP deck and underlying steel girders, practical aspects are also taken into consideration. In the field of bolted shear connectors, the embedded nuts configuration is a widely known and studied connection assembly. The parts needed to compose the assembly are readily available and known to be used under preloaded conditions. On the other hand, the coupler configurations are a novel type of connector which is less studied and only fabricated by limited producers. To the author's knowledge, the static and fatigue behaviour of the coupler under preloaded conditions is yet to be determined by experimental tests.

Because the static performance of the coupler configuration has no significant advantage over the embedded nuts configuration, the practical considerations and the available knowledge of the embedded nuts configuration suggest that it is a safer design choice. This is why for the rest of the study, the iSRR connector with the embedded nuts and an M20 10.9 rod is taken as the reference connector. Moreover, the embedded nuts configuration has proved to have outstanding fatigue and creep behaviour as shown by Olivier and Csillag [28].

For the design procedure of the iSRR connection with the embedded nuts, one should take the upper bound stiffness $k_{sc,upper} = 212 \text{ kN/mm}$ for the serviceability limit state (SLS) design check and take the design slip resistance $F_{s,Rd} = \frac{F_{s,Rk}}{\gamma_{M3,ser}} = \frac{60}{1.1} = 55 \text{ kN}$ as the limit state. In the ultimate limit state (ULS), the lower bound stiffness $k_{sc,lower} = 67 \text{ kN/mm}$ should be taken to check whether the shear forces exceed the design shear resistance $F_{v,Rd} = \frac{F_{v,Rk}}{\gamma_{M2}} = \frac{147}{1.25} = 118 \text{ kN}$. These values are considered during the following chapters.

4.4. Summary

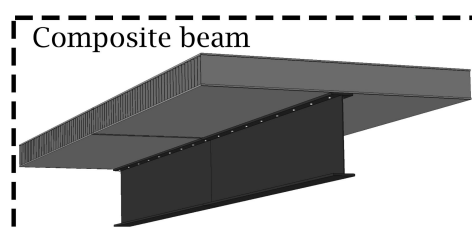
By investigating the proposed connection techniques, this chapter addressed objective 1. Through the finite element modelling of push-out tests, the coupler and embedded nuts connection configurations were characterised and validated. Below, a summary can be found:

- The numerical analysis of the embedded nuts configuration resulted in bolt shear failure at 145.6 kN. At failure, minor damages to the FRP panel were observed which assures the reuse of the FRP panel in a next life-cycle. The analysis of the coupler configuration resulted in an early termination and therefore the ultimate resistance can only be speculated. Prominent ductile damages in the bolt suggested that the coupler system was on the verge of bolt shear failure around 146.8 kN.
- The slip behaviour of the preloaded coupler and embedded nuts connection configurations was well simulated having a slip force of 63.2 kN and 59.2 kN, respectively. While the embedded nuts configuration exhibited clear slipping at the flange-washer interface, the slipping of the coupler configuration coincided with the slipping of the bolt thread within the coupler. This resulted in a less apparent slip plateau on the force-displacement curves of the coupler configuration.
- The two connection configurations had a similar ultimate displacement of 2.5-3.2 mm. Because the ultimate slip the ultimate displacement is smaller than six millimetres, both configurations are classified as brittle according to Eurocode 4. [39]
- The ultimate resistance of both connection configurations was in accordance with results from Olivier and Csillag [28] and analytical approximations using the α_v coefficient of 0.6 or the pure shear criterion. The slip force was also in agreement with results from Olivier and Csillag [28] and hand calculations.
- Because the static performance of the coupler configuration had no significant advantage over the embedded nuts configuration, it was advised to use the iSRR connection with the embedded nuts as a safe design choice. In the field of bolted shear connectors, the embedded nuts configuration is a widely known and studied connection assembly. The parts needed to compose the assembly are readily available and known to be used under preloaded conditions. Moreover, the embedded nuts configuration proved to have outstanding fatigue and creep behaviour during the experiments of Olivier and Csillag [28].
- For the design procedure of the iSRR connection with the embedded nuts, two secant stiffness moduli were defined:
 1. The stiffness before slipping is called the upper bound stiffness $k_{sc,upper}$ and will be used under service limit state (SLS) load levels to determine the deformations of the structure and forces in the bolt. In SLS, the upper bound stiffness $k_{sc,upper} = 212 \text{ kN/mm}$ should be used to check whether shear forces exceed the design slip resistance $F_{s,Rd} = \frac{F_{s,Rk}}{\gamma_{M3,ser}} = \frac{60}{1.1} = 55 \text{ kN}$.
 2. After slipping the stiffness is called the lower bound stiffness $k_{sc,lower}$ and will be used under ultimate limit state (ULS) load levels to determine whether or not the bolt forces exceed the design strength of the shear connection. In ULS, the lower bound stiffness $k_{sc,lower} = 67 \text{ kN/mm}$ should be taken to check whether the shear forces exceed the design shear resistance $F_{v,Rd} = \frac{F_{v,Rk}}{\gamma_{M2}} = \frac{147}{1.25} = 118 \text{ kN}$.

5

Composite beam level

This chapter investigates the mechanical performance of FRP-steel composite beams, forming the second numerical analysis level. In order to study the composite behaviour of the hybrid FRP-steel deck system (objective 2) and appropriate modelling techniques (objective 3), a composite beam model is made. The geometry of the system is representative to the dimensions of the existing steel structure from the Beneden Merwede bridge and the proposed renovation design which was presented in chapter 3.



Like in the previous chapter, the first section presents the modelling techniques used to create the composite beam model. But in order to apply the iSRR connection described in chapter 4 on the medium-scale composite beam model, the modelling techniques of the iSRR connector had to be simplified. Those simplifications of the FRP-steel connection are discussed in section 5.2.

Section 5.3 presents the results from the finite element analysis together with the analytical verification. Afterwards, the modelling techniques of the composite beam model are further simplified in section 5.4. In this section, the results from the detailed composite beam model presented in section 5.3 are compared with more user friendly and computational inexpensive modelling techniques. Finally, the chapter is concluded in section 5.5 with a discussion of the composite action, effective width and connector spacing.

5.1. Modelling technique

5.1.1. Geometry & boundaries

The 10 meter distance between the main-girders of the Beneden Merwede bridge is chosen to be the system length. One cross-girder is modelled which is connected to the deck panel having a width equal to the centre-to-centre distance of the cross-girders. This enables the use of symmetry to reduce the size of the model. The foam core is neglected in this analysis since it has a minimal influence on the results. (Appendix C.1)

The steel beam is simply supported in its centre of gravity by tying the end nodes of the steel section to a reference point at each end of the cross-girder. The vertical forces in these reference points are measured to back-calculate the applied pressure during the analysis ($q = \frac{2 \cdot R_y}{B \cdot L}$). The FRP deck panel is not supported at the support ends. As the longest edge of the deck panel is located at mid-span between two cross-girders and the loading conditions are symmetrical, symmetry boundary conditions are applied to prevent lateral displacements and rotations. The longitudinal direction of this model is denoted as the axial direction of the steel beam. The transverse direction is orthogonal to the span of the steel beam.

Table 5.1: Geometry parameters

Property	Symbol	Unit	Value
Length	L	[m]	10
Width deck	B	[m]	4.4
Steel flange width	$b_{f,a}$	[mm]	350
Steel flange thickness	$t_{f,a}$	[mm]	30
Steel web height	$h_{w,a}$	[mm]	1000
Steel web thickness	$t_{w,a}$	[mm]	14
FRP panel height	h	[mm]	400
FRP facing thickness	t_f	[mm]	20
FRP web thickness	t_w	[mm]	10
FRP web spacing	s_w	[mm]	120
Connector spacing	c_w	[mm]	600

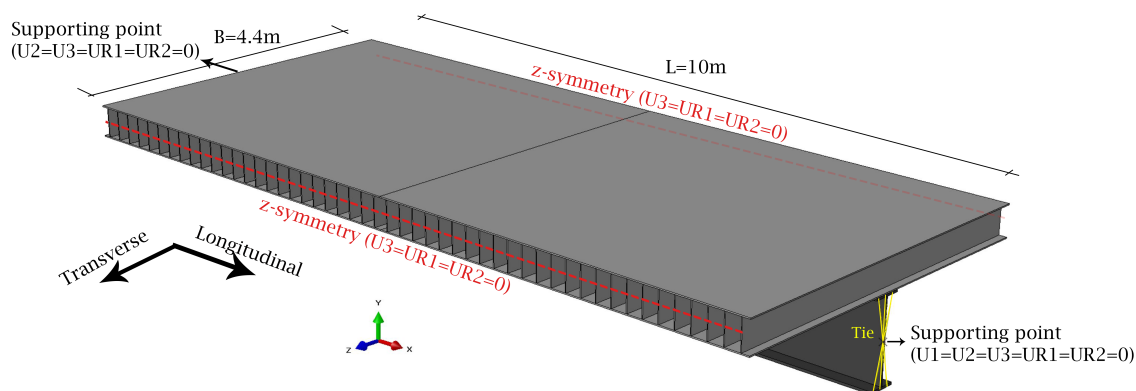


Figure 5.1: Composite beam model overview with boundary conditions

5.1.2. Mesh & interaction

In this model, all plate-like surfaces of the FRP panel and steel beam are modelled with eight-noded SC8R continuum shell elements since they allow two-sided surface interaction. For these elements, reduced integration and hourglass control is enabled. The target element size for the steel beam and the FRP panel are 20 mm and 30 mm, respectively. Rounded edges of holes in the FRP panel have a local element size of 5 mm and the elements near holes in the steel beam have an approximate size of 3 mm. The meshing of the connectors will be described in section 5.2.

The interaction between FRP-to-steel surfaces is defined by the general contact interaction procedure in Abaqus/Explicit with normal behaviour (hard formulation) and tangential behaviour (penalty friction formulation). A global property is assigned with a friction coefficient of 0.2. [41]

5.1.3. Loading & analysis

Loading of the models is done in two subsequent steps: bolt preloading and failure loading. The preloading step is elaborated in section 5.2. The failure loading step involves a force-controlled pressure loading which is applied on top of the FRP deck. The uniformly distributed pressure loading is increased under a smooth step function until a value of $300\text{kN}/\text{m}^2$.

Abaqus/Explicit is used to solve this large non-linear model. Since the model has a large variety of element sizes, nonuniform semi-automatic mass-scaling is applied on the whole model to prevent large computation times. The time period of the preloading step is set to 20s with a target time increment of 0.005s. For the failure loading step, a time period of 800s is chosen with a target time increment of 0.005s.

5.1.4. Material models

Since the analyses in chapter 4 have shown that the FRP undergoes minimal damage, only elastic properties were assigned to the FRP. Table 3.3 shows the properties of the facings and the webs according to the JRC [38].

In case of the steel beam, ductile damage is included because the bottom flange can yield before failure of the connectors. The plasticity curve (figure B.1) was built based on the elastic constants and plastic strain curve for S355 steel. The material models of the connectors will be discussed in the next section.

5.2. FRP-to-steel interaction

In order to apply the iSRR connection described in chapter 4 on the large-scale composite beam model, some simplifications were made to the connection model. The modelling techniques and geometry of the steel beam and FRP panel which were outlined in the previous subsection, are used to model a push-out test that will be compared to results from chapter 4.

Several simplifications of the modelling techniques discussed in chapter 4 had no influences on the results but decreased the computation time significantly from four hours to 25min. Step-by-step the connection model with the coupler configuration was simplified and force-displacement curves were compared. (see appendix C.2) The following simplifications had no effect on the force-displacement curves and damage progression:

1. Removal of the foam: the low stiffness of the foam material didn't contribute to the stiffness of the connection. By removing the foam material, many elements are spared which led to a significant decrease in computation time.
2. FRP modelling: As minor delamination damages to the FRP were apparent from the FEA analyses in chapter 4, the 2.5D stacked plies approach and the Hashin damage criterion were replaced by a single ply with elastic properties.
3. Steel section elements: The solid eight-noded brick elements (C3D8R) were replaced by eight-noded continuum shell elements with reduced integration and hourglass control. These elements still allow two-sided surface interaction which is needed for the preloading.
4. Mesh size: The fine mesh is enlarged to sizes equivalent to the composite beam model without compromising quality and stability of the results.

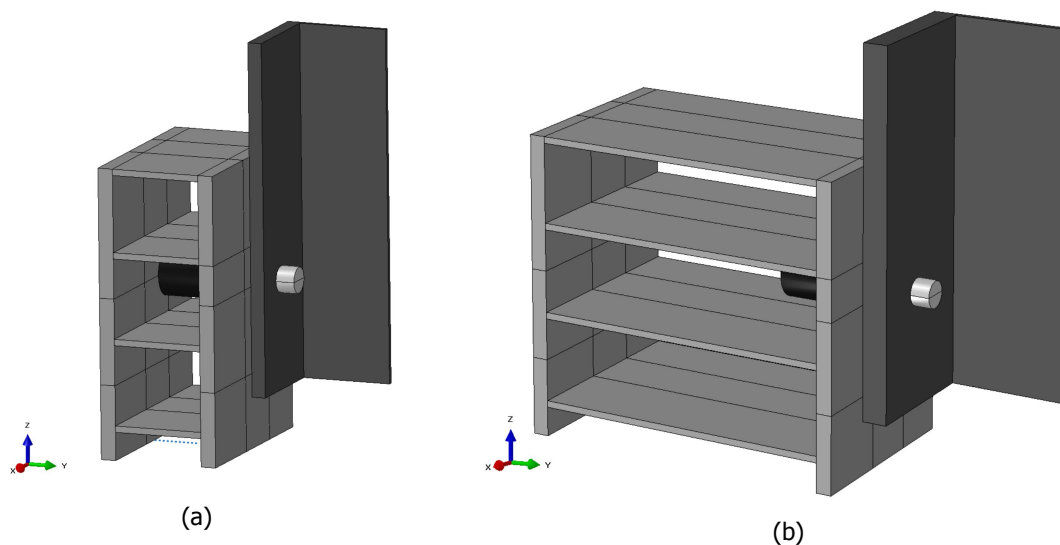


Figure 5.2: Simplified connection overview with the geometry of the push-out tests by Csillag [1] discussed in chapter 4 (a) and the composite beam geometry (b)

After modelling simplifications from the previous list were applied, the geometry of the coupler or embedded nuts connector configuration was replaced by a solid bolt mass as can be seen in figure 5.3. This solid bolt is composed of two cylindrical sections which represent firstly the bolt heads, nuts, coupler and washers, and secondly the bolt thread or rod. The diameter of the largest cylinders $\varnothing = 33mm$ are chosen to have an equivalent surface area as the hexagonal bolt head or nut. The diameter of the cylinder which replaces the threads is set to the diameter of the shear stress area of M20 bolts, i.e. $\varnothing = 18mm$.

As the hole clearance between the steel section and the solid bolt enlarges due to absence of a thread, the diameter of the hole in the steel flange is reduced to $\varnothing = 19.6mm$. This makes the hole

clearance equal to the clearance of the connection model in chapter 4.

Full preloading of the solid bolt is achieved by applying a uniaxial thermal strain to the solid bolt shank at the location depicted in figure 5.3c. The solid bolt is therefore assigned with orthotropic linear thermal expansion coefficients which are only non-zero in the axial direction of the bolt.

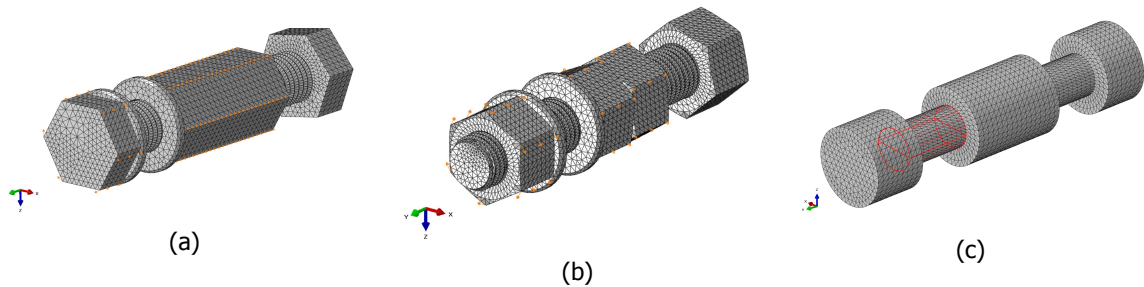


Figure 5.3: The coupler (a) and embedded nuts connector (b) compared to the solid bolt connector with the region of uniaxial thermal strain preloading (c)

The previously described simplifications of the connection model result in the geometry which can be seen in figure 5.2a. At this point, the geometry of the FRP panel and the steel beam are equal to the simplifications which had no effect on the results. Initially, the contact surfaces of the connector and steel beam which are compressed due to preloading of the high strength bolts, were assigned with a friction coefficient $\mu = 0.35$ like in the models of chapter 4. But as can be seen from graph 5.4, the slip force was overestimated by 66% using the solid bolt connector. It was therefore chosen to lower the friction coefficient to $\frac{60}{100} * 0.35 \approx 0.2$. The reason for the increase in slip force is the reduction in slip planes and change in friction surface topology. By lowering the friction coefficient to 0.2, the ultimate force and the slip behaviour are well approximated compared to the detailed connection models from chapter 4. A slip factor $\alpha_{slip} = \frac{0.2}{0.35} = 0.6$ is introduced.

Although the initial stiffness is well approximated, the reduction of the friction coefficient causes the connection to be less stiff around slipping. Approaching the ultimate load, significant shear damage is spreading through the solid bolt shank which eventually leads to the shear failure of the solid bolt.

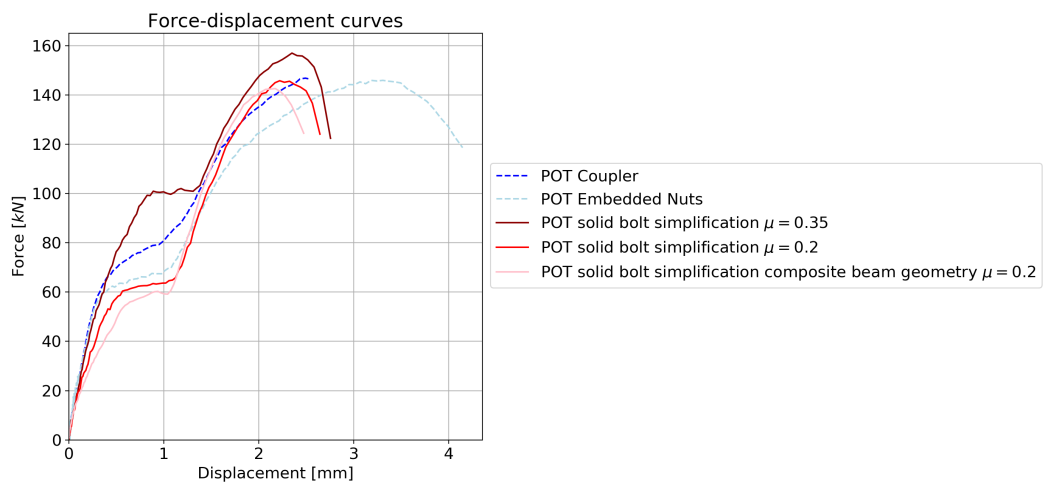


Figure 5.4: Force-displacement curves for connection models presented in chapter 4 and the simplified models of figures 5.2a and 5.2b

The last step of the simplification is the adaptation of the composite beam geometry as depicted in

figure 5.2b. A major difference in this case is the increase in thickness of the steel flange from 20 mm to 30 mm and the height of the FRP panel from 150 mm to 400 mm. The force-displacement curve at this stage of the simplifications is also plotted in graph 5.4. Until 20 kN, the stiffnesses of all models are equivalent. A possible explanation for the lower stiffness before slipping could be the increased shaft length of the solid bolt with composite beam geometry. The slip force and slip length are rather similar to the other models. When the force picks up again, due to bearing of the shank in the steel flange, similar behaviour is found as the solid bolt model with the smaller geometry of figure 5.2a. Eventually, the model fails in bolt shear failure which can also be observed in the other models.

Table 5.2: Distinctive values in force-displacement curves for connection simplification steps

Property	Unit	FEA Coupler configuration	FEA Embedded nut configuration	POT solid bolt ($\mu = 0.2$)	POT solid bolt ($\mu = 0.2$) deck geometry
Ultimate shear force	[kN]	146.8	145.6	145.5	143
Ultimate displacement	[mm]	2.5	3.3	2.5	2.4
Slip force	[kN]	63.2	59.8	59.4	58.1
$k_{sc,upper}$	[kN/mm]	221.6	212	157	136
$k_{sc,lower}$	[kN/mm]	73.6	67.2	69	73

The range of simplifications described above has led to the chosen modelling technique of the FRP-to-steel connection in the composite beam model. Having a connector spacing of 600 mm, a total of 34 solid bolt connectors have been modelled. The material models of the SRR and the solid bolt are equal to the materials models used in section 4. The remaining part of the composite beam model is modelled by using the modelling techniques described in section 5.1.

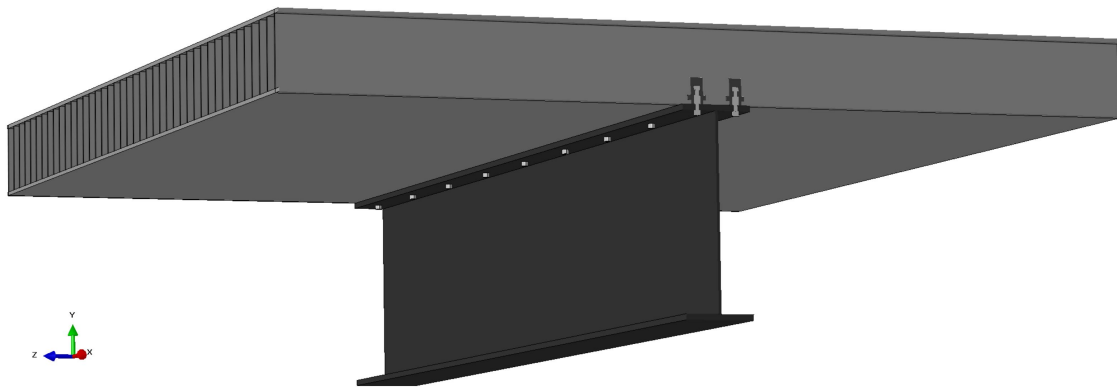


Figure 5.5: Cross-section of the composite beam model at mid-span

5.3. Results

5.3.1. Force-displacement behaviour

Graph 5.6 plots the increasing pressure on the top-facing against the mid-span displacement of the composite beam. The plot also includes the results from an analysis where only a steel reference beam was modelled with a pressure loading on its top flange. The steel reference beam has identical properties as the steel beam in the composite beam model. Appendix C.3 elaborates more details about the steel beam model.

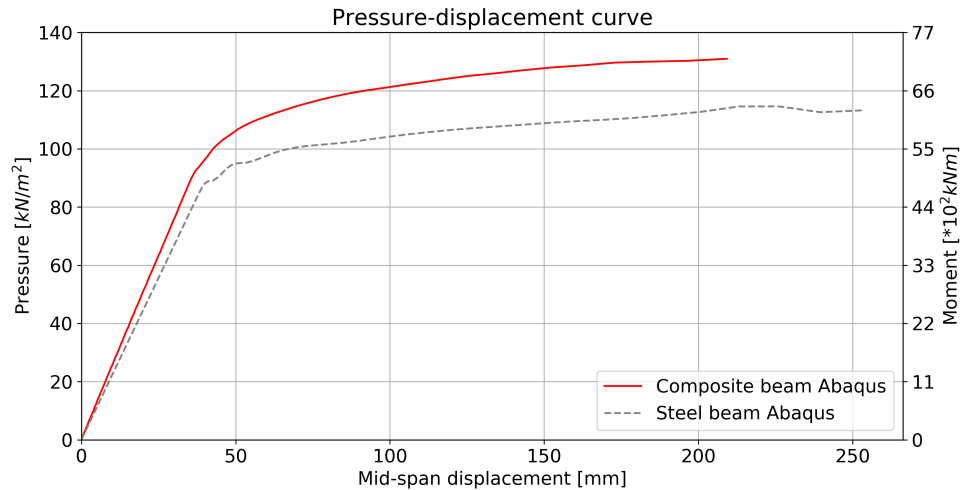


Figure 5.6: Pressure-displacement graph of the composite beam model and steel beam model

By comparing the slopes of the pressure-displacement curves in the linear-elastic phase, it can be observed that the stiffness increase of the composite system is slightly higher compared to the performance of the steel beam alone. To compare the two models, the bending stiffness EI_m is calculated at a pressure of $q = 10\text{kN/m}^2$ for both models using simple beam theory and ignoring shear deformation:

$$EI_m = \frac{5}{384} \frac{q b_{deck} L^4}{w}$$

Table 5.3: Bending stiffness EI_m comparison at $q = 10\text{kN/m}^2$

	$w[\text{mm}]$	$L[\text{m}]$	$EI_m[\text{kNm}^2]$	Increase in stiffness
Steel beam	4.4481	10	1 288 003	
Composite beam	3.9294	10	1 458 025	+13.2 %

The stiffness of the composite beam model compared to the steel reference beam is increased by 13.2%. Both models showed linear elastic behaviour up to a certain stage, followed by a non-linear response due to the yielding of the steel beam.

At the pressure level of 90kN/m^2 and 83kN/m^2 , respectively for the composite beam and steel beam model, yielding of the of the extreme tension fibre of the steel beam was initiated. The yielding pressure q_y is specified as the pressure at which the Mises stresses reach the yield stress of 355MPa . The yielding pressure of 90kN/m^2 can be considered as the load-carrying capacity of the FRP-steel composite system as the steel beam began to fail. At yielding pressure, no connections have failed in the composite beam. The yielding pressure of the steel beam is well approximated by hand calculations:

$$M_y = f_y S = \frac{1}{8} q_y L_{beam}^2 b_{deck}$$

$$\Leftrightarrow q_y = \frac{f_y I_a}{\frac{1}{8} L_{beam}^2 b_{deck} \frac{h_{w,a} + 2t_{f,a}}{2}} = \frac{355 * 6.738 * 10^9}{\frac{1}{8} * 10000^2 * 4400 * \frac{1000 + 2 * 30}{2}} = 82 \frac{kN}{m^2}$$

Eventually at a pressure level of $130kN/m^2$, the analysis of the composite beam model is terminated when the ratio of deformation speed to wave speed exceeds one. At this point, a large part of the steel beam has yielded and the remaining stiffness of the composite system is nearly zero. Approaching the point of $130kN/m^2$, not a single connection has failed. A more elaborate description of the connection damages will be described in the following paragraphs.

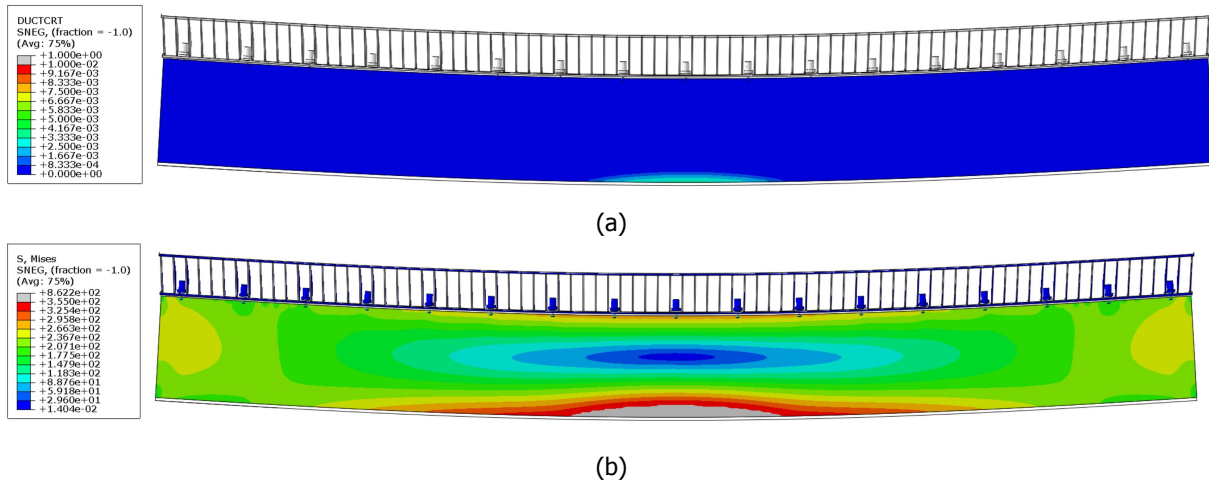


Figure 5.7: Yielding of the steel beam at $90kN/m^2$ visualised with the ductile damage criterion (a) and Mises stresses $< 355MPa$ (b) (Deformations scaled 3x)

In the linear elastic phase, the damages in the SRR and bolt are small. At a pressure level of $10kN/m^2$, the SRR of the bolts which are closest to the support start to show some tensile damage. (Figure 5.8a) As the force increases, the damages grow similarly to the damage figures 4.6 of the detailed connection models.

At a pressure of $50kN/m^2$, the first slipping of the connections closest to the support is initiated. Tensile damage accumulates behind the connector as can be seen in figure 5.8b and the connector starts to bear in the steel beam flanges. This causes stress concentrations and local yielding in the corners between the shank and outer cylinder of the solid bolt which can be seen in figure 5.9a.

Close to the point of ultimate pressure, multiple bolt pairs near the supports have slipped and considerable tensile damage can be observed in the SRR. (Figure 5.8d) The ductile damage, caused by the continuous bearing of the solid bolt in the steel beam top flange, has spread out through the solid bolt shank. Comparing the ductile damages from the detailed connection models (figures 4.6c and 4.7c) to the damage plot 5.9c of the solid bolt, the solid bolt was nearing shear failure. Around the mid-span region, no iSRR connections have slipped and hardly any damage can be observed around these connectors.

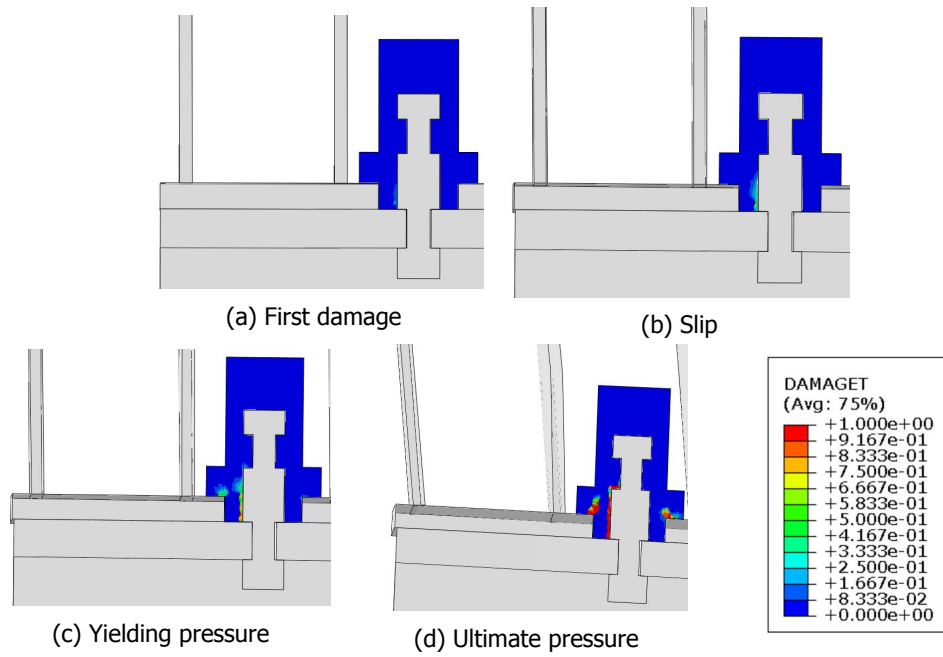


Figure 5.8: Tensile damage (DAMAGET) of the SRR closest to the supports at a pressure of $10 \frac{kN}{m^2}$ (a), $50 \frac{kN}{m^2}$ (b), $90 \frac{kN}{m^2}$ (c) and $130 \frac{kN}{m^2}$ (d)

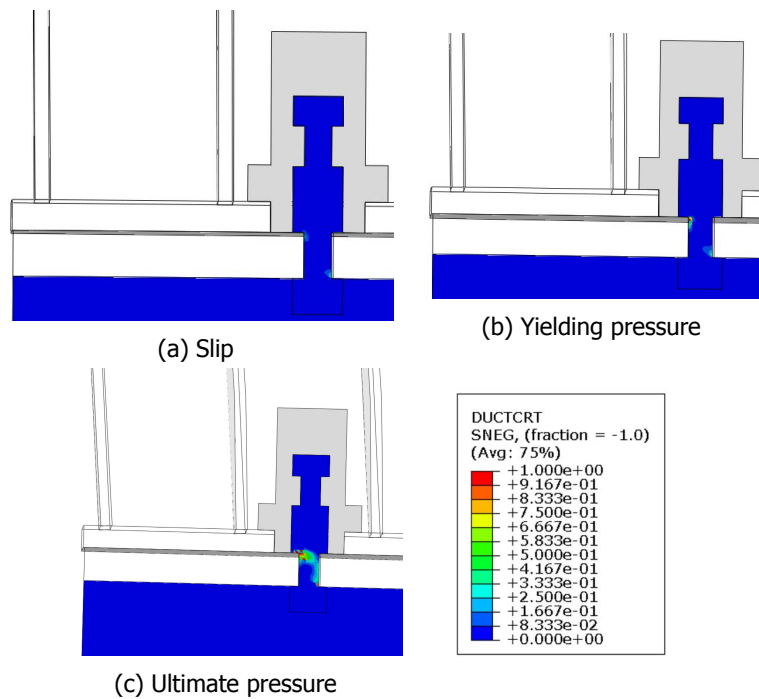


Figure 5.9: Ductile damage (DUCTCRT) of the solid bolt closest to the supports at a pressure of $50 \frac{kN}{m^2}$ (a), $90 \frac{kN}{m^2}$ (b) and $130 \frac{kN}{m^2}$ (c)

5.3.2. Stresses and strains evaluation

The longitudinal stresses and strains along the depth of the composite beam at mid-span are given in figure 5.10. Full composite action was identified between the steel beam and the bottom facing of the FRP. This is evidenced by the continuous strains at the FRP-steel interface. This confirms the effectiveness of the slip-resistant iSRR connections in transferring the shear flow between the FRP deck and the steel beam.

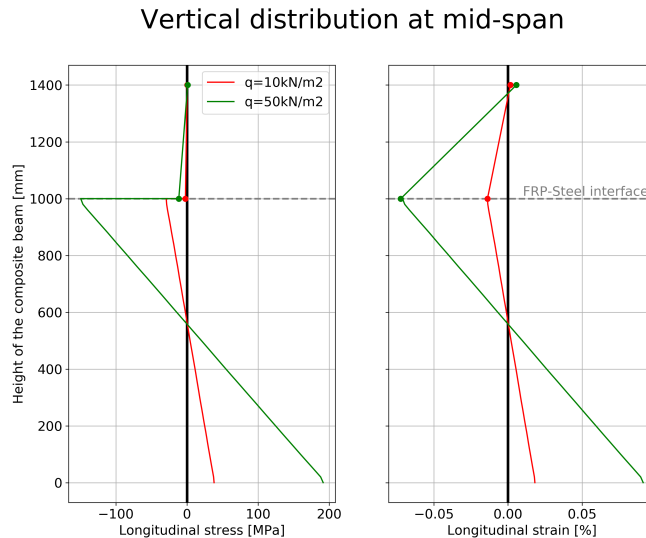


Figure 5.10: Stress-strain distribution along the height of the composite beam at mid-span

However, the composite action offered by the FRP panel itself seems rather low due to the modest longitudinal strains in the top facing. Plotting the stresses along the width of the FRP for the top and bottom facing in figure's 5.11 top graph, reveals a counter-intuitive longitudinal stress distribution in the top facing. Normally, one should expect compressive longitudinal stresses along the entire width of the FRP deck and a compressive longitudinal stress spike like in the bottom facing above the steel beam. Regardless, tensile longitudinal stresses can be found in the top facing at the location of the steel beam. This effect is caused by the transverse bending and secondary moments of the FRP deck due to the uniformly distributed load. The evaluation of this phenomenon and effective width will be discussed in section 5.5.

The transverse bending stresses are clearly visible from the second graph in figure 5.11. Since the panel has symmetry-boundary conditions at the edges, sagging moments are caused at panel's edges while at the panel's centre hogging moments are induced by the uniformly distributed load. This introduces transverse stresses in the top facing which are compressive at the panel's edge and tensile at the centre. The opposite stresses are observed in the bottom facing.

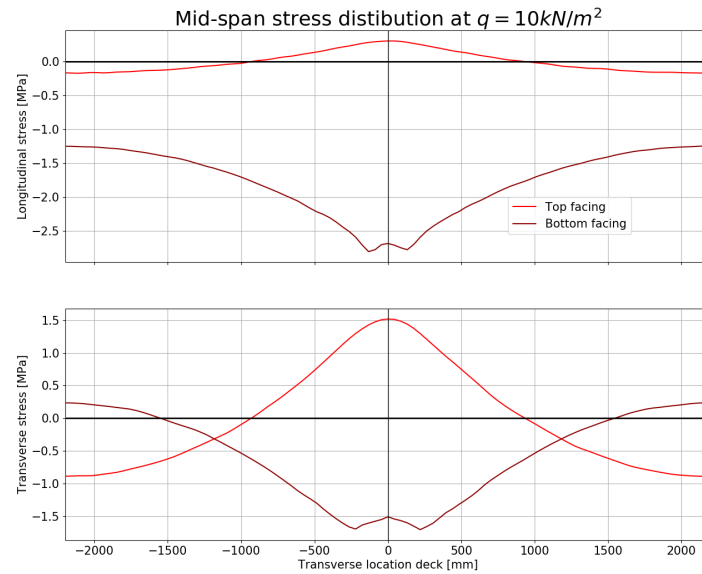


Figure 5.11: Stress distribution along the width of the FRP deck at mid-span

5.3.3. Verification

An analytical approximation of the composite beam bending stiffness was made according to annex B of Eurocode 5. [43] The annex demonstrates a simplified method to calculate the bending stiffness of mechanically fastened timber beams. The bending stiffness of a composite beam with three regions is calculated by the following formula:

$$EI = \sum_{i=1}^3 (E_i I_i + \gamma_i E_i A_i a_i^2)$$

Where the γ_i factors express the level of shear interaction between the regions and the a_i neutral axis distances.

Gürtler [10] demonstrated the use of this method applied on adhesively bonded FRP-steel composite beams under four-point bending tests. The partial composite action provided by the in-plane shear stiffness of the FRP deck, was considered in the design approach. But at the adhesive interface, full composite action was taken into account resulting in a Eurocode 5 formula where only two regions were adopted.

However, when bolted connections are used, partial composite action may be apparent at the FRP-steel interface. That's why Satasivam *et al.* [32] demonstrated that this method can be applied for composite beams with pultruded profiles connected with blind bolts to the steel beam. The three regions of the composite beam are chosen corresponding with figure 5.12.

In appendix C.3, the bending stiffness of the composite beam according to the method described above is presented. Using the bending stiffness, the mid-span displacements at $q = 10kN/m^2$ of the composite beam model are analytically calculated and compared to the FEA results in table 5.4. In order to more accurately approximate the results from the FEA models, the displacements due to shear deformation are incorporated.

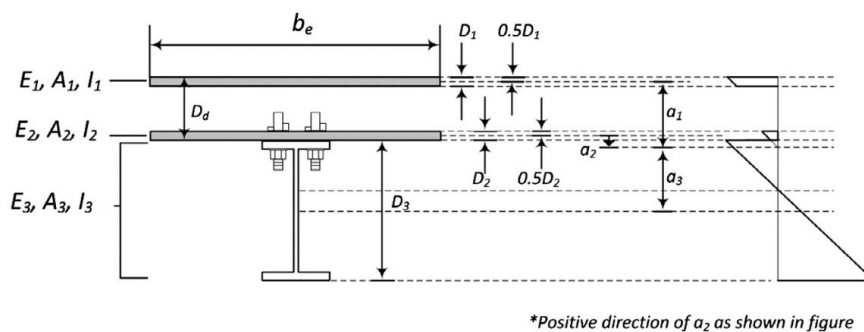


Figure 5.12: Cross-section of the composite beam used in the EC5 method [32]

Table 5.4: Displacements at $q = 10kN/m^2$

	Mid-span displacement [mm]	Difference compared to FEA
Composite beam FEA	3.93	
Composite beam analytically (EC5 method)	3.79	-3.49%
Steel beam FEA	4.45	
Steel beam analytically	4.53	+1.95%

5.4. Comparison of modelling techniques

The aim of this section is to compare the results from the detailed composite beam model to more user friendly and computational inexpensive modelling techniques. Therefore, two more models are built in Abaqus and the engineering software GSA. These models are geometrically identical to the composite beam, but different methods were used to model the FRP-steel interaction. Eventually, the impact of the modelling technique on the FRP-steel connection forces are evaluated.

5.4.1. Abaqus composite beam model simplification

Modelling the discrete solid iSRR connectors in the composite beam model requires a lot of elements and computational power. It was therefore decided to replace the solid connectors by non-linear fastener elements (CONN3D2 elements). The fasteners are assigned with a Cartesian section having non-linear in-plane properties but acting rigid out-of-plane. The non-linear properties of connector section are matched with the results from the embedded nuts connection model from figure 4.4.

Apart from the connection modification, all other modelling parameters stayed the same as elaborated in section 5.1. However, the simplification of the preloaded iSRR connection into a non-linear fastener allows the variation of the friction coefficient between the FRP deck and steel beam. In the previous composite beam model, a coefficient of 0.2 was used as in Du *et al.* [41]. As friction cannot be modelled in engineering software, two analyses with the simplified composite beam model were performed. One model has a coefficient of 0.2 and in the other model the coefficient is set to frictionless. In such a way, the influence of friction on the shear force in the connections is analysed.

5.4.2. GSA composite beam model simplification

The second model is made using the engineering software Oasys GSA. The software is able to provide comprehensible results from large-scale linear models and has a special module for bridge designing and loading. In order to approximate the linear behaviour of the composite beam model presented in section 5.1, some simplifications are implemented:

1. Element types: The 2.5D continuum shell elements are swapped with 2D shell elements. This implicates that trough thickness deformations are not accurate and contacts can't be defined.
2. Connectors: The discrete solid connectors of the composite beam model are replaced by springs

having an in-plane stiffness equal to the upper bound stiffness from the iSRR connector with embedded nuts, i.e. $k_{sc,upper} = 212kN/mm$. The rotational stiffnesses and vertical/axial stiffness of the spring are rigid by appointing a large stiffness of $10000kN/mm$.

3. Material properties: As the modelling of damage is not available in GSA, the steel section is only assigned with an elastic isotropic stiffness of $210GPa$ and a Poisson ratio of 0.3. Elastic orthotropic and isotropic material properties were already assigned to the FRP facings and webs, respectively. Therefore, the material properties of the FRP remain unchanged and according to table 3.3.

The geometries and boundary conditions of the simplified GSA composite beam model are the same as the Abaqus composite beam model. A pair of linear springs is 200 mm separated from each other in transverse direction and 600 mm separated from the next pair in longitudinal direction. An overview of the simplified GSA composite beam model can be seen in figure 5.13.

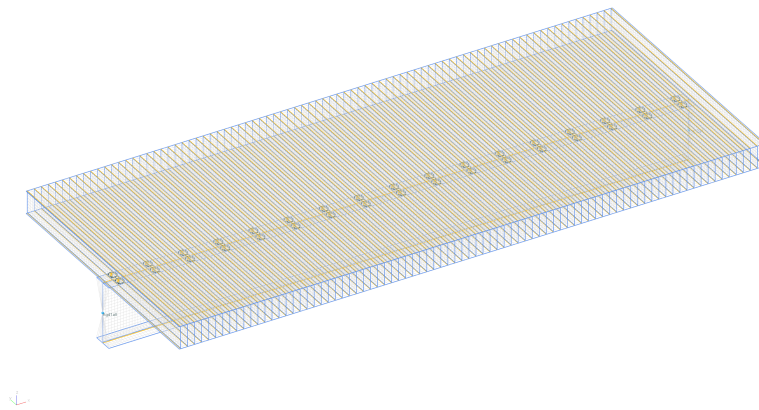


Figure 5.13: Overview of the composite beam model geometry in GSA

5.4.3. Influence of friction on connection forces

In reality, friction exists between the FRP deck and the steel top flange. If the deck is vertically loaded, a part of the shear flow between the FRP deck and steel girder will be transferred by friction while the other part is transferred through the connections. Friction has therefore the positive effect of reducing the connection forces when vertically loaded. In the design process of composite beams, it is generally assumed that the complete shear flow is taken by the interface connections, leading to a conservative connection design. Accordingly, the influence of friction is analysed using the different modelling techniques described in the previous sections.

Up until now, three different modelling techniques of the FRP-steel connections have been described. The connections have been modelled as solid iSRR connectors and non-linear fasteners in Abaqus, and linear springs in GSA. As engineering software is generally incapable of taking friction into account, two intermediary models with non-linear fasteners were made. One takes friction into account while the other excludes friction.

For the models with non-linear fasteners and linear springs, Abaqus and GSA offer the possibility to read the connections forces immediately from the results. As for the solid connection this option is not available, other techniques were used. It was chosen to quantify the connection forces of the solid bolts using the normal force distribution of the steel beam. By extracting section forces of the steel beam before and after the location of a connector pair, the change in section normal force is equal to the force taken by a connector pair.

It was chosen to use a factor to express the influence of friction on the connection forces. In order to exclude any other effect due to modelling techniques, the intermediary models with non-linear fasteners are used to define the factor. These two models have everything in common apart from the friction coefficient between the FRP deck and steel beam. It is also checked if the composite beam model with solid bolts has similar connections forces as the model with non-linear fasteners that includes friction. The same holds for the GSA model with linear springs that should match the results from the model with non-linear fasteners excluding friction.

Figure 5.14 displays the outcomes of the four different analyses at a pressure level of $10\text{kN}/\text{m}^2$. The upper graph plots the longitudinal shear connector force along the beam. As expected, all models show their maximum connector forces near the supports while at mid-span the connector force is zero. With maximum connector forces between 12-15 kN (25% of the slip force), the connector remains in the stiff region before slipping.

Comparing the connection forces from the analyses which included friction, i.e. solid bolts and non-linear fasteners, it can be concluded that they show similar results. The method to determine the connector forces in the solid bolts, demonstrates to work well but at some location small over- or under-estimations are made. This may be explained by the sensitivity of the determination method to local inaccuracies and effects. Nonetheless, it can be concluded that the non-linear fasteners approximate the behaviour of the solid bolts well. Using non-linear fasteners instead of solid bolts, the analysis time was 12 times reduced from 12 hours to just one hour.

When the connection forces from the analyses which excluded friction are compared, good similarities are found as well. The connection forces from the non-linear fasteners and linear springs show the same distribution along the composite beam length. Using the linear springs in GSA also reduced the analysis time dramatically from around one hour to a minute.

Considering that the models with the non-linear fasteners approximate well the connection forces with or without friction, a friction force factor is introduced in the second bar chart of figure 5.14. The friction force factor expresses how much the connection forces are overestimated when friction is excluded from the analysis. Using the connector forces from the non-linear fasteners, it is calculated by dividing the results from the model including friction ($\mu = 0.2$) with the results from the model excluding friction ($\mu = 0$). The maximum friction force factor value of $\alpha_{friction} = 0.89$ can be found near the supports. This means that under for the current configuration, connection forces may be reduced at

least 11% when friction is not taken into account during analyses such as during engineering analysis with linear springs.

For all modelling techniques, similar displacements and therefore stiffnesses are achieved as can be seen in the last graph of figure 5.14. As was determined in section 5.3, the stiffness of the composite beam model compared to the steel reference beam is increased by approximately 13%.

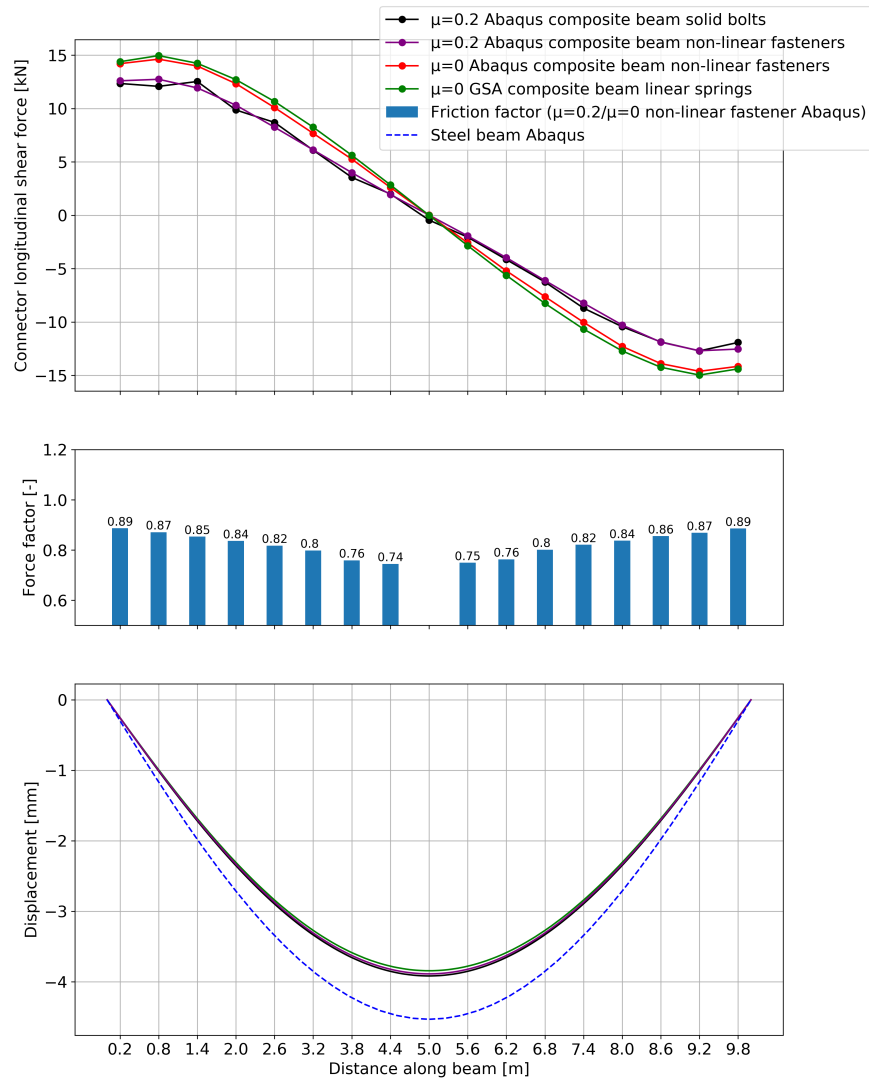


Figure 5.14: Comparison of different modelling techniques at a pressure of 10 kN/m^2

If the pressure is increased to $50kN/m^2$ at which slip was observed in the composite beam model with solid bolts, the same friction force factors are found as can be seen from the second chart in figure 5.15. However, the difference between the two models with friction and the two models without friction have become a bit bigger. This is because around the point of slipping, the stiffness of the connections is decreasing and after slipping it picks up again. It can therefore be the case that some of the outer connections are not slipping yet, slipping or already bearing in the steel flange. In case of the non-linear fastener models excluding friction, the connections have already passed the moment of slipping and picked up forces again. For the models including friction, the connections close to the support are in the stage of slipping or just before. Nevertheless, the friction force factor in this region is conservative when comparing connector forces in the solid bolts with the forces in the linear springs.

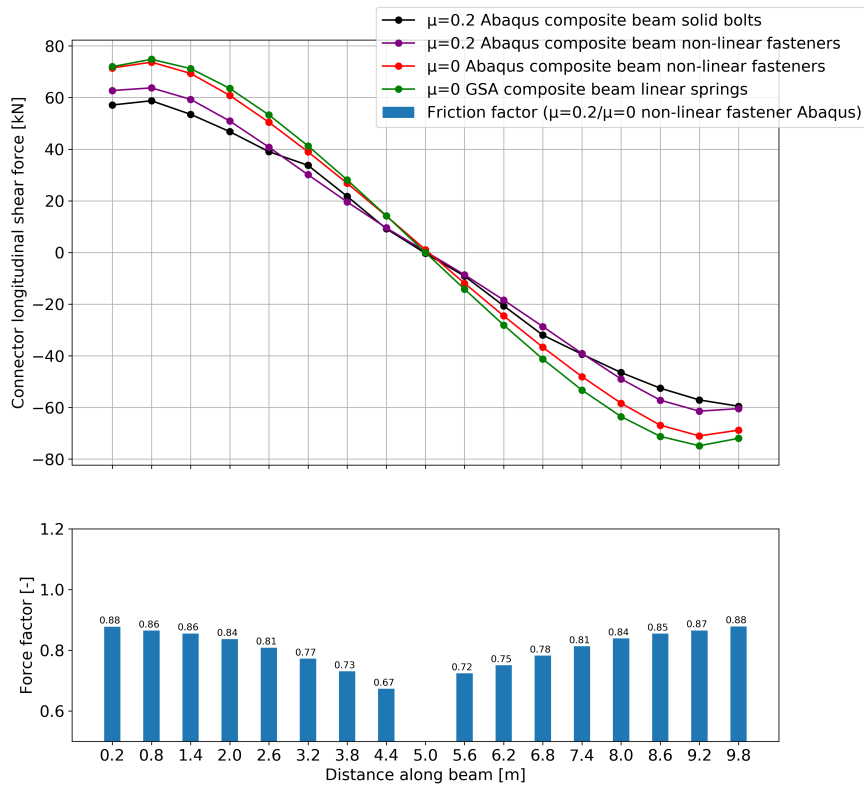


Figure 5.15: Comparison of different modelling techniques at a pressure of $50kN/m^2$

5.5. Discussion of results

5.5.1. Composite action of the FRP panel

Subsection 5.3.2 revealed that the composite action offered by the FRP panel itself was rather low. Figure 5.10 showed that at mid-span, the axial strain distribution is not linear over the composite beam's depth. The top facing of the FRP panel exhibited practically no contribution to the overall bending stiffness of the composite beam which was evidenced by the low strains. The high webs, which are placed in transverse direction, have a great impact on the in-plane stiffness of the panel and causes the incomplete transfer of shear forces between the two facings. This phenomenon has also been reported in literature where partial composite action was observed in FRP panels with rectangular [32] or trapezoidal [10] [23] cell geometries.

Nevertheless, one should not predict tensile longitudinal stresses in the top facing at the location of the steel beam like in figure 5.11. Normally, compressive longitudinal stresses along the entire width of the FRP deck are expected including a stress increase above the steel beam as observed in the bottom facing. The reasons for these tensile longitudinal stresses in the top facing are the transverse bending and secondary moments of the FRP deck due to the uniformly distributed load.

In order to investigate the influence of transverse bending and secondary bending of the deck on the longitudinal stresses in the top and bottom facing, both effects are isolated in two additional models. As the previous section demonstrated that the modelling of the composite beam connections with non-linear fasteners approximates the behaviour of the solid connections well, the composite beam model including non-linear fasteners and friction at the FRP-steel interface is chosen as a reference model for this investigation.

Transverse bending effect

To investigate the effect of transverse bending on the longitudinal stresses in the FRP deck, a condition of the model is assumed where only transverse bending can take place. Longitudinal stresses caused by global bending of the deck are eliminated by fixating the steel beam in vertical direction at the bottom flange. In such a way, only transverse bending can occur over the deck width.

To analytically approximate the transverse and longitudinal stresses in the facings, the panel is subdivided in a range of I-beams having a width equal to the FRP webs spacing (120 mm) and carrying a load $q = 10 \frac{kN}{m^2} * 0.12m = 1.2 \frac{kN}{m}$. This line load creates a hogging moment of $1.94kNm$ at the support of the cross-girder. As the webs have different material properties than the facings, the equivalent web thickness is $t_{web,eq} = \frac{E_{1,web}}{E_{1,facing}} * t_{web} = \frac{18600}{25800} * 10 = 7.21mm$. The transverse stresses and strains in the facings are then calculated:

$$\sigma_T = \frac{Mz}{I} = 1.83MPa$$

$$\epsilon_T = \frac{\sigma_T}{E_{1,FRP}} = \frac{1.83}{25800} = 7.1 * 10^{-5}$$

Where $z = 190mm$ and $I = 201.5 * 10^6 mm^4$ are the lever arm and moment of inertia of the equivalent I-section.

For the top and bottom facing, the equal stresses are positive and negative, respectively. If the top facing is taken as an example, tensile transverse stresses are apparent at the centre of the deck and accordingly transverse elongation. Due to the Poisson effect, the elements want to shrink in longitudinal direction but are restrained by neighbouring elements. This causes tensile strains and stresses in longitudinal direction equal to:

$$\epsilon_L = \sigma_T * \nu_{12,FRP} = 7.1 * 10^{-5} * 0.32 = 2.27 * 10^{-5}$$

$$\sigma_L = \epsilon_L * E_{2,FRP} = 2.27 * 10^{-5} * 15900 = 0.36MPa$$

The results from finite element analysis, which are presented in appendix C.5 and table 5.5, are in line with the analytical approximation strategy described above. At the FRP deck edges, where the sagging moment of $0.97kNm$ occurs, the same analytical calculation approximates the finite element results well. Approaching the supports of the composite beam, the elements are less 'restrained' in longitudinal direction by neighbouring elements. This means that the transverse bending effect has a less prominent influence in these regions as can be seen from figures C.6b and C.7b.

Comparing the longitudinal stresses caused by transverse bending of the deck to the longitudinal stresses from the composite beam presented in figure 5.11 (i.e. $\pm 0.2 MPa$), it can be concluded that the transverse bending effect has a significant influence on the longitudinal stresses in the top facing.

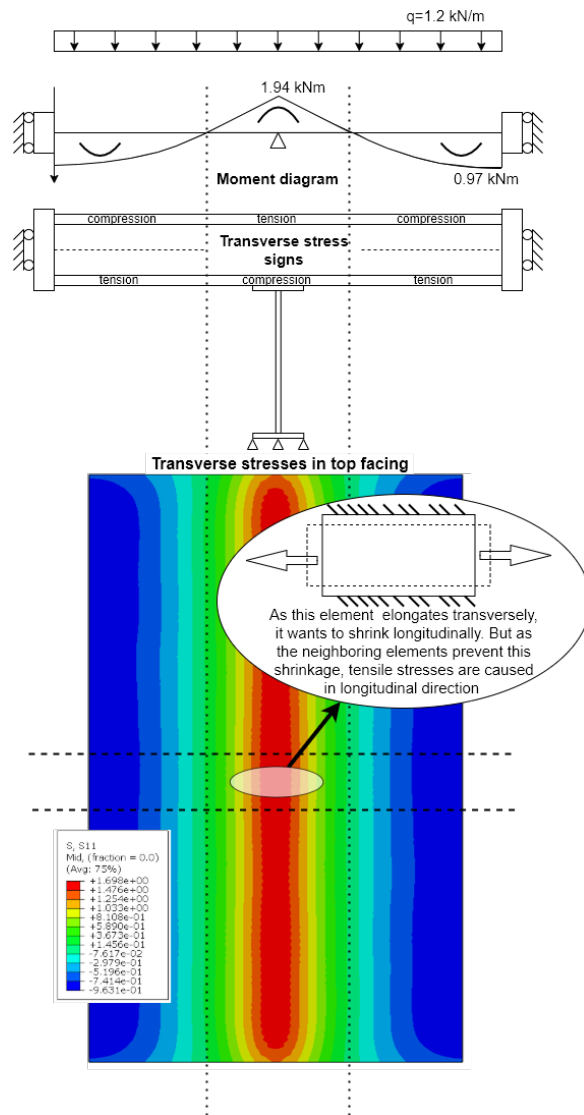


Figure 5.16: Transverse bending and stresses diagram (not-to-scale)

		At deck centre		At deck edge		Note
		σ_L [MPa]	σ_T [MPa]	σ_L [MPa]	σ_T [MPa]	
Analytically	Top facing	0.36	1.83	-0.18	-0.91	Change sign for bottom facing results
FEM	Top facing	0.32	1.7	-0.17	-0.9	
	Bottom facing	-0.33	-1.6	0.16	0.9	

Table 5.5: Analytical versus finite element stresses in the FRP panel

Secondary moment effect

Another effect is causing tensile longitudinal stresses in the top facing of the FRP panel, namely the secondary moment effect. In short, this effect is a second order effect of the load acting on the top facing caused by the incomplete shear transfer between the top and bottom facing in the weak longitudinal direction. As the load causes bending of the composite beam, the bottom facing acts together in compression with the top flange of the steel beam. Because of the low in-plane shear stiffness of the FRP panel, the top facing is not engaged and practically not mobilised. This causes the FRP webs to take a 'fan'-like position which is clearly visible in figure 5.7. As these inclined webs are in compression, the horizontal component results in tensile stresses in the top facing.

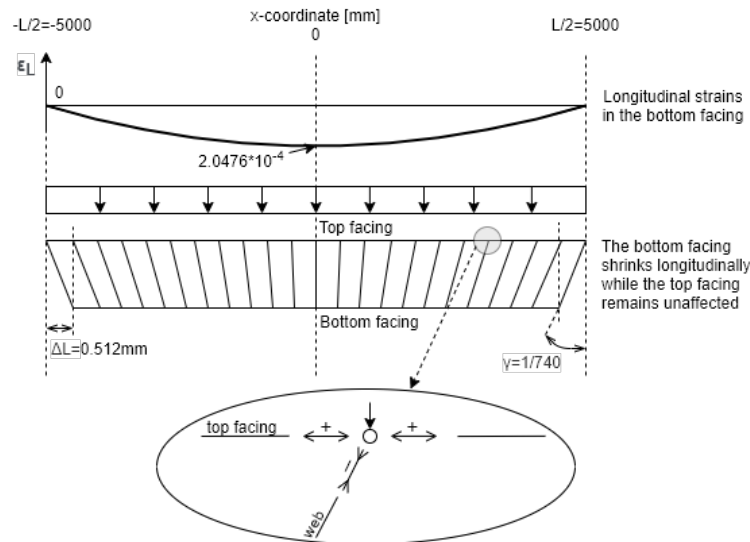


Figure 5.17: Illustration of the secondary moment effect (not-to-scale)

In order to show the impact of this effect, the transverse bending effect needs to be excluded as much as possible. This can be achieved by applying a line load on the top facing of the FRP panel right above the steel beam. The magnitude of the line load is chosen to be equal to the equivalent pressure of 10 kN/m^2 , i.e. $4.4\text{m} * 10\text{kN/m}^2 = 44\text{kN/m}$. The moment that is generated by the line load is equal to $M = \frac{1}{8} * 44 * 10^2 = 550\text{kNm}$. Given this maximum moment at mid-span, the approximate strains at the FRP-steel interface are obtained by:

$$\sigma_{max,a} = \frac{-Mz}{I_a} = \frac{550 * 10^6 * 530}{6.738 * 10^9} = -43\text{MPa}$$

$$\epsilon_{interface} = \frac{\sigma_{max,a}}{E_a} = \frac{43}{210000} = -2.0476 * 10^{-4}$$

As complete interaction was achieved between the FRP bottom facing and the steel beam, it can be assumed that in the FRP bottom facing a strain equal to $\epsilon_{interface}$ is found at mid-span. At the

supports, the longitudinal strains and bending moments are theoretically zero which means that the bottom facing wants to shrink longitudinally following a distribution indicated in figure 5.17. The longitudinal shrinkage of one half of the bottom facing can be linearly approximated as follows:

$$\Delta L = \frac{-2.0476 * 10^{-4} * 5000mm}{2} = -0.512mm$$

As the in-plane shear stiffness of the FRP panel is low, the top facing is practically not engaged. The combination of the immobile top facing and shrinkage of the bottom facing cause the webs to take a 'fan'-like position as can be seen in figure 5.17. The angular rotation of central webs is zero but rotation of the outward webs can be calculated as:

$$\gamma = \frac{\Delta L}{h_{deck}} = \frac{0.512mm}{380mm} \approx \frac{1}{740}$$

Since the inclined webs are in compression and under an average angle of $\frac{\gamma}{2} = \frac{1}{1480}$, the horizontal component of the compression force is introduced as a tensile force in the FRP top facing which is equal to:

$$\sum F_{horizontal} = 44kN/m * 5m * \frac{1}{1480} = 0.150kN = 150N$$

As a line load is applied over the width of the top flange of the steel beam, most of the horizontal stresses are transferred over this width. Having an FRP web thickness of 10 mm and a steel flange width of 350 mm, the tensile longitudinal stress in the top facing at the location of the steel beam can be calculated as follows:

$$\sigma_{L,top-facing} = \frac{150N}{350mm * 10mm} = 0.043MPa$$

The same effect is happening in the bottom facing but as the first order bending is creating a large compression stress, the tensile stresses caused by secondary bending are negligible. The longitudinal stress in the bottom facing would be calculated as: $\sigma_{L,bottom-facing} = \epsilon_{interface} * E_{2,FRP} + \sigma_{L,second-order} = -3.2MPa + 0.043MPa = -3.157MPa$. The tensile and the compressive longitudinal stress in the top and bottom facing, respectively, match the results from finite element analysis presented in appendix C.6 and table 5.6. Using the analytical approximation, the average rotation angle of the webs was used to calculate the stresses but in reality the effect is stronger closer to the supports than at mid-span. In figure C.9, it is clearly visible that the tensile stresses in the top facing are the largest closer to the supports.

		At deck centre σ_L [MPa]
Analytically	Top facing	0.043
	Bottom facing	-3.157
FEM	Top facing	0.05
	Bottom facing	-2.6

Table 5.6: Analytical versus finite element longitudinal stresses in the FRP panel at mid-span

Comparing the magnitude of tensile longitudinal stresses in the top facing caused by the secondary moment effect to the transverse bending effect, it can be noticed that the order of magnitude is 10 times smaller. Figure 5.18 compares the influences of both effects on the longitudinal stresses to the stresses that were found in the original composite beam model of section 5.3. The most important observations from this figure are listed below:

- The secondary moment effect causes a tensile stress component in the top and bottom facing which are from a minor magnitude.
- As longitudinal stresses in the top facing caused by transverse bending (fixed beam) are equal to the reference model, it is confirmed that the counter-intuitive tensile stresses in the top facing are mainly caused due to transverse bending.
- The longitudinal stresses caused by transverse bending are equal but have opposite signs in the top and bottom facing. This means that during the calculation of the effective width, the effect is cancelled out.

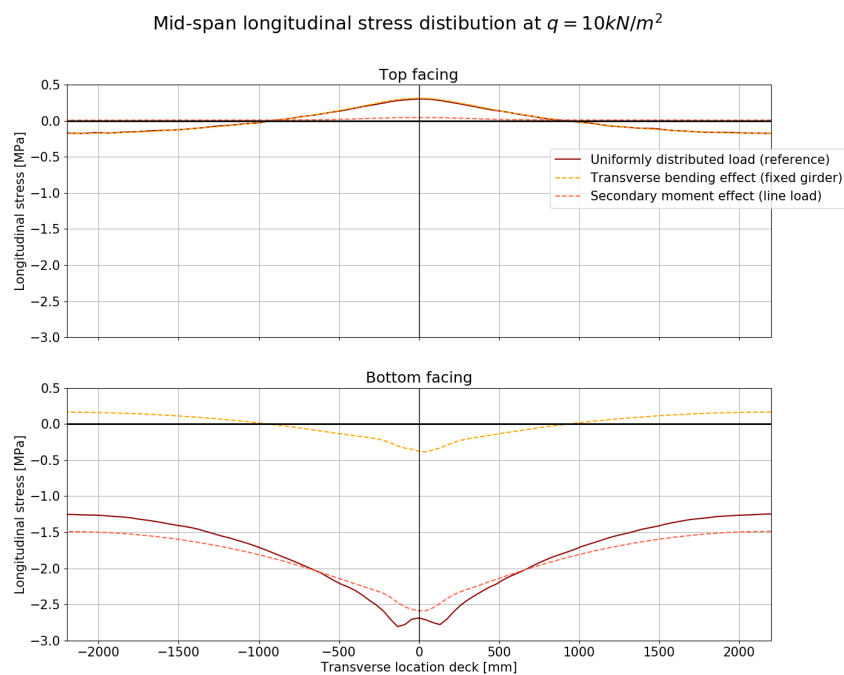


Figure 5.18: Longitudinal stresses at mid-span illustrating the different effects

5.5.2. Effective width

To evaluate the effective width of the FRP deck, the longitudinal stresses at mid-span were extracted from the top and bottom facing of the composite beam model. After discussing of the tensile longitudinal stresses in the top facing from graph 5.11 in the previous subsection, it was shown that the occurring effects have a limited influence on the effective width determination. Figures 5.19a and 5.19b plot the compressive stresses in the top and bottom facing, respectively. Additionally, they demonstrate that the top facing of the FRP deck hardly contributes to the stiffness of the composite system and a large part of the top facings has tensile forces (grey zone) caused by the effects discussed in the previous section. The longitudinal stresses from the top and bottom facing are summed to calculate the effective width of the entire deck.

As can be seen from graph 5.19c, the longitudinal stress distribution across the entire deck is not uniform. This non-uniform distribution is caused by the shear lag effect within the composite beam, resulting in an effective width of the FRP deck contributing to the stiffness of the system. The deck width at which a constant stress is equal to the maximum value σ_{max} of the stress distribution σ_x is known as the effective width b_{eff} . The effective width can also be calculated if the shear lag factor β is known. Evaluating the effective width and the shear lag factor of the FRP deck, gives:

$$b_{eff} = \frac{1}{\sigma_{max}} \int_{b/2}^{-b/2} \sigma_x dy = \frac{1}{2.53} \int_{2200}^{-2200} \sigma_x dy = 3127mm$$

$$b_{eff} = \beta b \Leftrightarrow \beta = \frac{b_{eff}}{b} = \frac{3127}{4400} = 0.71$$

Comparing the effective width of the FRP-steel composite beam to Eurocode 4 [39] calculations for the effective width of interior steel-concrete beams, the effective width and shear lag factor from the FRP-steel system is 16% higher.

$$b_{eff} = b_0 + \sum b_{ei} = b_0 + 2 \frac{L_{beam}}{8} = 200 + 2 \frac{10000}{8} = 2700mm$$

$$b_{eff} = \beta b \Leftrightarrow \beta = \frac{b_{eff}}{b} = \frac{2700}{4400} = 0.61$$

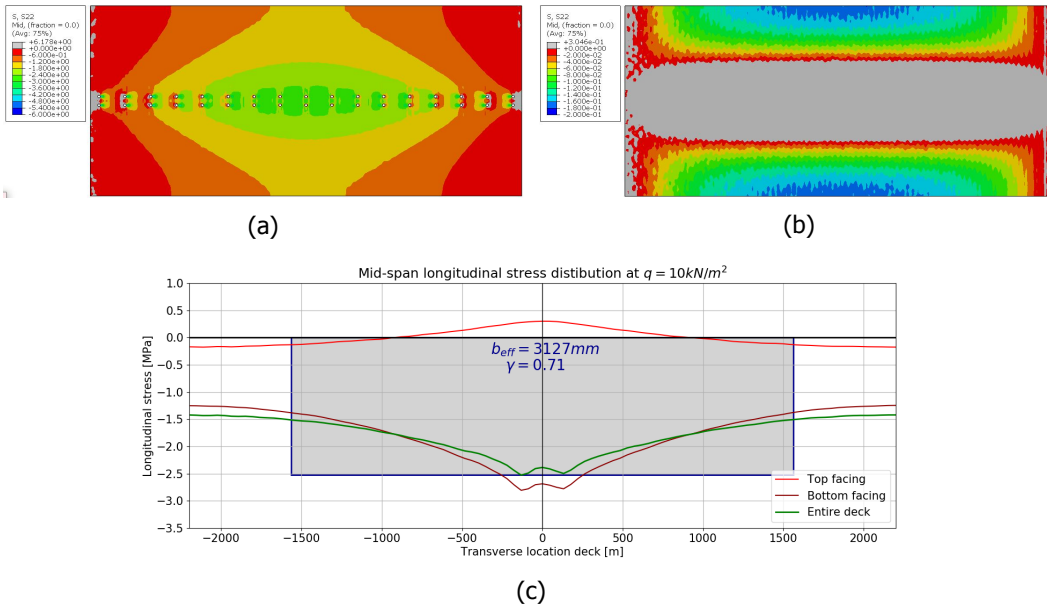


Figure 5.19: Compressive longitudinal stresses in the bottom facing (a), the top facing (b) and plotted (c) at a pressure level of $10 \frac{kN}{m^2}$

5.5.3. Connector spacing

Results presented in section 5.3 revealed that the iSRR connections performed well during the composite beam test. Firstly, slipping was observed at a uniformly distributed load of 50kN/m^2 which is around five times higher than the bridge traffic load levels regarded in the Eurocodes. Secondly, when yielding and thus ductile failure of the composite beam is initiated at 90kN/m^2 , none of the connections have failed in their governing bolt shear failure. Therefore, it can be suggested that the original connector spacing of 600 mm might be conservative.

Additional analyses are performed with a connector spacing of 1200 mm using both the solid bolts and the non-linear fasteners in Abaqus. This means that the amount of connectors over the length of the composite beam is reduced from 34 to 18 connections. Since less connectors are positioned over the length of the composite beam, higher forces need to be endured to transfer the shear flow between the FRP deck and steel beam. Areas of interest that will be compared with the results presented in section 5.3 are: the load at which slipping takes place, the bolt force distribution and the accumulated connector damage around yielding pressure.

Graph 5.20 plots the increasing pressure on the top-facing of the FRP deck against the mid-span displacement. The graph includes the results of the composite beam model with a connector spacing $c_w = 600\text{mm}$ and $c_w = 1200\text{mm}$, and the results of only the steel beam. Comparing the behaviour of the composite beam model with the two different spacings, hardly any difference can be observed in the linear-elastic phase. The composite beam model with a spacing of 1200 mm also has a stiffness which is about 13% higher than the steel beam only.

The linear-elastic behaviour ends when the steel beam starts to yield at a pressure of 90kN/m^2 . Comparing figures 5.7 and C.11, the onset of the non-linear behaviour is the same as the composite beam with a spacing of 600 mm. This is because, even with a spacing of 1200 mm, no connectors have failed at yielding pressure. The FRP deck remains therefore engaged with the steel beam until yielding is initiated.

Eventually, at a pressure level of 115kN/m^2 , the analysis of the composite beam is terminated when the ratio of deformation speed to wave speed exceeds one. At this pressure, a large part of the composite beam has yielded. Although no connections failed, large damages in the SRR (figure 5.22c) suggest that the connections near the supports were on the verge of failing and probably caused the analysis to terminate.

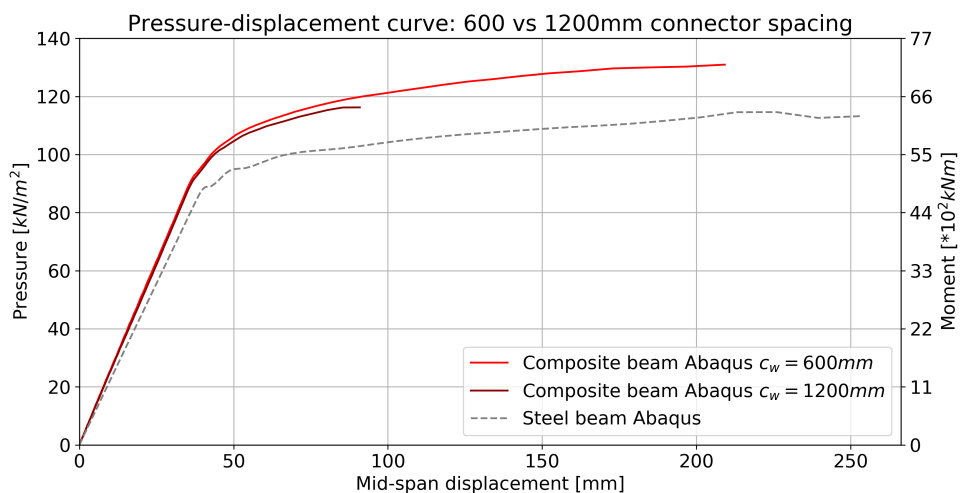


Figure 5.20: Pressure-displacement graphs comparing the 600 vs 1200 mm connector spacing

As the connector amount is almost halved when using a spacing of 1200 mm, larger shear forces are taken by the connections. This implies that forces and damages accumulate faster for the same

pressure level compared to the composite beam with a spacing of 600 mm. Figure 5.21, shows this implication by plotting the connector forces at a pressure of 10 kN/m^2 . The graph also includes the analysis of the same composite beam model with non-linear fasteners as presented in section 5.4. Comparing the connector forces of the $c_w = 600\text{ mm}$ and $c_w = 1200\text{ mm}$ non-linear fastener models, it can be seen that the force having a connector spacing of $c_w = 1200\text{ mm}$ is maximally 1.78 times higher.

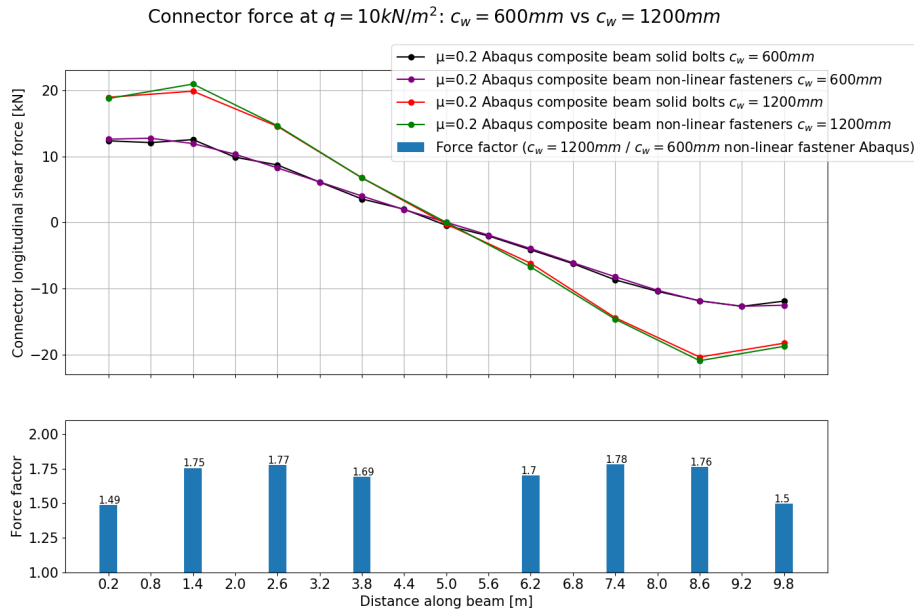


Figure 5.21: Longitudinal connector forces at 10 kN/m^2 for a spacing of 600 mm and 1200 mm

The increase of connector spacing also results in a decrease in pressure at which the first slipping takes place. Having a connector spacing of 600 mm, slipping was observed at a pressure level of 50 kN/m^2 . When the connector spacing is increased to 1200 mm, the first slipping of the connectors near the supports is marked at a pressure of 35 kN/m^2 . At this point, the tensile damage in the iSRR and ductile damage in the solid bolt (figures 5.22a and 5.23a are similar to the damages observed in the model with a spacing of 600 mm (figures 5.8b and 5.9a).

At the yielding pressure of 90 kN/m^2 it can be observed that the connectors having a spacing of 1200 mm have accumulated more damages than the connectors having a spacing of 600 mm. This can be seen when comparing damage figures 5.22b and 5.23b from the model with a spacing of 1200 mm to the damage figures 5.8c and 5.9b from the model with a spacing of 600 mm.

The reason why the model with a connector spacing of 1200 mm terminates earlier than the model with a spacing of 600 mm, i.e. 115 kN/m^2 and 130 kN/m^2 respectively, is that the damages accumulate faster. Figure 5.22c shows how tensile damage in the SRR accumulate around the solid bolt. Comparing it to the tensile damage figure 5.8d from the model with a spacing of 600 mm, more damage is found in the SRR with a spacing of 1200 mm.

To conclude, doubling the connector spacing from 600 mm to 1200 mm still leads to the ductile failure of the composite system. Although this connection spacing is outside of the recommended maximum of 800 mm for headed studs in steel-concrete structures [39], it still leads to a favourable failure mode. The maximum limit is not only prescribed for strength reasons but also takes into account serviceability considerations. Larger spacings could lead to moisture entrapment between the headed studs at the interface which eventually leads to the deterioration of the steel, concrete or FRP. As in the proposed FRP-steel design an epoxy adhesive is applied at the FRP-steel interface, moisture is not able to enter the interface.

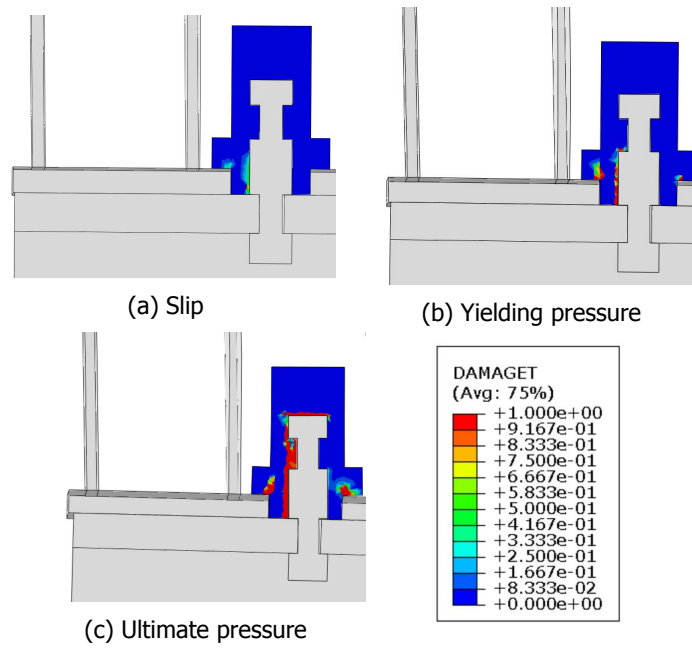


Figure 5.22: Tensile damage (DAMAGET) of the SRR closest to the supports at a pressure of $35 \frac{kN}{m^2}$ (a), $90 \frac{kN}{m^2}$ (b) and $115 \frac{kN}{m^2}$ (c)

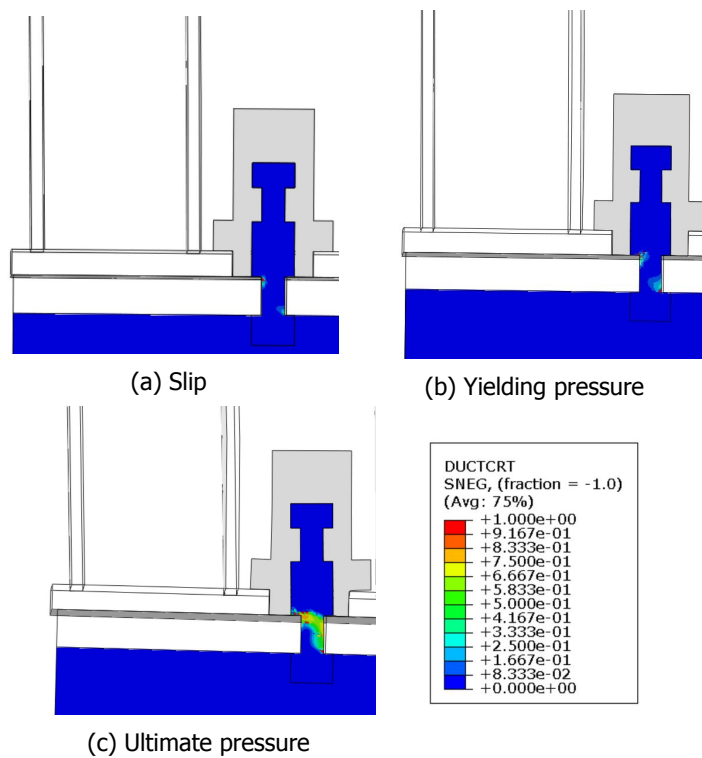


Figure 5.23: Ductile damage (DUCTCRT) of the solid bolt closest to the supports at a pressure of $35 \frac{kN}{m^2}$ (a) $90 \frac{kN}{m^2}$ (b) and $115 \frac{kN}{m^2}$ (c)

5.6. Summary

This chapter investigated the mechanical performance of FRP-steel composite beams through finite element modelling. In order to study the composite behaviour of the hybrid FRP-steel deck system (objective 2) and appropriate modelling techniques (objective 3), a composite beam model was made. A summary of the performed analyses in this chapter, is given in the list below:

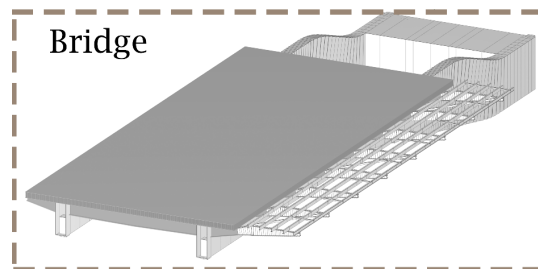
- A composite beam, composed of an FRP deck strip attached to an underlying cross-girder, was modelled. The system length of 10m was chosen equal to the distance between the main-girders of the Beneden Merwede bridge and the 4.4m width of the FRP deck was matched to the centre-to-centre distance of the cross-girders. As the geometry was symmetrical and a symmetrical uniformly distributed load was applied on the deck's surface, symmetry boundary conditions were employed.
- In order to apply discrete solid iSRR connections every 600 mm on the large-scale composite beam model, a simplification of the connection model was made using solid bolts. In order to achieve the same slip behaviour, the slip coefficient between the solid bolt and steel beam flange had to be reduced from 0.35 to 0.2. A slip factor $\alpha_{slip} = \frac{0.2}{0.35} = 0.6$ was introduced to account for change in slip force due to the change of friction planes.
- The results from the composite beam analysis demonstrated a linear phase and non-linear phase on the pressure-displacement curves. During the linear phase, the stiffness of the composite beam was 13.2% higher compared to the stiffness of only the steel beam. The first minor tensile damages were observed at a pressure level of 10kN/m^2 , followed by the first slipping of the connections near the supports at 50kN/m^2 . The initiation of non-linear phase and failure, was triggered by the yielding of the extreme tensile fibre of the steel beam at 90kN/m^2 . Eventually, the analysis was terminated at a pressure level of 130kN/m^2 when a large part of the steel beam had yielded. At this ultimate pressure, no connections had failed but substantial damages were visible at the outer connections.
- Full composite action was identified between the steel beam and the bottom facing of the FRP. This was evidenced by the continuous strains at the FRP-steel interface. This confirms the effectiveness of the slip-resistant iSRR connections in transferring the shear flow between the FRP deck and the steel beam. However, the composite action offered by the webs of the FRP panel itself was low. At mid-span, the axial strain distribution was not linear over the composite beam's depth. The top facing of the FRP panel had practically no contribution to the overall bending stiffness of the composite beam.
- The FRP top facing exhibited longitudinal tensile stresses at the location of the steel beam. Normally, compressive longitudinal stresses along the entire width of the FRP deck are expected. These tensile longitudinal stresses in the top facing were mainly caused by the transverse bending of the FRP deck due to the uniformly distributed load. The effect causes equal but opposite longitudinal stresses in the top and bottom facings. This means that during the calculation of the effective width, the effect is cancelled out.
- An effective width of 3127 mm was achieved resulting in a shear lag factor of 0.71. Comparing the effective width of the FRP-steel composite beam to hand calculations for the effective width of concrete-steel beams, the effective width of the FRP-steel composite beam was 16% higher.
- The analytical approximation of the bending stiffness using the Eurocode 5 method, showed relatively accurate results. Calculated displacements at mid-span under a pressure load of 10kN/m^2 were 3.5% lower compared to the FEA results.
- In order to simulate the behaviour of the iSRR connections in engineering software, further simplifications of the FRP-steel connections were made and compared. The solid iSRR connectors were replaced by non-linear fasteners in Abaqus, and linear springs in GSA. As engineering software is generally incapable of taking friction into account, two intermediary analyses with non-linear fasteners were made. One took friction into account while the other excluded friction.

- Comparing the connection forces from the analyses which included friction, i.e. solid bolts and non-linear fasteners in Abaqus, it was demonstrated that the non-linear fasteners approximated the behaviour of the solid bolts well and reduced the computation time 12 times. The same conclusion was made when the connection forces from the analyses which excluded friction were compared. The connection forces from the non-linear fasteners and linear springs showed the same distribution along the composite beam length. Using the linear springs in GSA also reduced the analysis time dramatically from around one hour to a minute.
- To express the influence of friction on the connector forces, a friction force factor $\alpha_{friction}$ was introduced. The friction force factor expresses how much the connection forces are overestimated when friction is excluded from the analysis. Using the connector forces from the non-linear fasteners, it was calculated by dividing the results from the model including friction ($\mu = 0.2$) with the results from the model excluding friction ($\mu = 0$). A maximum friction force factor of $\alpha_{friction} = 0.89$ was found near the supports for multiple pressure levels. This means that connection forces may be reduced at least 11% when friction is not taken into account during the analysis, i.e. during engineering analysis with linear springs.

6

Bridge level

This chapter aims to provide an answer to the last objective 4. Using the modelling techniques developed in the previous chapter, a global bridge model is made. The bridge model is used to analyse the FRP-steel connection forces that are generated by critical load cases. Based on different bolt placement configurations, a recommendation is made for the connection positioning.



Like in the previous chapters, the reader is firstly introduced to the model which is used to analyse the deck-to-girder connections. Secondly, section 6.2 evaluates the forces in the deck-to-girder connections resulting from the critical load cases. Finally, section 6.4 presents a comparison between the original design with the timber deck and the renovation design with the FRP deck.

6.1. Modelling technique

The starting point for the global model is an Oasys GSA model which was generated by Arup for the reassessment of the Beneden Merwede bridge. The elements of the timber deck and the secondary girders were removed to obtain the structure which can be seen in figure 6.1. In this chapter, the longitudinal direction is referred to as the traffic direction. The transverse direction is denoted as the direction orthogonal to the traffic direction.

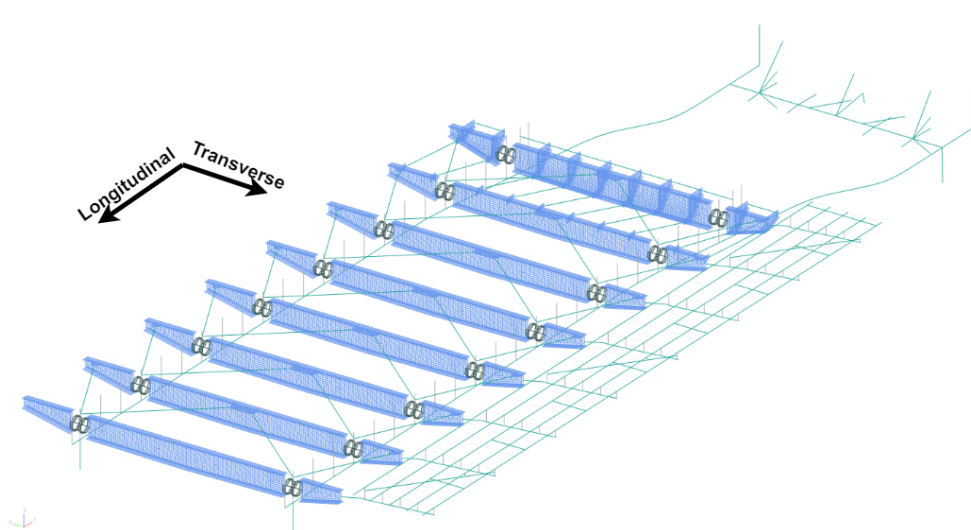


Figure 6.1: Overview of the GSA bridge model provided by Arup

The linear model consists of mostly beam elements apart from the cross-girders which are modelled in 2D shell elements. As the model presented in figure 6.1 contains only steel elements, only elastic isotropic steel material properties are assigned. The cross- to main-girder connections are modelled using linear multi-axial springs. All stiffnesses, apart from the weak axis bending stiffness, are set to infinitely large ($10 * 10^6 \text{ kN/m}$ or kNm/rad). The weak axis bending stiffness of the cross- to main-girder connections is determined by a detailed shell model where each rivet is modelled separately as can be seen in figure 6.2. Applying a force of 25 kN at a distance of 1.125 m induced a displacement of 1.052 mm. This results in a weak axis bending stiffness of 41.000 kNm/rad .

Connection properties	Unit	Stiffness
Translational stiffnesses	kN/m	$10 * 10^6$
Strong axis bending & torsion	kNm/rad	$10 * 10^6$
Weak axis bending	kNm/rad	41.000

Table 6.1: Cross- to main-girder connection properties

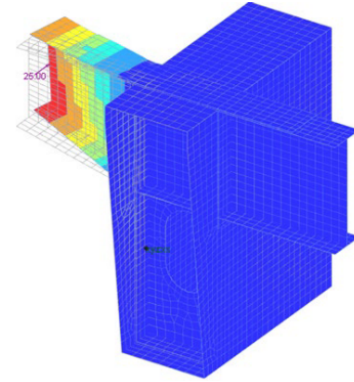


Figure 6.2: Local model to weak axis bending stiffness [36]

The global bridge model is upgraded with an FRP deck which consists of 2D shell elements and corresponds to the geometry presented in table 3.2. The FRP facings and webs are assigned with respectively orthotropic and isotropic material properties according to table 3.3. Figure 6.3 presents the cross-section of the Beneden Merwede bridge with the FRP deck. The modelling strategy of the FRP-steel connections presented in subsection 5.4.1, is applied to connect the steel girders to the FRP deck.

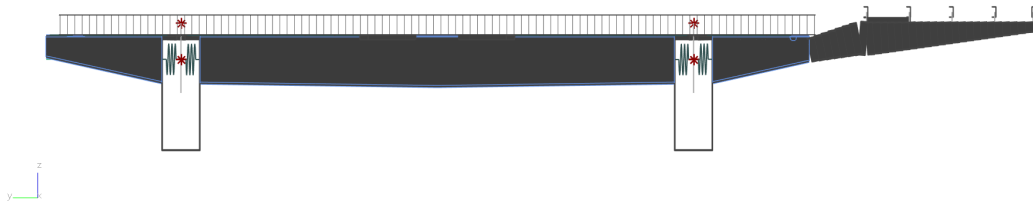


Figure 6.3: Section of global bridge model including the FRP deck

For the first iteration of the deck-to-girder connection distribution, it is assumed that all iSRR connections are placed on the cross-girders. When the timber deck and secondary girders are removed, the top flange of the cross-girders are easily reachable for the installation of the iSRR connectors. This is not the case when installing the iSRR connections inside the box sections of the main-girders. Every 600 mm, a pair of iSRR connections (modelled as linear springs) is connecting the top flange of the cross-girders with the bottom facing of the FRP deck. Using this distribution, a total of 400 connections are used as can be seen in figure 6.4.

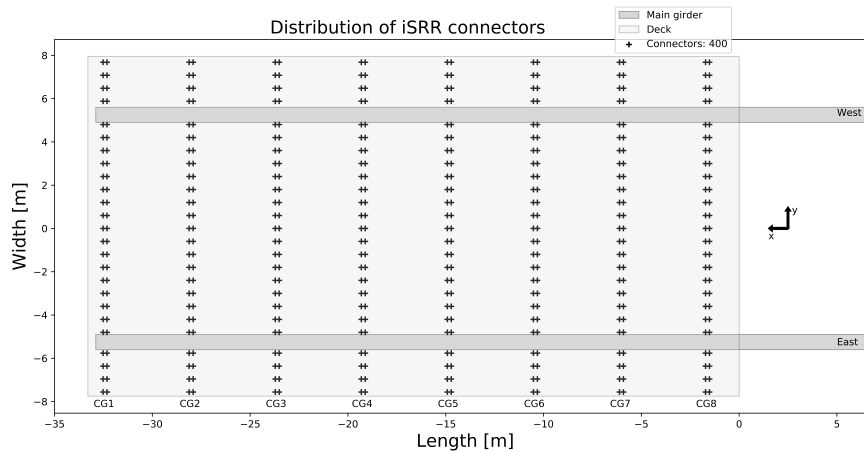


Figure 6.4: Distribution of the iSRR connectors

6.1.1. Permanent loads

The permanent loads imposed on the structure consist of the self-weight of the steel superstructure, the counterweights and the FRP deck. The density of the steel superstructure is set to $7850\text{kg}/\text{m}^3$. The visualisation of the weight of the steel superstructure can be found in figure D.1. Considering a fibre volume of 50%, the density of the laminates is calculated as $1855\text{kg}/\text{m}^3$. The weight of the counterweight is imposed by nodal loads as can be seen in figure D.2. In order to take into account the weight of connections, stiffening plates, etc., the gravitational constant $g = 9.81\text{m}/\text{s}^2$ is factored by 1.1 (10%).

The self-weight of the new FRP deck is approximately $1.137\text{kN}/\text{m}^2$ as calculated in the appendix D.3. Comparing that to the weight of the original timber deck and secondary girders, which was calculated at $1.97\text{kN}/\text{m}^2$ in appendix D.4, the timber deck and secondary girders were 73% heavier than the FRP deck.

6.1.2. Variable loads

To analyse the force-states in the deck connectors, a selection of important bridge deck loads is considered from the Eurocode. Critical variable load types for the analyses of the connectors are: traffic and thermal loads.

Traffic load model 1

Traffic load model 1 is considered since Eurocode EN1991-1-2 [44] prescribes the usage of this load model for both global and local verifications. The load model intends to simulate the effect of having a bridge deck full of traffic, i.e. traffic congestion. Load model 1 contains a set of concentrated force tandems and uniformly distributed loads spread over the corresponding notional lanes. The bridge deck can be divided in four notional lanes. The first notional lane is taken as the East lane because it is the side of the pedestrian path. The uniformly distributed load on the first notional lane is $9\text{kN}/\text{m}^2$ and an axle loads of the tandem system are set to 300 kN. The second, third and fourth notional lanes are loaded with a uniform pressure of $2.5\text{kN}/\text{m}^2$. However, only the second and third lane are loaded with axle loads of respectively 200 kN and 100 kN as can be seen in figure 6.5.

For the longitudinal positioning of the tandem systems, it is chosen to consider five positions. At these five positions, the tandem systems on the first three notional lanes are aligned across the width of the deck. The tandem systems at position one are situated in the middle between the central cross-girders. At positions two and three, the tandem systems are positioned directly above the central cross-girders. The tandems at positions four and five are located at the first and last cross-girder.

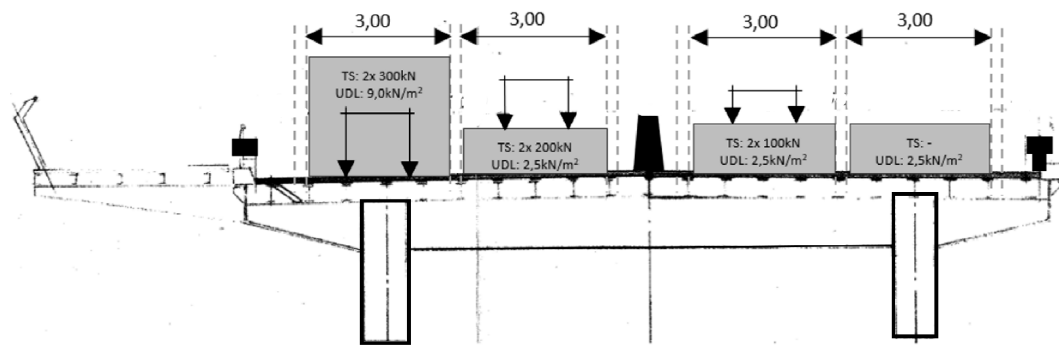


Figure 6.5: Traffic load model 1 imposed on the Beneden Merwede bridge

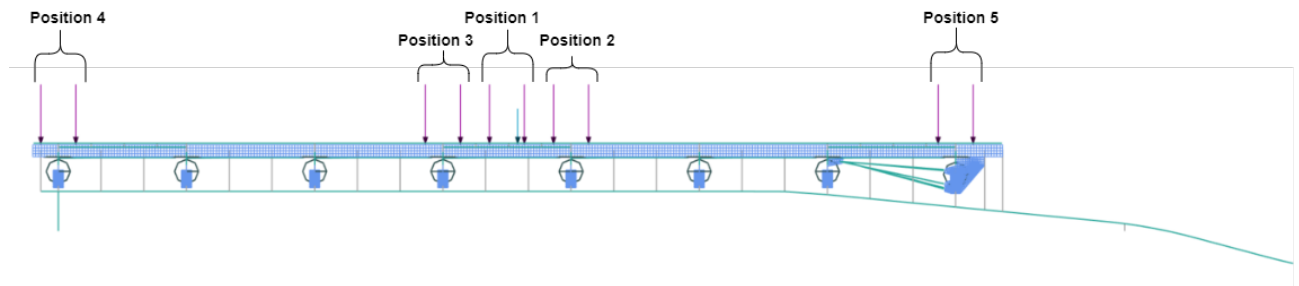


Figure 6.6: Longitudinal positioning of the tandem systems

Fatigue load model 4b

Although a fatigue assessment is outside the scope of this thesis, fatigue load model 4b (FLM4b) is used to determine maximum forces in the deck-to-girder connections for a realistic load case. [45] The load model is composed of a set of seven lorries with different axle loads and geometries that are used to simulate the typical heavy traffic on European highway. The lorries are defined by the axle spacing and their number, the equivalent load and the wheel contact area. In the case of the bridge analysis, the heaviest lorry with 7 axles will be used and positioned on notional lane 1 at mid-span as visualised in figure 6.7.

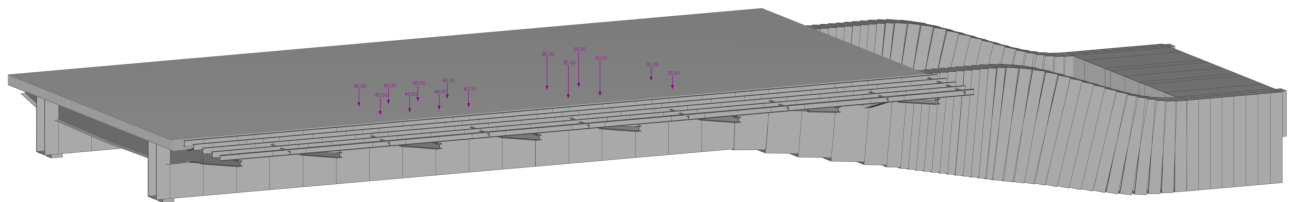









Figure 6.7: Application of heaviest FLM4b truck with seven axles

Tabel NB.8 — Verzameling van gelijkwaardige vrachtwagens voor belastingsmodel 4b

Type voertuig			Verkeerstype			Wiel- type
Afbeelding van de vrachtwagen	Afstand tussen de assen m	Gelijkwaardige aslast kN	Lange afstand (%) ^a	Middellange afstand (%) ^a	Lokaal verkeer (%) ^a	
	4,5	70 130	20,0	50,0	80,0	A B
	1,50 2,40 1,30	70 120 120 120	7,0	4,0	4,0	A C B B
	3,20 5,20 1,30 1,30	70 130 100 100 90	37,0	20,0	5,0	A B C C C
	3,40 6,00 1,80	70 140 90 90	20,0	12,0	4,0	A B C C
	4,80 3,60 4,40 1,30	70 150 80 80 70	10,0	10,0	5,0	A B C C C
	3,20 1,30 4,40 1,80 1,80	80 160 100 100 100 100	4,5	3,0	1,5	A B C C C C
	3,20 1,40 4,40 1,30 1,30 1,30	70 180 170 80 80 80 90	1,5	1,0	0,5	A B B C C C C

^a Percentage vrachtwagens.

Figure 6.8: Definition of fatigue load model 4b [45]

Thermal loads

Thermal loads are considered according to Eurocode EN1991-1-5. [46] Bridge decks described in the Eurocode are grouped in steel, concrete-steel and concrete bridges but unfortunately no FRP-steel bridges. Since FRP decks have a similar thermal conductivity as concrete decks, thermal loads are considered for concrete-steel bridges. From this group, the temperature difference component is taken into account as the governing case. Using this thermal load case, only the FRP deck is heated over its height h to a temperature of 15°C as seen in figure 6.9. Normally both expansion and contraction should be considered but for this case expansion is only assumed.

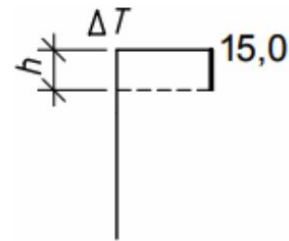


Figure 6.9: Temperature difference component for the thermal expansion load case [46]

6.2. Analysis of the deck-to-girder connections

This section presents the deck-to-girder connection forces that are generated by the critical load cases presented above. Since the objective of this analysis is to verify the connection forces, permanent loading is not taken into account. This is because during the unpropped installation of the deck, the fixture of the FRP deck to the steel superstructure is done after the deck is already resting on steel superstructure. A distinction is made between serviceability limit state (SLS) and ultimate limit state (ULS).

Serviceability limit state

In serviceability limit state, the situation is considered that the bridge is under frequent loading. The heaviest truck from fatigue load model 4 is combined with the thermal heating of the FRP deck. For this combination, the initial stiffness $k_{sc,upper} = 212kN/mm$ is applied to check whether the forces in the connections are not exceeding the design slip force $F_{s,Rd} = 55kN$ obtained from appendix B.2. The characteristic load combination is used because the limit state is irreversible. The combination for SLS verifications is then given by:

$$\sum G_{kj} + Q_{k1} + \sum(\psi_{0i} * Q_{ki})$$

For which $G_{kj} = 0$ are the permanent loads, Q_{k1} is the leading variable load and $\psi_{0i}Q_{ki}$ are the accompanying variable loads. The combination factor ψ_{0i} is taken as $\psi_{0,gr1a,TS} = 0.75$ for traffic FLM4b truck and $\psi_{0,Tk} = 0.6$ for thermal actions. The combination factors ψ are taken as recommended values from Eurocode EN-1990 table A2.1. [47]

Ultimate limit state

At ultimate limit state levels, the resistance of the connectors is compared to the occurring forces. At this level, the deck-to-girder connections are assigned with the lower bound stiffness $k_{sc,lower} = 67kN/mm$. The shear force levels in the connections should not exceed the design strength $F_{v,Rd} = 118kN$ as obtained from appendix B.2. In this situation, it is assumed that the bridge is full of traffic and high temperatures heat up the deck. Therefore, traffic load model 1 and thermal loading is applied to the FRP deck. The fundamental combination from EN1990 Eq 6.10 is used to assemble the load combinations for ULS verification of the deck-to-girder connections.

$$\sum \gamma_{Gj} * G_{kj} + \gamma_{Q,1} * Q_{k1} + \sum(\gamma_{Q,i} * \psi_{0i} * Q_{ki})$$

In this equation, permanent loading is not taken into account. The partial safety factors are taken from Eurocode EN-1990 table A2.4. [47] The recommended safety factors are taken as $\gamma_{Q,traffic} = 1.35$ for traffic loads and $\gamma_{Q,T} = 1.5$ for thermal loading. The combination factors for the traffic LM1 loading are $\psi_{0,gr1a,TS} = 0.75$ for the tandem systems and $\psi_{0,gr1a,UDL} = 0.4$ for the uniformly distributed load. For the thermal loading, the combination factor is set to $\psi_{0,Tk} = 0.6$ for thermal actions.

Table 6.2: Combinations

Leading load case		$Q_{traffic}$	$Q_{Thermal}$
SLS	Traffic	1	0.6
	Thermal	0.75	1
ULS	Traffic	1.35	1.5*0.6=0.9
	Thermal	1.35*0.75=1.01 (TS)	1.5
		1.35*0.4=0.54 (UDL)	

6.2.1. Serviceability limit state

In serviceability state, the slipping of the deck-to-girder connections is not permitted. All deck-to-girder connections are modelled with linear springs having a stiffness of $k_{sc,upper} = 212\text{kN/mm}$. Firstly, the results from the unfactored FLM4b truck and thermal load cases are presented. Lastly, the load cases are combined and compared to the design slip resistance. In appendix D.2, all the results corresponding to the SLS load cases are presented.

Fatigue load model 4b

Figure 6.12 presents the forces in the deck-to-girder connections when the bridge is only subjected to the heaviest FLM4b truck. Because the cycling path is situated on the eastern side of the bridge, the load is slightly unsymmetrical and balanced towards the East. This reflects in higher absolute values of the connection forces on the eastern side of the bridge. Although the connection forces stay below the slip limit of $F_{s,Rd} = 55\text{kN}$, the maximum force in the connections was measured at 51.94 kN in longitudinal direction F_x . This is already high considering only traffic loading.

Investigating the longitudinal forces F_x depicted in figure 6.12a, it appears that the maximal longitudinal forces are mainly concentrated at the cross- to main-girder connections. Further away from the main-girders, the longitudinal forces drop to approximately zero. The reason why the connection forces are higher near the main-girders is similar to the connection force distribution that was found during the composite beam test. The cross-girders are connected to the main-girders every 4.4 m. Because at these locations the FRP deck is connected to the cross-girders and the cross- to main-girder connections are infinitely stiff in most directions, the FRP deck acts compositely with the main-girder. Having a large connector spacing in longitudinal direction of 4.4 m results in high longitudinal connector forces. To demonstrate this effect, the normal force and its change over the length of the eastern main-girder are plotted in figure 6.10. As expected, at the location where the change in normal force is the highest (cross-girder 6), the longitudinal forces in the deck-to-girder connection are the highest as well.

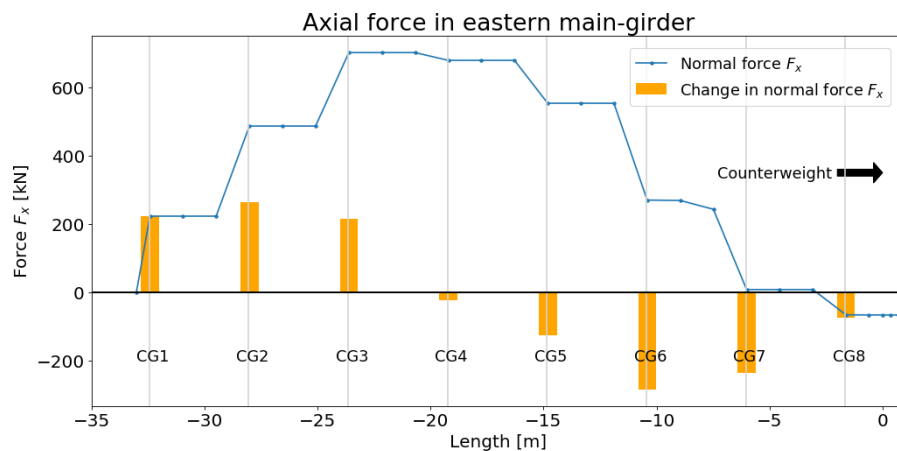


Figure 6.10: Section forces/moments in the eastern main-girder

In transverse direction, the deck is well restrained which results in transverse connector forces F_y that are from a lower order which can be seen in figure 6.12b. Generally, it can be observed that between the two main-girders, the forces F_y are having a similar distribution as in the composite beam model. In the middle of the cross-girders, the connectors are not loaded while at the extremities near the main-girders, the maximum forces are measured. This is due to the sagging of the cross-girders between the main-girders.

Near the cross- to main-girder connections, it can be observed that the forces in transverse direction of a connector pair can have different signs. The difference of the forces is the largest near the main-girder. The effect is caused by the weak axis bending of the cross-girder. Because the cross- to main-girder has a limited rotational stiffness that allows the weak axis bending of the cross-girder, the two deck-to-girder connections can rotate along with the cross-girder around its rotation point. The effect is visualised in figure 6.11 for the connection with the absolute maximum transverse force at cross-girder 6. The effect of weak axis bending of the cross-girders is further elaborated in section 6.4.

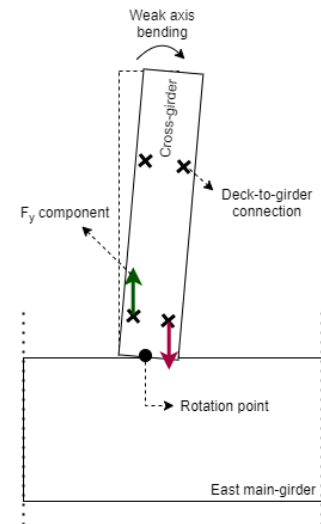


Figure 6.11: Effect of weak axis bending on transverse force in deck-to-girder joint (top-view cross- to main-girder connection)

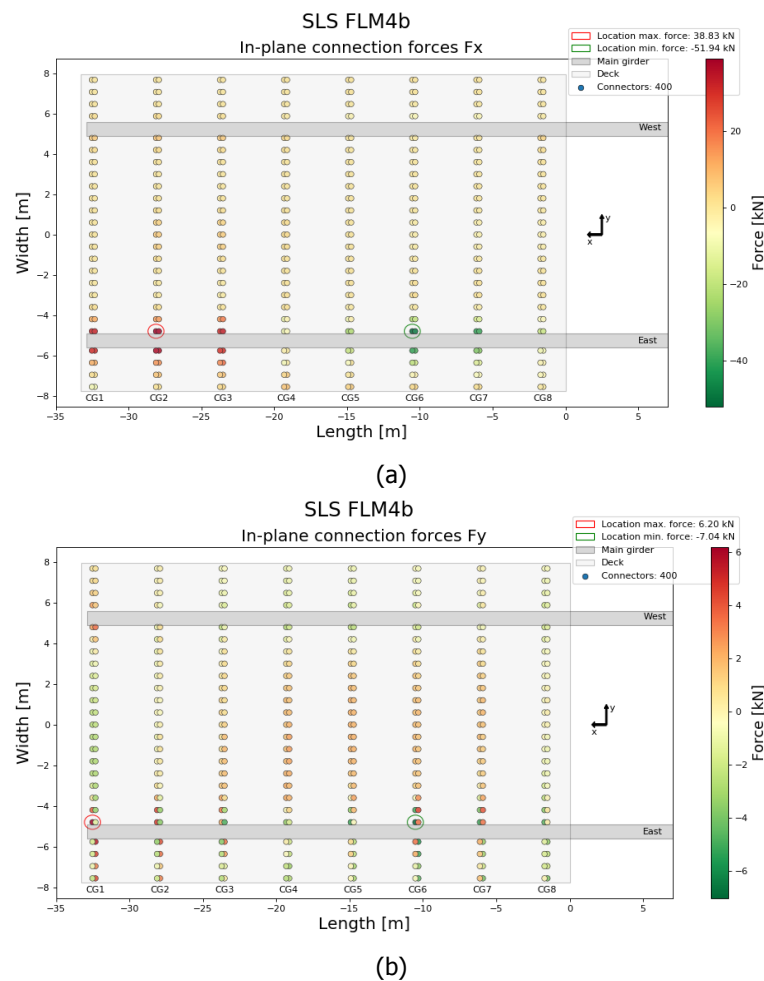


Figure 6.12: Deck-to-girder connection force-states longitudinally F_x (a) and transversely F_y (b)

Thermal loading

The thermal loading of the FRP deck causes it to expand in both longitudinal and transverse direction. In non-hybrid structures, where the deck can move freely relative to the steel superstructure, no shear forces are generated at the FRP-steel interface. But as a consequence of engaging the deck to the steel girders to exploit hybrid interaction, the expansion is restricted by the deck-to-girder connections. This involves large forces that are generated at the FRP-steel interface.

Figure 6.13 proves the previous statement because the maximum forces in both directions are measured at the outer edges of the deck where the expansion displacements are the largest. The longitudinal forces in the connections are exceeding the slip limit of the M20 10.9 bolt. Again, the longitudinal force is mainly concentrated near the stiff cross- to main-girder connections. Because the longitudinal expansion of the deck is the largest at the start and end of the deck, the largest forces are measured on the first and eight cross-girder.

The plot of the transverse connection forces reveals the symmetric expansion of the deck which grows towards the eastern and western edges of the deck. At these edges, the maximum force measured in the connections is 36 kN. Due to the longitudinal expansion of the deck, weak axis bending of the cross-girders is occurring mostly near the first and last cross-girder. Therefore, it seen that near the cross- to main-girder connection of cross-girder 1 and 8, a connector pair can have different transverse force values. Further away from the cross- to main-girder connection, connector pairs have equal transverse force values.

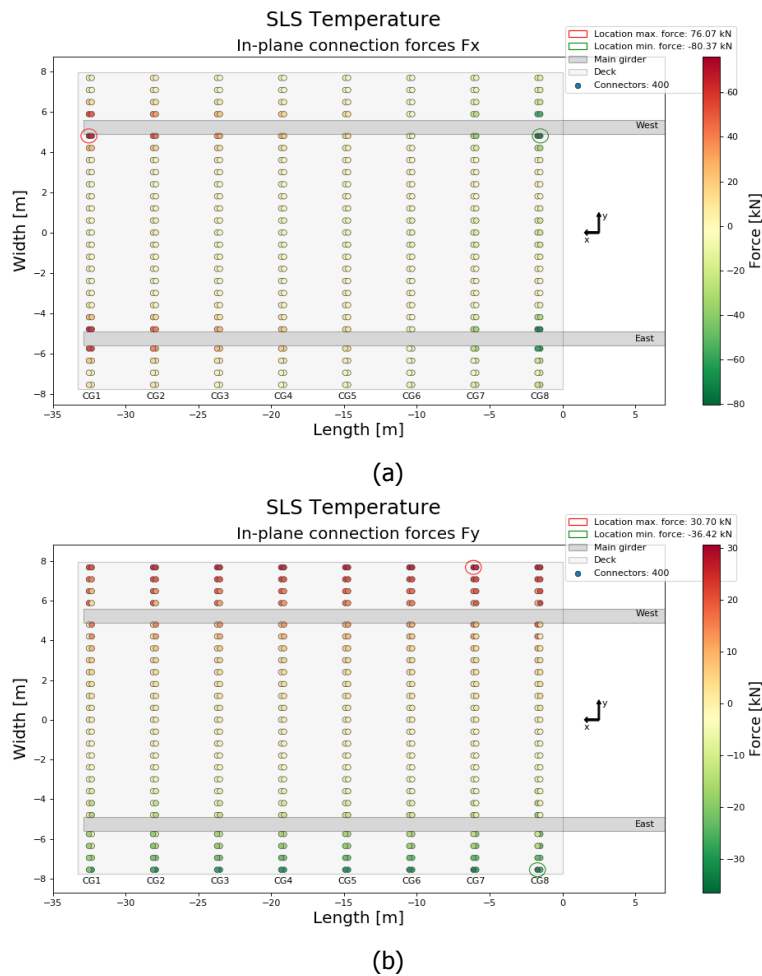


Figure 6.13: Deck-to-girder connection force-states longitudinally F_x (a) and transversely F_y (b)

Combination

The maximum forces generated by the load combinations are presented in table 6.3. It is clear the governing combination is found when thermal loading is the leading variable load case. The connector forces generated by this load combination are presented in figure 6.14. The maximum shear force measured in the deck-to-girder connections was $F_{v,Ed} = 94.12kN$.

Table 6.3: Maximum connector forces from the load combinations expressed in table 6.2

Leading load case		F_x [kN]	F_y [kN]
SLS	Traffic	73.85	22.5
	Thermal	94.12	36.46

In order to check whether the occurring forces are not exceeding the design slip resistance, the knowledge from section 5.4 about the influence of friction is used. In this section, a friction force factor $\alpha_{friction}$ was defined that expresses the influence of friction at the FRP-steel interface on the connector forces. The study showed that when assuming a friction coefficient of 0.2 at the FRP-steel interface, the connector forces from the global model could be reduced by 11%. Therefore, the check for the connector forces in SLS result in:

$$\alpha_{friction} * F_{v,Ed} < F_{s,Rd}$$

$$0.89 * 94.12kN = 84kN < 55kN \quad \text{Not satisfied UC}=1.53$$

The high longitudinal forces near the cross- to main-girder connections cause the design check to be unsatisfactory. A solution to this localised effect would be to connect the FRP deck to the main-girder or to have bolts with a larger diameter installed near the cross- to main-girder connection. An M27 10.9 bolt would be able to resist the shear force of 84 kN as the slip resistance is equal to $F_{s,Rd} = \frac{0.7 * A_s f_{u,b} \mu}{\gamma_{M3,ser}} = \frac{0.7 * 459 * 1000 * 0.35}{1.1} = 102kN$. The solution of installing connectors on the main-girders is discussed in section 6.3.

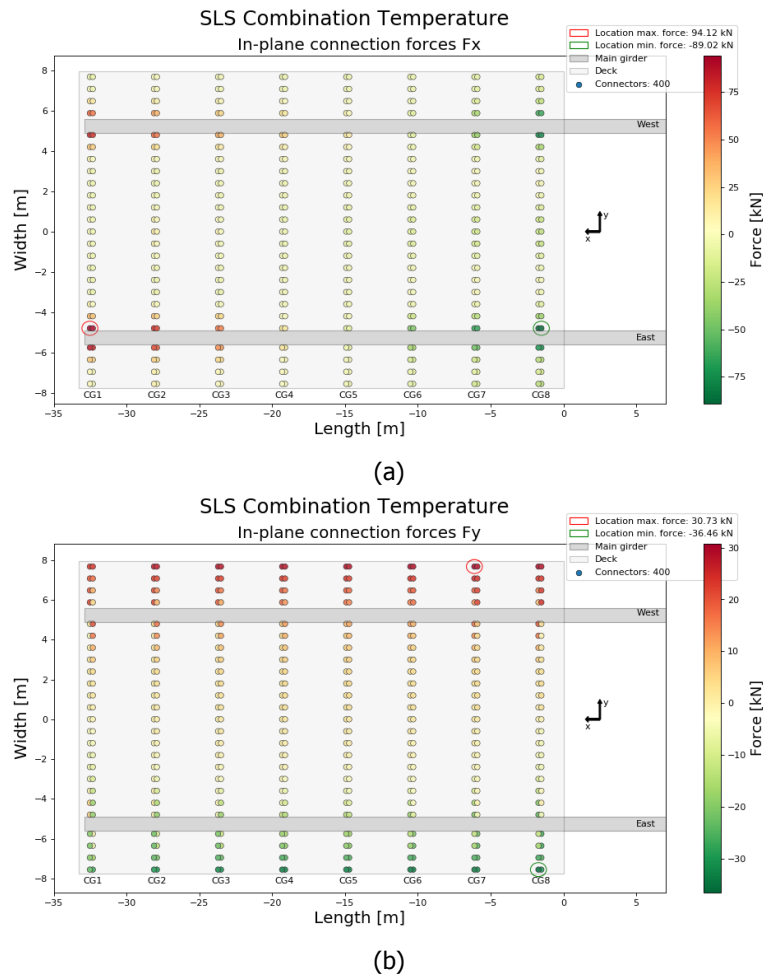


Figure 6.14: Deck-to-girder connection force-states longitudinally F_x (a) and transversely F_y (b)

6.2.2. Ultimate limit state

Checking the connectors in the ultimate limit state, the shear forces in the connections should not exceed their ultimate design resistance $F_{v,Rd} = 118kN$. The deck-to-girder connections are assigned with the lower bound stiffness $k_{sc,lower} = 67kN/mm$ as determined in chapter 4. Firstly, the results from the individual LM1 and thermal load cases are presented after which the combinations are discussed.

Traffic load model 1

Table 6.4 summarises the absolute maximum connection force measured in the deck-to-girder connections due to traffic loading. When the tandem systems are positioned around the mid-span region (positions 1, 2 & 3), the longitudinal and transverse connection forces are maximised. Although figures 6.15b and 6.15b present the governing load cases for longitudinal and transverse forces respectively, the visualisation of the connector forces for all tandem positions are given in appendix D.2.

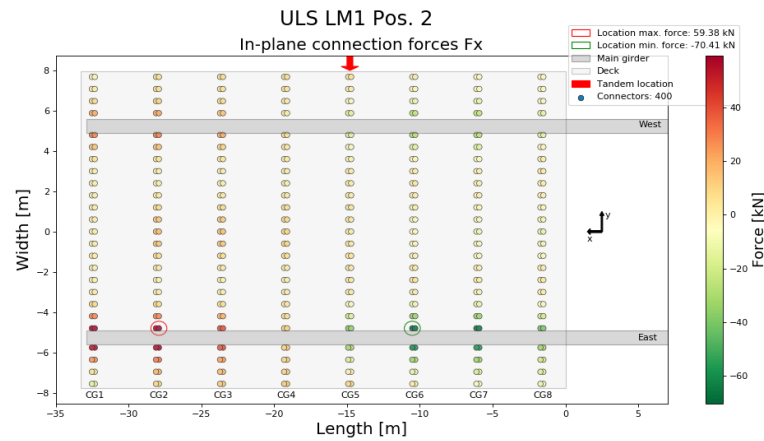
Table 6.4: Maximum longitudinal F_x and transverse F_y connection forces

LM1 Traffic	Position 1	Position 2	Position 3	Position 4	Position 5
F_x [kN]	67.53	70.41	67.98	29.75	40.70
F_y [kN]	11.53	10.43	9.59	11.16	10.71

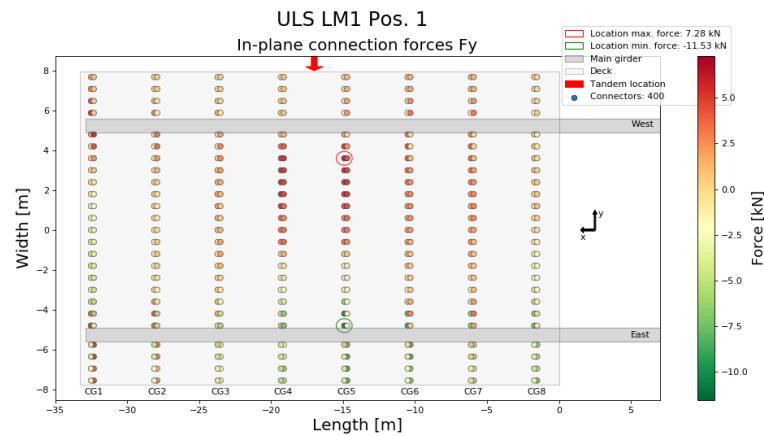
Figure 6.15a presents the traffic load case for which the longitudinal load case is maximised. Positioning the tandem system above the fifth cross-girder reveals the longitudinal connection force can lead to 70.41 kN. The same kind of force distribution is observed as in the FLM4b load case (figure

6.12a). The longitudinal forces are mainly concentrated around the cross- to main-girder connections for the same reason as discussed earlier. Because of the composite action of the deck with the cross-girders, the longitudinal shear flow between those elements are concentrated at the stiff cross- to main-girder connections.

The maximum longitudinal and transverse connector force are respectively measured at 70.41 kN and 11.53 kN which is below the ultimate resistance of 118 kN. This indicates that the deck is sufficiently supported by the iSRR connectors in longitudinal and transverse direction. The switching of the transverse force signs near the cross- to main-girder axis due to weak axis bending of the cross-girders, is also apparent.



(a)



(b)

Figure 6.15: Connection force-states longitudinally F_x with LM1 tandem at position 2 (a) and transversely F_y with LM1 tandem at position 1 (b)

Thermal loading

Due to the thermal expansion of the deck, large connector forces are measured at the edges of the deck. Although in SLS the same thermal load is applied to the FRP deck, the connector forces in ULS are lower than in SLS. This is because of the difference in connector stiffness. During the SLS check, the connector stiffness $k_{sc,upper} = 212\text{kN/mm}$ is higher than during the ULS check $k_{sc,lower} = 67\text{kN/mm}$. The higher stiffness means that larger forces are measured for the same displacement.

Figure 6.16 shows that the longitudinal and transverse are less than 50.95 kN and 26.8 kN, respectively. The distribution of the forces is similar to the figures 6.13 from the SLS checks. The longitudinal forces are mainly concentrated at the cross- to main-girder connections and for the transverse forces you have unequal forces in the same connector pair at the first and last cross-girder.

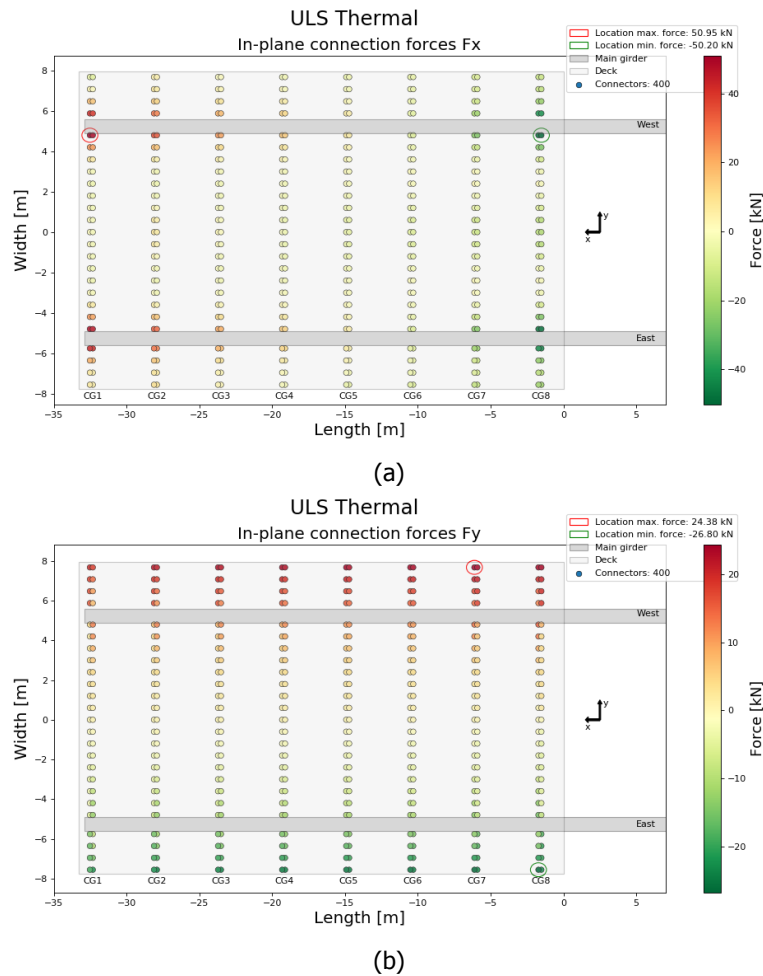


Figure 6.16: Deck-to-girder connection force-states longitudinally F_x (a) and transversely F_y (b)

Combination

Since the largest connector forces were generated by positioning the tandem systems at position one and two, the maximum forces are measured combining both positions with the thermal load case. Table 6.5 presents the result of these combinations and shows that position one maximises the connector forces.

Table 6.5: Maximum connector forces from the load combinations expressed in table 6.2

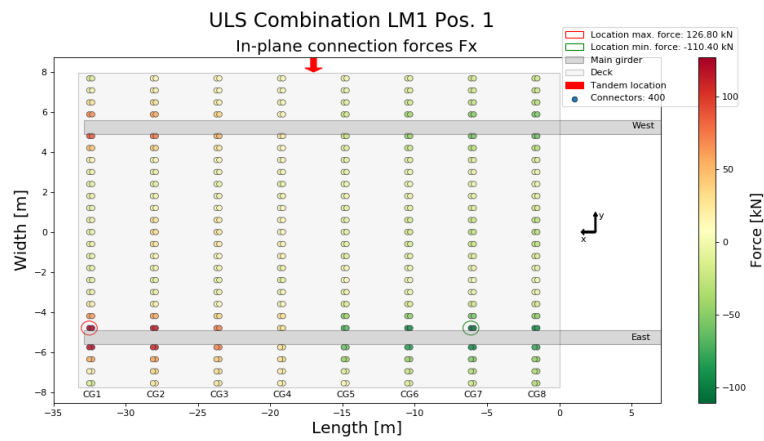
LM1 position Leading load case		1		2	
		F_x [kN]	F_y [kN]	F_x [kN]	F_y [kN]
ULS	Traffic	126.8	24.37	120.6	32.69
	Thermal	120.2	43.28	115.6	42.75

To maximise the longitudinal forces, the combination where traffic LM1 is leading results in the largest connector force of 126.8 kN. For the transverse force, the thermal-led combination is governing. The check if the maximum shear force is exceeding the ultimate resistance of the connector, is performed using the same friction factor as discussed for the SLS checks 6.2.1. The check then results in:

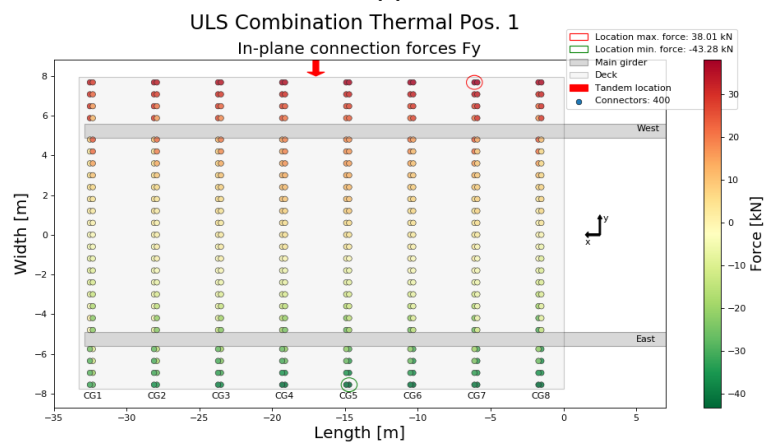
$$\alpha_{friction} * F_{v,Ed} < F_{Rd}$$

$$0.89 * 126.8kN = 113kN < 118kN \quad \text{Satisfied UC}=0.96$$

Although the design check is satisfied, the connector forces are mainly determined by the large longitudinal forces near the cross- to main-girder connections. The other connections in the system are hardly near the ultimate resistance of the connector. As the same conclusion was made during the SLS checks, it is proposed to connect the FRP deck to the main-girder. The effect of connecting the connections to the main-girder are discussed in the next section 6.3.



(a)



(b)

Figure 6.17: Deck-to-girder connection force-states longitudinally F_x (a) and transversely F_y (b)

6.3. Connecting the main-girder

The previous section showed that highly localised forces are apparent near the cross- to main-girder connections. This was due to the insufficient connection between the main-girder and the FRP deck. Therefore, it was proposed to connect the main-girder to the FRP deck. This means that connectors have to be installed inside the box section of the main-girder.

By adding a connector pair every 700 mm along the main-girder, the distribution of connectors results in the one presented in figure 6.18. As a result of the addition of connectors, the total amount of connector increases by 43% from 400 to 572 connectors. For this distribution, the same analyses are performed as presented in 6.2. Firstly, the results for the serviceability limit state are compared and secondly for the ultimate limit state. The results from all load cases can be found in appendix D.3.

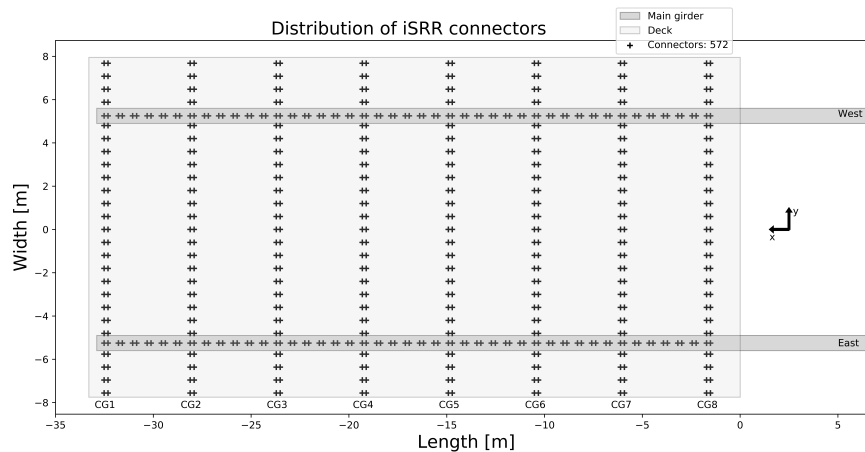


Figure 6.18: Distribution of the iSRR connectors when connecting the main-girder

Serviceability limit state

Table 6.6 compares the maximum force results from the original renovation design, where the cross-girders are only connected to the FRP deck, to the design where the main-girders are connected as well. The table summarises the maximum forces in both longitudinal as transverse direction for all load cases and combinations.

Comparing the values from the original renovation design to the new design, a large decrease in mainly longitudinal forces is observed. Once again, the load combination with thermal loading as the leading case, is the governing load combination. The maximum forces dropped by 43% from 94 kN to 53.95 kN. This is a result from the increased longitudinal support of the FRP deck on the main-girders. The effect of attaching the FRP deck to the main-girder, mainly affects the longitudinal connection forces but also the transverse forces are reduced by roughly 10%.

Examining the longitudinal forces in figure 6.19a, it can be noticed that they gradually increase on the main-girders towards the edges of the deck. This is expected since the thermal expansion displacements are the largest near the deck ends. Connecting the main-girders to the deck allows the maximum shear force of 53.95 kN to satisfy the design check as follows:

$$\alpha_{friction} * F_{v,Ed} < F_{s,Rd}$$

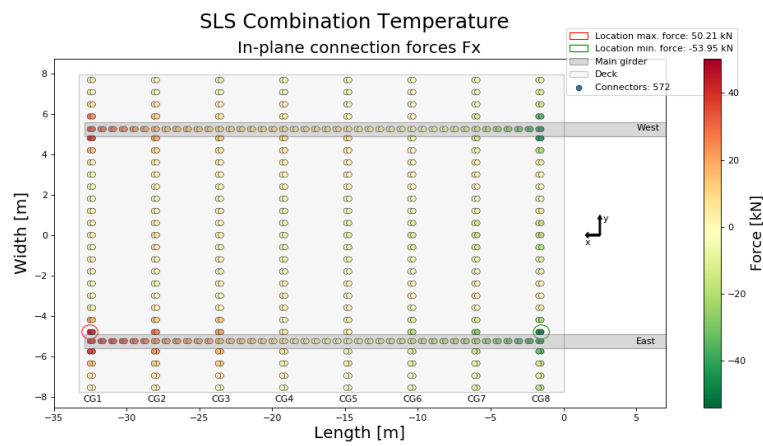
$$0.89 * 53.95kN = 48kN < 55kN \quad \text{Satisfied UC}=0.87$$

The transverse connection forces are less influenced by the addition of the connections on the main-girder because the FRP deck was already well supported in transverse direction. But by comparing the transverse forces near the connection of the main-girder with the first and last cross-girder, it can be

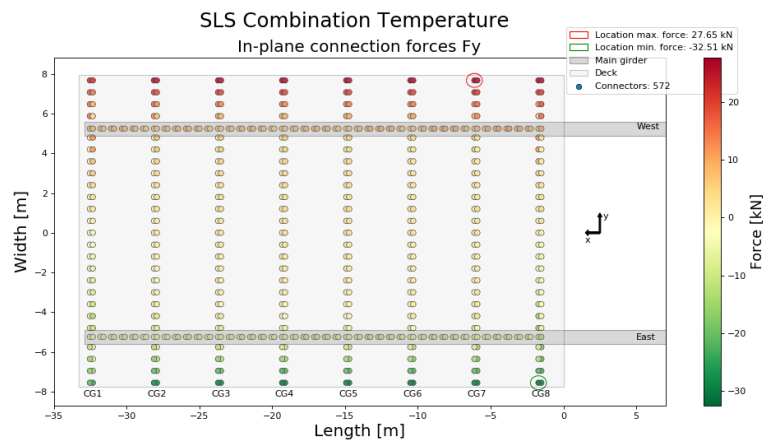
seen that the difference in forces in the same connector pair are less than when the connections are only connected to the cross-girders. This might suggest that the weak axis bending of the cross-girders is less when the main-girders are connected as well.

Table 6.6: Maximum longitudinal F_x and transverse F_y connection forces

		Connecting only cross-girders	Connecting cross- and main-girders	Difference
FLM4b	F_x [kN]	51.94	27.07	- 48%
	F_y [kN]	7.04	4.37	- 38%
Thermal	F_x [kN]	80.37	51.23	- 36%
	F_y [kN]	36.42	33.06	- 9%
Combination traffic leading	F_x [kN]	73.85	36.83	- 50%
	F_y [kN]	22.5	20.55	- 9%
Combination thermal leading	F_x [kN]	94.12	53.95	- 43%
	F_y [kN]	36.46	32.51	- 11%
Maximum	F [kN]	94.12	53.95	- 43%



(a)



(b)

Figure 6.19: Deck-to-girder connection force-states longitudinally F_x (a) and transversely F_y (b)

Ultimate limit state

The positive effect of connecting the FRP deck to the main-girders is also clear from the results presented in table 6.7. Positioning the tandem system at position 1 and combining it with the secondary thermal load, delivers a maximum shear force of 69 kN in the deck-to-girder connections. Comparing that to the 126.8 kN from the original renovation design, it is a reduction of 46%. As was seen in the serviceability limit state, mainly the longitudinal forces are affected by the connection of the FRP deck to the main-girder.

The plot of the longitudinal connection forces in figure 6.21a, shows the effectiveness of the new connection distribution. Because the heaviest LM1 loads are on the eastern side of the bridge, the largest forces are occurring near the eastern main-girder. The distribution of the connector forces along the eastern main-girder demonstrates the engagement of the FRP deck with the main-girder as the forces grow towards the extremities of the main-girder. Comparing the location of the maximum force from figure 6.17a and 6.21a, the maximum connector load has shifted from the cross- to main-girder connection to a connection on the main-girder. Having a maximum value of 69 kN, the connection satisfies the ULS check:

$$\alpha_{friction} * F_{v,Ed} < F_{Rd}$$

$$0.89 * 69kN = 61kN < 118kN \quad \text{Satisfied UC}=0.52$$

Figure 6.20 zooms in on the connector forces near the intersection of the eastern main-girder and the second cross-girders under the governing ULS load combination presented in figures 6.17a and 6.21a. The longitudinal forces are plotted of one row deck-to-girder connectors at the level of the cross-girder. The figure shows that the forces are better distributed near the cross- to main-girder connection when the main-girders are connected to the FRP deck. It can be regarded that the effective width of the FRP panel above the main-girders is larger in this case. When the main-girders are not connected, the deck is less engaged in longitudinal direction resulting in a lower effective width and eventually less composite action.

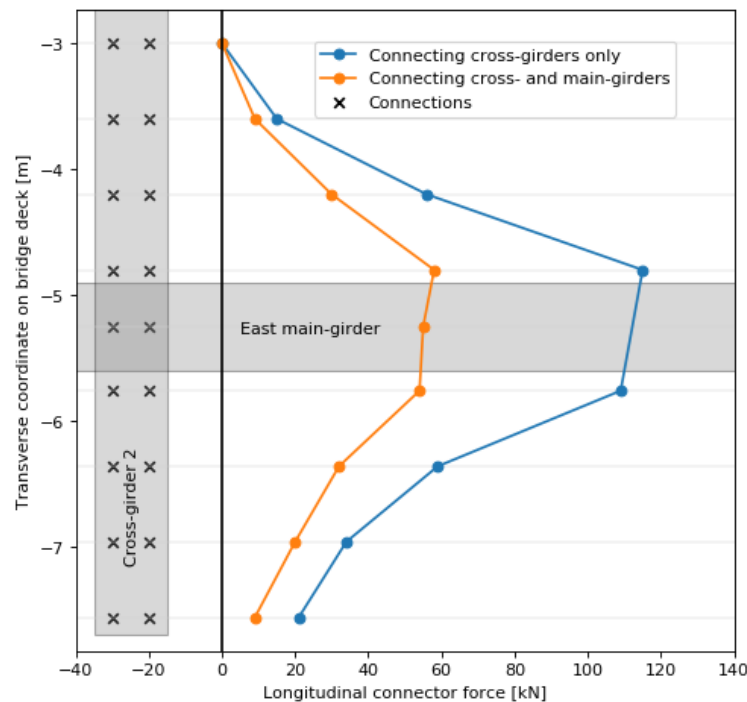
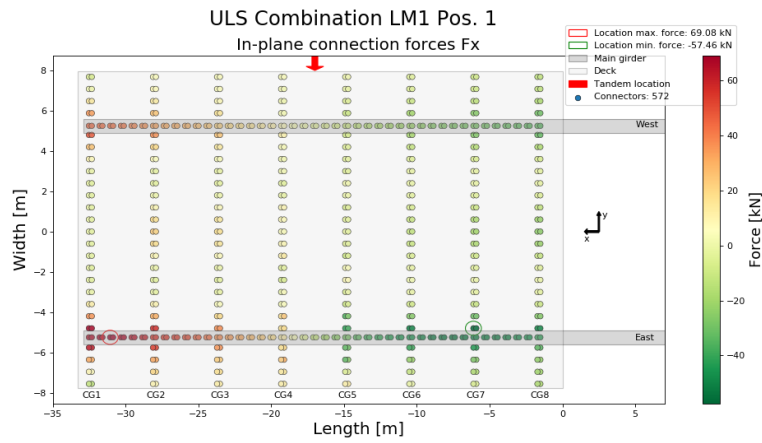


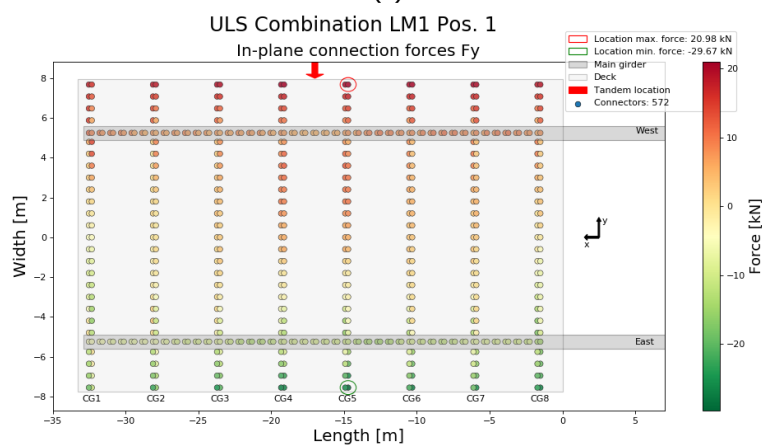
Figure 6.20: Longitudinal force distribution near the connection of cross-girder 2 with the eastern main-girder

Table 6.7: Maximum longitudinal F_x and transverse F_y connection forces

		Connecting only cross-girders	Connecting cross- and main-girders	Difference
LM1 Pos. 1	F_x [kN]	67.53	37.16	- 45%
	F_y [kN]	11.53	8.17	- 29%
LM1 Pos. 2	F_x [kN]	70.41	39.53	- 44%
	F_y [kN]	10.43	8.09	- 22%
Thermal	F_x [kN]	50.95	35.45	- 30%
	F_y [kN]	26.8	23.94	- 11%
Combination traffic Pos. 1 leading	F_x [kN]	126.8	69.08	- 46%
	F_y [kN]	33.33	29.67	- 11%
Combination thermal Pos. 1 leading	F_x [kN]	120.2	68.58	- 43%
	F_y [kN]	43.28	38.14	- 12%
Combination traffic Pos. 2 leading	F_x [kN]	120.6	65.2	- 46%
	F_y [kN]	32.69	28.21	- 14%
Combination thermal Pos. 2 leading	F_x [kN]	115.6	65.98	- 43%
	F_y [kN]	42.75	37.04	- 13%
Maximum	F [kN]	126.8	69.08	- 46%



(a)



(b)

Figure 6.21: Deck-to-girder connection force-states longitudinally F_x (a) and transversely F_y (b)

6.4. Comparison with timber deck

Chapter 3 presented the current state of the Beneden Merwede bridge including its flaws. One of the issues presented, was the insufficient static capacity of the cross- to main-girder connection. During the reassessment of the bridge, it was found that the yield strength was exceeded at the connections. The large stresses were caused by the combination of weak- and strong-axis bending of the cross-girders due to load combinations where permanent and traffic loads were dominant.

In order to show the potency of the proposed renovation design, a comparison is made between the original model with the timber deck and the FRP renovation design with and without the connection of the main-girder to the FRP deck. Since the steel superstructure is examined, it is subjected to the permanent loading of the FRP deck. Because this section presents only the comparison between the models, unfactored load cases are considered for permanent loading and traffic LM1 loading. In case of the models for the renovation design with the FRP deck, the deck is connected with the underlying girders using the upper bound stiffness $k_{sc,upper} = 212\text{kN/mm}$.

6.4.1. Cross- to main-girder connection

As one of the current issues with the Beneden Merwede bridge are the cross- to main-girder connections, the influence of the renovation design on the bending moments in the connections are studied for permanent and traffic load cases. Tables 6.8 and 6.9 present respectively the maximum strong and weak axis bending moments in the cross- to main-girder connections.

Investigating the maximum values for the strong axis bending moments, no major differences are found. The largest percentual difference is found for the permanent load case. This is because of the self-weight reduction as a result from the replacement of the timber deck and secondary girders by an FRP deck. The self-weight from the replaced elements (1.97kN/m^2) are substituted by the self-weight from the FRP deck (1.137kN/m^2). This leads to a $\pm 15\%$ reduction of strong axis moments in the cross- to main-girder connections.

Table 6.8: Comparison strong axis bending moments

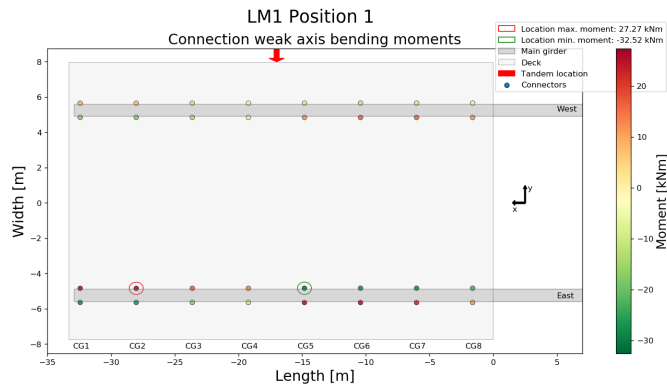
in [kNm]	Permanent	LM1 traffic				
		Pos. 1	Pos. 2	Pos. 3	Pos. 4	Pos. 5
Reference timber deck	106.3	365.8	486.9	459.9	578.4	518.3
Renovation design: cross-girders connected	91.8	361	470.8	448	582.3	508.8
Renovation design: cross+main-girders connected	88.62	355.2	464.7	440.9	578.6	509.5

Evaluating the weak axis bending moments in table 6.9, a significant reduction is found when employing the renovation design which includes deck-to-girder connections on the main-girders. When only the cross-girders are connected in the renovation design, the difference with the original timber deck is only noticeable for permanent loading due to the self-weight reduction.

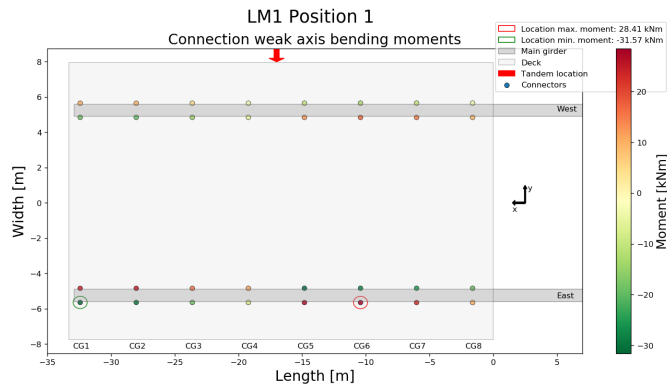
When positioning the tandem system at position 1 and connecting the deck to the main-girders, a weak axis bending moment reduction of 30% is achieved compared to the original model with the timber deck. A reduction of the same magnitude is also found for the other load cases. The reason why the weak axis bending moments are significantly reduced when connecting the main-girders is because the FRP deck acts as a diaphragm on top of the cross- to main-girder connections. This increases the stiffness of the cross- to main-girder connection against weak axis bending of the cross-girder. When the main-girder is not connected to the FRP deck, the relative rotation between the cross- and main-girders is not restrained and rotations as indicated in figure 6.11 are still possible.

Table 6.9: Comparison weak axis bending moments

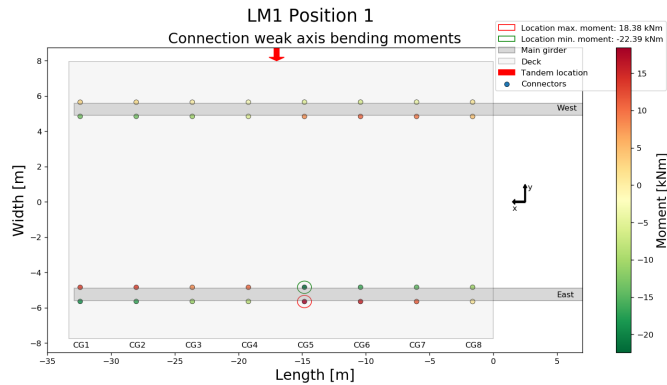
in [kNm]		Permanent	LM1 traffic				
			Pos. 1	Pos. 2	Pos. 3	Pos. 4	Pos. 5
Reference timber deck		12.5	32.52	31.47	30.78	13.56	19.29
Renovation design: cross-girders connected	cross-	9.92	31.57	31.33	33.61	16.01	17.72
Renovation design: cross+main-girders connected	cross+main-	9.05	22.39	19.5	20.03	9.32	10.97



(a) Reference timber deck



(b) Renovation design: cross-girders connected



(c) Renovation design: cross+main-girders connected

Figure 6.22: Weak-axis bending of the cross- to main-girder connection

6.4.2. Main-girder bending and displacements

In order to investigate the global effect of the renovation design, the bending moments and displacements in the main-girders are studied. Figure 6.23 plots the bending moments and displacements of the eastern main-girder under the LM1 traffic loading with the tandem system located at position 1. The graphs include the results from both the original model with the timber deck as the renovation design with the FRP deck.

As can be seen from both graphs, the partial replacement of the timber deck and secondary girders by the FRP deck, has a minor influence on the global behaviour of the bridge. The global response of the bridge under vertical load cases is mainly dictated by the stiffness of the main-girders. For that reason, the addition of the relatively flexible FRP deck has a minimal effect on the global performance of the bridge.

As an example of the low composite action between the FRP deck and the main-girders, figure 6.20 can be re-examined. Although this graph plots the longitudinal forces in the deck-to-girder connections, the distribution can be interpreted as the longitudinal shear flow that is transferred between the deck and main-girder which causes a shear lag effect. This means that only a minor part of the FRP deck is contributing to the bending stiffness of the main-girder.

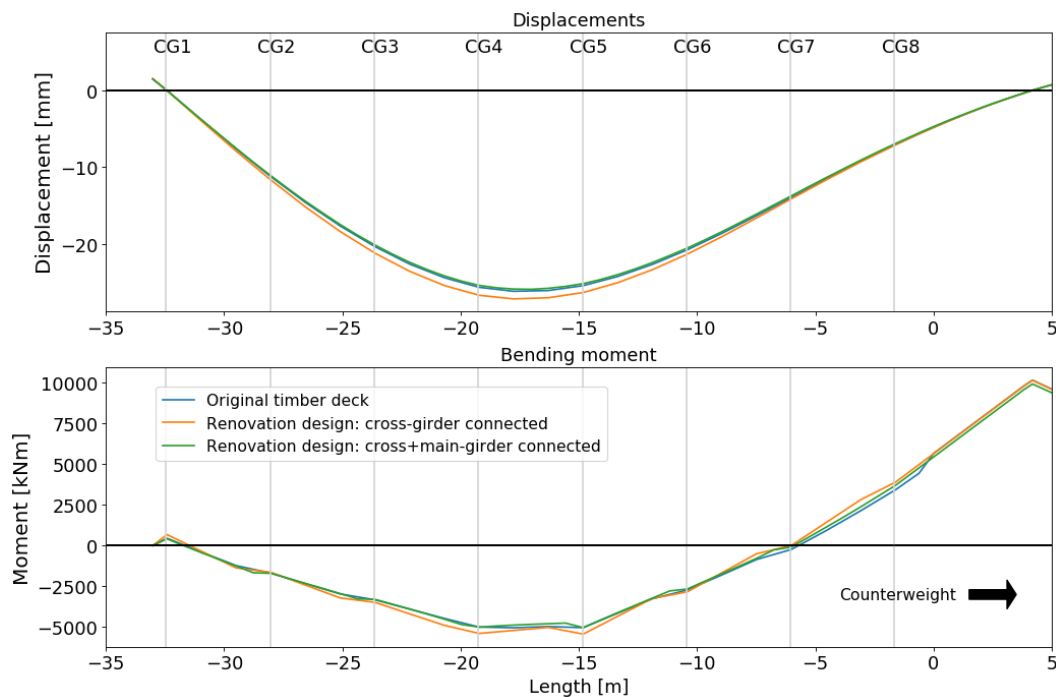


Figure 6.23: Displacement and moment comparison of the eastern main-girder under traffic LM1 loading with the tandem system located at position 1

6.5. Summary

This chapter focused on delivering an answer to the fourth and last objective 4. Using the modelling techniques developed in chapter 5, a global bridge model was made. The bridge model was used to analyse the FRP-steel connection forces that were generated by critical load cases. Based on different bolt placement configurations, a recommendation was made for the positioning of the connections. The main outcomes of this chapter are listed below:

- The bridge model, used during the reassessment of the Beneden Merwede bridge, was fitted with an FRP deck having the properties from tables 3.2 and 3.3. The FRP deck was connected to the underlying steel superstructure using linear springs. The stiffness of the springs depended on the limit state check.
- The deck-to-girder connections were checked in the serviceability (SLS) and ultimate (ULS) limit state. As mentioned in section 4.2.2, the linear springs were assigned with the upper bound stiffness $k_{sc,upper} = 212kN/mm$ in SLS and the lower bound stiffness $k_{sc,lower} = 67kN/mm$ in ULS. In SLS, the situation was considered that the bridge was realistically loaded. The heaviest truck from fatigue load model 4 was combined with the thermal heating of the FRP deck. For this combination, the forces in the connections should not exceed the design slip force $F_{s,Rd} = 55kN$. In ULS, the resistance of the connectors was compared to the occurring forces. The shear force in the connections should not exceed the design strength $F_{Rd} = 118kN$. In this situation, it was assumed that the bridge was full of traffic (LM1) and the deck was heated.
- For the first iteration of the deck-to-girder connection distribution, it was assumed that all iSRR connections were placed on the accessible cross-girders. Every 600 mm, a pair of iSRR connections (modelled as linear springs) connected the top flange of the cross-girder with the bottom facing of the FRP deck. Using this distribution, a total of 400 connections were used. Investigating the deck-to-girder connections in SLS and ULS, the following observations were made concerning the connection distribution:
 1. In **SLS**, thermal expansion was the leading load case for the governing combination. Large longitudinal forces were found near the cross- to main-girder connections as a result of the composite action between the FRP deck and the main-girders. The connection forces in transverse direction were mainly generated by the thermal expansion of the deck but remained below the slip limit $F_{s,Rd}$. Nonetheless, the longitudinal connector forces near the cross- to main-girder connections caused the design check to be unsatisfactory (UC=1.53). As a solution to this local effect it was suggested to connect the FRP deck to the main-girder or to have bolts with a larger diameter installed near the cross- to main-girder connections. An M27 10.9 bolt would be able to resist the occurring shear force at these locations.
 2. In **ULS**, the connector forces due to thermal loading were generally lower due to the reduced stiffness of the connectors. Yet, positioning the LM1 tandem system at mid-span caused large longitudinal shear forces which were also concentrated at the cross- to main-girder connections. Having an ULS unity check of 0.96, the deck-to-girder connections were almost fully utilised near the main-girders.
- Connecting only the cross-girders to the FRP deck produced large longitudinal shear forces near the cross- to-main-girders connections. Therefore, it was suggested to connect the main-girders to the FRP deck. The same analyses were performed including the addition of 172 connectors which were distributed every 700 mm in pairs on the main-girders. Comparing the results from the new connector distribution to the original distribution with only iSRR connectors on the cross-girders, the following observations were made:
 1. In **SLS**, the longitudinal forces near the cross- to main-girder connection were reduced by 43% as a result of the increased longitudinal support of the FRP deck on the main-girders. The transverse shear forces in the deck-to-girder connections were reduced by a smaller 10% because the deck was already sufficiently supported transversely. Connecting the main-girders to the deck allowed the maximum shear force to satisfy the unity check of 0.87.

2. In **ULS**, the positive effect of connecting the FRP deck to the main-girders was also clear from the 46% maximum force reduction in the deck-to-girder joints. This resulted in a largely sufficient design check of $UC=0.52$. Figure 6.20 also demonstrated that the longitudinal forces are better distributed near the cross- to main-girder connection when the main-girders are connected to the FRP deck. When the main-girders are not connected, the deck is less engaged in longitudinal direction. This results in a lower effective width of the deck panel above the main-girders and eventually less composite action.
- In order to show the potency of the proposed renovation design, a comparison was made between the original model with the timber deck and the FRP renovation design with and without the connection of the main-girders to the FRP deck. As one of the current issues with the Beneden Merwede bridge are the cross- to main-girder connections, the influence of the renovation design on the strong and weak axis bending moments in those critical connections were studied for permanent and traffic load cases. Moreover, the global effects of the renovation design on the main-girder displacements and bending moments were investigated. The following remarks were noted:
 1. Investigating the maximum values for the strong axis bending moments, no major differences were found. The largest percentual difference was found for the permanent load case. This was explained by the self-weight reduction as a result from the replacement of the timber deck and secondary girders by an FRP deck. The self-weight from the replaced elements (1.97 kN/m^2) was substituted by the self-weight from the FRP deck (1.137 kN/m^2). This led to a $\pm 15\%$ reduction of strong axis bending moments in the cross- to main-girder connections.
 2. A significant reduction of the weak axis bending moments was found when employing the renovation design which includes deck-to-girder connections on the main-girders. When only the cross-girders were connected in the renovation design, the difference with the original timber deck was only noticeable for permanent loading due to the self-weight reduction. When connecting the FRP deck to the main-girders, the weak axis bending moments were reduced by 30% compared to the original model with the timber deck. The reason for this significant reduction in weak axis bending moments was explained by the diaphragm action of the FRP deck on top of the cross- to main-girder connection. This increases the stiffness of the cross- to main-girder connection against weak axis bending of the cross-girder.
 3. The partial replacement of the timber deck and secondary girders by the FRP deck, had a minor influence on the global behaviour of the bridge. The global response of the bridge under vertical load cases is mainly dictated by the stiffness of the main-girders. For that reason, the addition of the relatively flexible FRP deck had a minimal effect on the global performance of the bridge. The main-girder displacements and bending moments were almost equal in all three models.

7

Conclusions & recommendations

7.1. Conclusions

The main objective of this thesis was to investigate the behaviour of deck-to-girder connections in FRP-steel composite bridges with the application of renovating movable highway bridges with a timber deck. Using a series of finite element models, the application of the iSRR connection for the renovation of the Beneden Merwede bridge was investigated on three levels: the connection, composite beam and bridge level.

The analysis of the iSRR connection with the embedded nuts and coupler showed that both configurations have a similar static behaviour which was well predicted by analytical approximations. Based on the known long-term behaviour of the iSRR connection with the embedded nuts, it was advised to use this type of configuration as deck-to-girder joint.

Applying the iSRR connection on the composite beam model every 600 mm, the connections provided full composite action between the FRP deck and the steel girder and preserved the interaction between the two components until yielding of the steel beam was initiated. The composite beam analysis also concluded that connection forces may be reduced when friction is not taken into account during the analysis, e.g. during engineering analysis with linear springs in GSA. Assuming a friction coefficient of 0.2, the reduction of the deck-to-girder connection forces is at least 11%.

Investigating the deck-to-girder connections on the bridge level, it was advised to install iSRR connections on the cross- and main-girders to connect the FRP deck. Using 572 connectors supporting the FRP deck in longitudinal and transverse direction of the bridge, the design resistance of the preloaded iSRR connections was not exceeded. When connecting the FRP panel to the cross- and main-girders, the bending moments in the cross- to main-girder connections were reduced up to 30% compared to the original design of the bridge with a timber deck.

The following paragraphs list the conclusions about the individual research questions formulated in section 1.2. The first analyses of the iSRR connection are performed by a push-out test having the geometry recommended by Eurocode 4. Therefore, it can be regarded that these results can be generalised. The geometry of the composite beam model and the bridge model are based on the dimensions of the Beneden Merwede bridge. Accordingly, the conclusions of those analyses are applicable to bridges with similar structural lay-outs and comparable spans.

Shear behaviour of the iSRR connection

The first part of this thesis characterised two types of injected steel reinforced resin (iSRR) connectors, the coupler and embedded nuts configuration, in order to answer the first research question:

What is the load-displacement behaviour of the iSRR connection configurations, and which one is most suitable as deck-to-girder connection in movable highway bridges with FRP deck panels?

- The static performance of the iSRR connection with the coupler and the embedded nuts showed similar static behaviour. Bolt rupture defined the ultimate resistance of the iSRR connections which was well approximated by hand calculations at 147 kN. As only minor damages were observed to the FRP panel, the panel could be used in a next life-cycle. Slipping of the fully preloaded connections was observed at a slip force of 60 kN which also corresponded with analytical approximations.
- Because the static performance of the coupler configuration had no significant advantage over the embedded nuts configuration, it was advised to use the iSRR connection with the embedded nuts as a safe design choice. The recommendation was based on practical considerations and available knowledge about the fatigue and creep performance of the embedded nuts configuration. For the design procedure of the iSRR connection with the embedded nuts, two secant stiffness moduli were defined:
 - The stiffness before slipping is called the upper bound stiffness $k_{sc,upper}$ and will be used under service limit state (SLS) load levels to determine the deformations of the structure and forces in the bolt. In SLS, the upper bound stiffness $k_{sc,upper} = 212kN/mm$ should be used to check whether shear forces exceed the design slip resistance $F_{s,Rd} = 55kN$.
 - After slipping the stiffness is called the lower bound stiffness $k_{sc,lower}$ and will be used under ultimate limit state (ULS) load levels to determine whether or not the bolt forces exceed the design strength of the shear connection. In ULS, the lower bound stiffness $k_{sc,lower} = 67kN/mm$ should be taken to check whether the shear forces exceed the design shear resistance $F_{v,Rd} = 118kN$.

Flexural performance of the FRP-steel composite beam

The second part of this thesis focused on the structural behaviour of an FRP-steel composite beam and the finite element modelling of the deck-to-girder connections. (objective 2 and 3) The following conclusions are drawn regarding the second research question:

Investigating the mechanical performance of an FRP-steel composite system, what is the failure mechanism, degree of composite action, and effective width of the system?

- The numerical bending test of the composite beam was divided in a linear phase and a non-linear phase. During the linear phase, the stiffness of the composite beam was 13.2% higher compared to the stiffness of only the steel beam. The initiation of the non-linear phase and failure, was triggered by the yielding of the extreme tensile fibre of the steel beam at $90kN/m^2$. Eventually, the analysis was terminated at a pressure level of $130kN/m^2$ when a large part of the steel beam had yielded.
- The slip-resistant deck-to-girder connections provided full composite action until the first outer connection slipped at a pressure of $50kN/m^2$. During the ductile yielding the steel beam, no connections had failed but substantial damages were visible at the outer connections.
- An effective width of 3127 mm was achieved resulting in a shear lag factor of 0.71. Comparing the effective width of the FRP-steel composite beam to hand calculations for the effective width of concrete-steel beams, the effective width of the FRP-steel composite beam was 16% higher.

Regarding the modelling of the deck-to-girder connections, the next list answers the third research question:

How can the forces in deck-to-girder connections be efficiently determined in engineering-oriented software? And, what is the influence of friction at the FRP-steel interface on the forces in the deck-to-girder connections?

- In order to simulate the behaviour of the iSRR connections in engineering software, further simplifications of the FRP-steel connections were made and compared. The solid iSRR connectors from the initial composite beam test were replaced by non-linear fasteners in Abaqus, and linear springs in GSA. When properties of non-linear fasteners were matched with the results from the embedded nuts connection model and friction was modelled at the FRP-steel interface, it was demonstrated that the non-linear fasteners approximated the behaviour of the solid iSRR connections well while reducing the computation time 12 times. As engineering software is generally incapable of taking friction into account, the spring forces resulting from the analysis in GSA were compared with the Abaqus model having non-linear fasteners and excluding friction at the FRP-steel interface. Modelling the springs in GSA with the upper bound stiffness $k_{sc,upper} = 212 \text{ kN/mm}$ showed a comparable distribution of connection forces along the composite beam while reducing the analysis time dramatically from around one hour to a minute.
- To express the influence of friction on the connector forces, a friction force factor $\alpha_{friction}$ was introduced. The friction force factor expresses how much the connection forces are overestimated when friction is excluded from the analysis. Using the connector forces from the non-linear fasteners, it was calculated by dividing the results from the Abaqus model including friction ($\mu = 0.2$) with the results from the Abaqus model excluding friction ($\mu = 0$). A maximum friction force factor of $\alpha_{friction} = 0.89$ was found near the supports for multiple pressure levels. This means that connection forces may be reduced at least 11% when friction is not considered during the analysis, i.e. during engineering analysis with linear springs in GSA.

Behaviour of the bridge model

Using the knowledge of the first two parts of this thesis, the final part investigated the deck-to-girder connections on a large-scale bridge model of the Beneden Merwede bridge and therefore the last research question:

Under a number of load cases, which forces can be expected in the deck-to-girder connections on a movable highway bridge and to which elements should the connections be attached?

- When only the cross-girders were connected to the FRP deck, large shear forces in the deck-to-girder connections were observed. The largest forces were mainly concentrated near the cross-to-main-girder connections as a result of the composite action between the FRP deck and the main-girders. In SLS, thermal expansion was the leading load case for the governing combination. The longitudinal connector force of 94 kN near the cross- to main-girder connections caused the design check to be unsatisfactory (UC=1.53). In ULS, the largest connector force was 126.8 kN. After the multiplication with the friction force factor $\alpha_{friction}$, the design check sufficed with a unity check of 0.96.
When the cross- and main-girders are connected to the FRP deck, the largest forces in the deck-to-girder joints dropped significantly compared to the design where only the cross-girders are connected. The maximum shear force in deck-to-girder connection decreased by 43% in SLS and 46% in ULS. In both limit states, the design check sufficed having a unity check of 0.87 and 0.52 in SLS and ULS, respectively. It was demonstrated that the longitudinal forces are better distributed near the cross- to main-girder connection when the main-girders are connected to the FRP deck.
- A comparison was made between the original model with the timber deck and the FRP renovation design with and without the connection of the main-girders to the FRP deck. As one of the current issues with the Beneden Merwede bridge are the cross- to main-girder connections, the influence of the renovation design on the strong and weak axis bending moments of these critical connections were studied. The analyses showed that the strong axis bending moments in the cross- to main-girder connections were only reduced by the lower self-weight of the FRP deck. A significant reduction of the weak axis bending moments was found when employing the renovation design which includes deck-to-girder connections on the main-girders. A weak axis bending moment reduction of 30% was achieved compared to the original model with the timber deck due to the diaphragm action of the FRP deck on top of the cross- to main-girder connection. Therefore, it was recommended to connect the FRP deck to the cross- and main-girders.

7.2. Recommendations for further research

Based on the current uncertainties of the renovations method and the assumptions made for this thesis, a number of recommendations for further research are listed below:

- **Perform a parametric study of the iSRR connection**

Although the initial stiffness, slip behaviour and ultimate resistance of the iSRR connector were well approximated by the finite element models, the ductility after slipping was underestimated compared to the single-lap joint tests from Olivier and Csillag [28]. Push-out tests should be performed to validate the static performance of the iSRR connection with the embedded nuts and the constitutive model of the steel-reinforced resin should be verified by more material tests. When numerical modelling techniques are validated, a parametric study could be initiated to examine the performance of the connection using different design variables. Some examples of design parameters are: bolt diameter, flange thickness, FRP laminate thickness, diameter of the hole in the FRP and length of the threaded rod.

- **Optimise the design of the FRP panel**

The geometrical dimensions of the numerical composite beam test were set by the constraints of the renovation design. Due to the relatively high and slender vertical webs, the top facing of the FRP panel had practically no contribution to the overall bending stiffness of the composite beam. It is advised to explore mechanical solutions that would increase the engagement of the top facing. As an alternative, inclined webs could be added to the current FRP design that would transfer the shear forces between the top and bottom facing. Another suggestion could be to add vertical webs orthogonal to the spanning direction of the FRP deck but solely above the underlying steel beam.

- **Minimise the number of connectors for multiple load combinations**

For the distribution of the connectors on the underlying girders, uniform connector spacings were applied. A suggestion would be to explore non-uniform distributions to minimise the number of deck-to-girder connections. It has to be taken into account that only elementary load cases were considered to determine the connector forces. In a full renovation design, thousands of load cases are applied to verify the connections.

- **Formulate norms on FRP-steel bridge design and thermal loading**

The determination of the shear forces in the deck-to-girder joints revealed that thermal loading generated significant shear forces towards the edges of the deck. Since the thermal expansion coefficient of an FRP laminate is dependent on the ply lay-up, the lay-up could be tweaked to minimise shear forces in the deck-to-girder joints. The root of the problem could also be investigated by forming a recommendation on the thermal loading of FRP-steel composite bridges.

- **Practical feasibility**

The feasibility of the renovation design was mainly investigated with respect to the deck-to-girder connections. Questions related to the cost, sustainability, installation procedure and detailing of the renovation design were outside the scope of this thesis. Regarding the cost and sustainability of the renovation design, a life-cycle cost analysis (LCCA) and life-cycle assessment (LCA) could be performed, respectively. Regarding the installation procedure, it is unsure if the deck can be installed in one section. If not, it could be investigated where and how FRP deck sections should be connected to each other.

Bibliography

- [1] F. Csillag, *Demountable deck-to-girder connection of FRP- steel hybrid bridges*, Tech. Rep. September (TUDelft, 2018).
- [2] V. M. Karbhari and F. Seible, *Fiber reinforced composites - advanced materials for the renewal of civil infrastructure*, [Applied Composite Materials](#) **7**, 95 (2000).
- [3] C. C. Fu, H. Alayed, A. M. Amde, and J. Robert, *Field performance of the fiber-reinforced polymer deck of a truss bridge*, [Journal of Performance of Constructed Facilities](#) **21**, 53 (2007).
- [4] S. Brand, *How buildings learn: What Happens After They're Built* (Viking Press, 1994) p. 288.
- [5] S. Reeve, *FRP bridges - 14 years and counting*, [Reinforced Plastics](#) **54**, 40 (2010).
- [6] L. Ascione, J. Caron, P. Godonou, K. van IJselmuiden, J. Knippers, T. Mottram, M. Oppe, M. Gantriis-Sorensen, J. Taby, and L. Tromp, *Prospect for new guidance in the design of FRP*, Tech. Rep. (Joint Research Centre, Ispra, Italy, 2016).
- [7] T. Hong and M. Hastak, *Construction, Inspection, and Maintenance of FRP Deck Panels*, [Journal of Composites for Construction](#) **10**, 561 (2006).
- [8] H. Tuwair, M. Hopkins, J. Volz, M. A. ElGawady, M. Mohamed, K. Chandrashekhara, and V. Birman, *Evaluation of sandwich panels with various polyurethane foam-cores and ribs*, [Composites Part B: Engineering](#) **79**, 262 (2015).
- [9] G. Camata and B. Shing, *Evaluation of GFRP Honeycomb Beams for the O'Fallon Park Bridge*, [Journal of Composites for Construction](#) **9**, 545 (2005).
- [10] H. W. Gürtler, *Composite Action of Frp Bridge Decks Adhesively Bonded To Steel Main Girders*, [Ph.D. thesis](#), EPFL Lausanne (2004).
- [11] S. W. Lee, S. G. Lee, D. Bae, and B. S. Kim, *Flexural Characteristics of filament wound GFRP composite bridge deck*, Tech. Rep. (Kookmin University, Seoul, 2002).
- [12] M. Schollmayer, *Through-thickness performance of adhesive joints between FRP bridge decks and steel girders*, [Composite Structures](#) **87**, 232 (2009).
- [13] M. Osei-Antwi, *Structural performance of complex core systems for FRP-balsa composite sandwich bridge decks*, [Ph.D. thesis](#), EPFL Lausanne (2014).
- [14] J. F. Davalos, P. Qiao, X. Frank Xu, J. Robinson, and K. E. Barth, *Modeling and characterization of fiber-reinforced plastic honeycomb sandwich panels for highway bridge applications*, [Composite Structures](#) **52**, 441 (2001).
- [15] FiberCore, *InfraCore: technical datasheet*, Tech. Rep. (FiberCore, Rotterdam, 2007).
- [16] P. Alagusundaramoorthy, I. E. Harik, and C. C. Choo, *Structural Behavior of FRP Composite Bridge Deck Panels*, [Journal of Bridge Engineering](#) **11**, 384 (2006).
- [17] A. Zhou and T. Keller, *Joining techniques for fiber reinforced polymer composite bridge deck systems*, [Composite Structures](#) **69**, 336 (2005).
- [18] K. T. Park, S. H. Kim, Y. H. Lee, and Y. K. Hwang, *Degree of composite action verification of bolted GFRP bridge deck-to-girder connection system*, [Composite Structures](#) **72**, 393 (2006).
- [19] A. Temeles and J. J. Lesko, *Composite plate & tube bridge deck design: Evaluation in the Troutville*, *Advanced Composite Materials in Bridges and Structures*, 800 (2000).

- [20] M. Gabler and J. Knippers, *Improving structural reliability of FRP bridges by inserting fibre optic sensors*, Proceedings of Advanced Composites in Construction , 375 (2011).
- [21] M. K. Turner, K. A. Harries, M. F. Petrou, and D. Rizos, *In situ structural evaluation of a GFRP bridge deck system*, *Composite Structures* **65**, 157 (2004).
- [22] P. Cassity, D. Richards, and J. Gillespie, *Compositely acting FRP deck and girder system*, *Structural Engineering International* **12**, 71 (2002).
- [23] J. P. Moses, K. A. Harries, C. J. Earls, and W. Yulismana, *Evaluation of Effective Width and Distribution Factors for GFRP Bridge Decks Supported on Steel Girders*, *Journal of Bridge Engineering* **11**, 401 (2006).
- [24] S. Keelor, Y. Luo, and C. Earl, *Service Load Effective Compression Flange Width in Fiber Reinforced Polymer Deck Systems Acting Compositely with Steel Stringers*, *Journal of Composites for Construction* **8** (2004).
- [25] F. L. Moon, D. A. Eckel, and J. W. Gillespie, *Shear stud connections for the development of composite action between steel girders and fiber-reinforced polymer bridge decks*, *Journal of Structural Engineering* **128**, 762 (2002).
- [26] J. F. Davalos, A. Chen, and B. Zou, *Stiffness and strength evaluations of a shear connection system for FRP bridge decks to steel girders*, *Journal of Composites for Construction* **15**, 441 (2011).
- [27] J. F. Davalos, A. Chen, and B. Zou, *Performance of a scaled FRP deck-on-steel girder bridge model with partial degree of composite action*, *Engineering Structures* **40**, 51 (2012).
- [28] G. Olivier and F. Csillag, *Bolted joints for FRP decks*, Tech. Rep. (TUDelft - Arup - Rijkswaterstaat, Netherlands, 2020).
- [29] M. P. Nijgh, *New Materials for Injected Bolted Connections: A Feasibility Study for Demountable Connections*, Tech. Rep. September (TUDelft, 2017).
- [30] M. S. Pavlovic, *Resistance of Bolted Shear Connectors in prefabricated steel-concrete composite decks*, Ph.D. thesis, University of Belgrade (2013).
- [31] S. Satasivam, *Modular FRP sandwich structures for building floor construction*, Ph.D. thesis, Monash University (2015).
- [32] S. Satasivam, P. Feng, Y. Bai, and C. Caprani, *Composite actions within steel-FRP composite beam systems with novel blind bolt shear connections*, *Engineering Structures* (2017).
- [33] J. Natterer and M. Hoeft, *Zum Tragverhalten von Holz-Beton-Verbundkonstruktionen*, Forschungsbericht , 195 (1987).
- [34] Europe, *EN1995 Eurocode 5 Part 1-1: Design of timber structures*, European Standards (2008).
- [35] Rijkswaterstaat, *Vervanging & Renovatie bruggenlijst*, (2019).
- [36] Arup, *Herberekening Brug over de Beneden Merwede*, Tech. Rep. (Arup, 2020).
- [37] M. D. Klomp, *Hybrid interaction of timber decks in movable bridges*, Tech. Rep. (TUDelft, 2020).
- [38] L. Ascione, P. Godonou, K. van IJselmuiden, J. Knippers, T. Mottram, M. Oppe, M. Gantriis Sorensen, J. Taby, and L. Tromp, *Prospect for New Guidance in the Design of FRP*, Tech. Rep. (JRC European Commission, 2016).
- [39] Europe, *EN1994 Eurocode 4 Part 1-1: Design of composite steel and concrete structures*, European Standards (2004).
- [40] Europe, *BS 5400-5: Steel, concrete and composite bridges*, Tech. Rep. (British Standard, 2005).

- [41] A. Du, Y. Liu, H. Xin, and Y. Zuo, *Progressive damage analysis of PFRP double-lap bolted joints using explicit finite element method*, *Composite Structures* **152**, 860 (2016).
- [42] M. P. Nijgh, H. Xin, and M. Veljkovic, *Non-linear hybrid homogenization method for steel-reinforced resin*, *Construction and Building Materials* **182**, 324 (2018).
- [43] Europe, *EN1993 Eurocode 3 Part 1-8: Design of Joints*, European Standards (2005).
- [44] Europe, *EN1991 Eurocode 1 Part 2: Actions on structures - Traffic*, European Standards **1** (2003).
- [45] Europe, *EN1991 Eurocode 1 Part 2: Dutch National annex*, European Standards (2011).
- [46] Europe, *EN1991 Eurocode 1 Part 5: Actions on structures - Temperature*, European Standards (2003).
- [47] Europe, *EN1990 Eurocode 0: Basis of structural design*, European Standards (2006).
- [48] Rijkswaterstaat, *Archived technical drawings*, (1965).

List of Figures

1.1	Numerical analyses overview	4
2.1	Shear experiment set-up of ASSET deck (a) and in-plane shear results for the ASSET and DuraSpan deck (b) [10]	7
2.2	VARTM produced deck with triangular (a), trapezoidal (b) and rectangular (c) shapes and their longitudinal (d) and transverse (e) 3-point bending test results [11]	8
2.3	Z-shaped FRP laminates of InfraCore deck	8
2.4	Bolted fasteners: long bolt penetrating the entire deck [18] (a) including a steel sleeve [19] (b), the Ajax (c) and Lindapter (d) system [1]	11
2.5	Adhesively-bonded connection [10]	11
2.6	Shear studs: Cross-section of S655 bridge [21] (a), grouted shear connection by Moon <i>et al.</i> [25] (b), threaded shear stud by Davalos <i>et al.</i> [26] (c) and iSRR connector by Csillag [1]	12
2.7	iSRR push-out specimen [1]	13
2.8	Typical pure bolt shear failure (a) and unfastened bolts (b) of the iSRR push-out test [1]	14
2.9	Experimental force-displacement curves of the coupler [1] and embedded nuts [28] configuration	14
2.10	iSRR single-lap joint specimen [28]	14
2.11	Relative stiffness decrease under cyclic loading only (F-series) and combined cyclic+creep loading (C-series) [28]	15
2.12	Static resistance after production (S1), after cyclic loading (F1) and after creep+cyclic loading (C1) [28]	16
2.13	Theoretical full hybrid interaction of a composite beam [10]	16
2.14	Mid-span strain distribution over the composite beam height: DuraSpan VS ASSET [10]	17
2.15	Three-point bending specimen from Park <i>et al.</i> [18]	17
2.16	Three-point bending specimen from Davalos <i>et al.</i> [27]	18
2.17	Longitudinal strain distribution on the top (a) and bottom (b) facing of the FRP deck [27]	18
2.18	Specimen geometry of the FRP-steel composite beam (a) using blind bolts (b) [31]	18
2.19	Failure (a) and strain distribution along the height of the composite beam (b) [31]	19
2.20	Cross-section analysed by Gürtler [10] (a) and Satasivam <i>et al.</i> [32] (b)	20
3.1	Exploded bridge structure of the Beneden Merwede bridge	23
3.2	Timber deck to secondary girder connections	24
3.3	Cross-section of the FRP panel	25
3.4	Connection configuration with coupler (a) and embedded nuts (b) with FRP deck panel (c)	28
4.1	Connection model overview with boundary conditions	31
4.2	Meshing of the FRP panel (a), HEB260 (b), SRR (c), coupler (d) and embedded nuts connector (e)	32
4.3	Preloading of the coupler (a) and embedded nuts connector (b) by the 'turn-of-nut' method	33
4.4	Force-displacement curves of the coupler and embedded nuts FEA models compared to the single lap joint (SLJ) experimental results from Olivier and Csillag [28] and push-out tests (POT) from Csillag [1]	34
4.5	Slip of the threads	34
4.6	Damage indices of the coupler configuration at failure in the following order: SRR compression damage (a), SRR tensile damage (b), ductile damage initiation (c), FRP shear damage (d), FRP contact damage (delamination) (e)	35

4.7	Damage indices of the embedded nuts configuration at failure in the following order: SRR compression damage (a), SRR tensile damage (b), ductile damage initiation (c), FRP shear damage (d), FRP contact damage (delamination) (e)	35
4.8	Secant stiffness determined according to Eurocode 4 [39] for the FEA of the coupler push-out tests	36
5.1	Composite beam model overview with boundary conditions	41
5.2	Simplified connection overview with the geometry of the push-out tests by Csillag [1] discussed in chapter 4 (a) and the composite beam geometry (b)	43
5.3	The coupler (a) and embedded nuts connector (b) compared to the solid bolt connector with the region of uniaxial thermal strain preloading (c)	44
5.4	Force-displacement curves for connection models presented in chapter 4 and the simplified models of figures 5.2a and 5.2b	44
5.5	Cross-section of the composite beam model at mid-span	45
5.6	Pressure-displacement graph of the composite beam model and steel beam model	46
5.7	Yielding of the steel beam at 90kN/m^2 visualised with the ductile damage criterion (a) and Mises stresses $< 355\text{MPa}$ (b) (Deformations scaled 3x)	47
5.8	Tensile damage (DAMAGET) of the SRR closest to the supports at a pressure of $10\frac{\text{kN}}{\text{m}^2}$ (a), $50\frac{\text{kN}}{\text{m}^2}$ (b), $90\frac{\text{kN}}{\text{m}^2}$ (c) and $130\frac{\text{kN}}{\text{m}^2}$ (d)	48
5.9	Ductile damage (DUCTCRT) of the solid bolt closest to the supports at a pressure of $50\frac{\text{kN}}{\text{m}^2}$ (a), $90\frac{\text{kN}}{\text{m}^2}$ (b) and $130\frac{\text{kN}}{\text{m}^2}$ (c)	48
5.10	Stress-strain distribution along the height of the composite beam at mid-span	49
5.11	Stress distribution along the width of the FRP deck at mid-span	50
5.12	Cross-section of the composite beam used in the EC5 method [32]	51
5.13	Overview of the composite beam model geometry in GSA	52
5.14	Comparison of different modelling techniques at a pressure of 10kN/m^2	54
5.15	Comparison of different modelling techniques at a pressure of 50kN/m^2	55
5.16	Transverse bending and stresses diagram (not-to-scale)	57
5.17	Illustration of the secondary moment effect (not-to-scale)	58
5.18	Longitudinal stresses at mid-span illustrating the different effects	60
5.19	Compressive longitudinal stresses in the bottom facing (a), the top facing (b) and plotted (c) at a pressure level of $10\frac{\text{kN}}{\text{m}^2}$	61
5.20	Pressure-displacement graphs comparing the 600 vs 1200 mm connector spacing	62
5.21	Longitudinal connector forces at 10kN/m^2 for a spacing of 600 mm and 1200 mm	63
5.22	Tensile damage (DAMAGET) of the SRR closest to the supports at a pressure of $35\frac{\text{kN}}{\text{m}^2}$ (a), $90\frac{\text{kN}}{\text{m}^2}$ (b) and $115\frac{\text{kN}}{\text{m}^2}$ (c)	64
5.23	Ductile damage (DUCTCRT) of the solid bolt closest to the supports at a pressure of $35\frac{\text{kN}}{\text{m}^2}$ (a) $90\frac{\text{kN}}{\text{m}^2}$ (b) and $115\frac{\text{kN}}{\text{m}^2}$	64
6.1	Overview of the GSA bridge model provided by Arup	67
6.2	Local model to weak axis bending stiffness [36]	68
6.3	Section of global bridge model including the FRP deck	68
6.4	Distribution of the iSRR connectors	69
6.5	Traffic load model 1 imposed on the Beneden Merwede bridge	70
6.6	Longitudinal positioning of the tandem systems	70
6.7	Application of heaviest FLM4b truck with seven axles	70
6.8	Definition of fatigue load model 4b [45]	71
6.9	Temperature difference component for the thermal expansion load case [46]	71
6.10	Section forces/moments in the eastern main-girder	73
6.11	Effect of weak axis bending on transverse force in deck-to-girder joint (top-view cross-to main-girder connection)	74
6.12	Deck-to-girder connection force-states longitudinally F_x (a) and transversely F_y (b)	74
6.13	Deck-to-girder connection force-states longitudinally F_x (a) and transversely F_y (b)	75
6.14	Deck-to-girder connection force-states longitudinally F_x (a) and transversely F_y (b)	77

6.15 Connection force-states longitudinally F_x with LM1 tandem at position 2 (a) and transversely F_y with LM1 tandem at position 1 (b)	78
6.16 Deck-to-girder connection force-states longitudinally F_x (a) and transversely F_y (b)	79
6.17 Deck-to-girder connection force-states longitudinally F_x (a) and transversely F_y (b)	81
6.18 Distribution of the iSRR connectors when connecting the main-girder	82
6.19 Deck-to-girder connection force-states longitudinally F_x (a) and transversely F_y (b)	83
6.20 Longitudinal force distribution near the connection of cross-girder 2 with the eastern main-girder	84
6.21 Deck-to-girder connection force-states longitudinally F_x (a) and transversely F_y (b)	85
6.22 Weak-axis bending of the cross- to main-girder connection	87
6.23 Displacement and moment comparison of the eastern main-girder under traffic LM1 loading with the tandem system located at position 1	88
A.1 Overview of the Beneden Merwede Bridge [48]	102
A.2 Cross-section of the Beneden Merwede Bridge before the widening in the 70's [48]	103
A.3 Cross-section of the Beneden Merwede Bridge after the widening in the 70's [48]	103
B.1 Stress-strain relationship for various metals [1]	105
B.2 Compression (a) and tension (b) stress-strain curves of the SRR [1]	105
B.3 Stress-strain relationship of PUR foams [8]	106
B.4 Damage indices of the coupler configuration right before slipping (0.4mm): SRR compression damage (a), SRR tensile damage (b), ductile damage initiation (c)	107
B.5 Damage indices of the embedded nuts configuration right before slipping (0.4mm): SRR compression damage (a), SRR tensile damage (b), ductile damage initiation (c)	107
B.6 Damage indices of the coupler configuration after slipping (1.8mm): SRR compression damage (a), SRR tensile damage (b), ductile damage initiation (c)	108
B.7 Damage indices of the embedded nuts configuration after slipping (1.8mm): SRR compression damage (a), SRR tensile damage (b), ductile damage initiation (c)	108
C.1 Overview of the composite beam model including the foam core	111
C.2 Pressure-displacement curves of the composite beam model including VS excluding foam core	111
C.3 Force-displacement curves for the elementary modelling simplifications of the coupler POT	112
C.4 Mesh and boundary condition of steel girder model	113
C.5 Boundary conditions of composite beam model with the fixed beam	120
C.6 Transverse (a) and longitudinal (b) stresses in the top facing	120
C.7 Transverse (a) and longitudinal (b) stresses in the bottom facing	121
C.8 Loading of composite beam model with the line load	121
C.9 Longitudinal stresses in the top facing	122
C.10 Longitudinal stresses in the bottom facing	122
C.11 Yielding of the steel beam at $90kN/m^2$ visualised with the ductile damage criterion (a) and Mises stresses $< 355MPa$ (b) (Deformations scaled 3x)	122
D.1 Weight of the steel superstructure visualised	123
D.2 Weight of the counterweight	123
D.3 Calculation of the weight of the FRP deck	124
D.4 Calculation of the weight of the timber deck including the secondary girders	124

List of Tables

2.1	Examples of different FRP panel configurations	9
3.1	Movable highway bridges in the Netherlands with a timber deck (Haringvliet was recently retrofitted with an aluminium deck)	22
3.2	Geometrical parameter values of figure 3.3	26
3.3	Stiffness values for facing and web laminates ($V_f = 50\%$)	26
4.1	Secant stiffness corresponding to figure 4.8	37
4.2	Distinctive values in force-displacement curves	37
5.1	Geometry parameters	41
5.2	Distinctive values in force-displacement curves for connection simplification steps	45
5.3	Bending stiffness EI_m comparison at $q = 10kN/m^2$	46
5.4	Displacements at $q = 10kN/m^2$	51
5.5	Analytical versus finite element stresses in the FRP panel	58
5.6	Analytical versus finite element longitudinal stresses in the FRP panel at mid-span	59
6.1	Cross- to main-girder connection properties	68
6.2	Combinations	72
6.3	Maximum connector forces from the load combinations expressed in table 6.2	76
6.4	Maximum longitudinal F_x and transverse F_y connection forces	77
6.5	Maximum connector forces from the load combinations expressed in table 6.2	80
6.6	Maximum longitudinal F_x and transverse F_y connection forces	83
6.7	Maximum longitudinal F_x and transverse F_y connection forces	85
6.8	Comparison strong axis bending moments	86
6.9	Comparison weak axis bending moments	87
B.1	FRP laminate layup (sublaminates interfaces in red)	104
B.2	Elastic FRP material properties	104
B.3	Nonlinear FRP material parameters	104
B.4	Cohesive surface properties	104
B.5	Elastic and CDP material parameters for the SRR	105

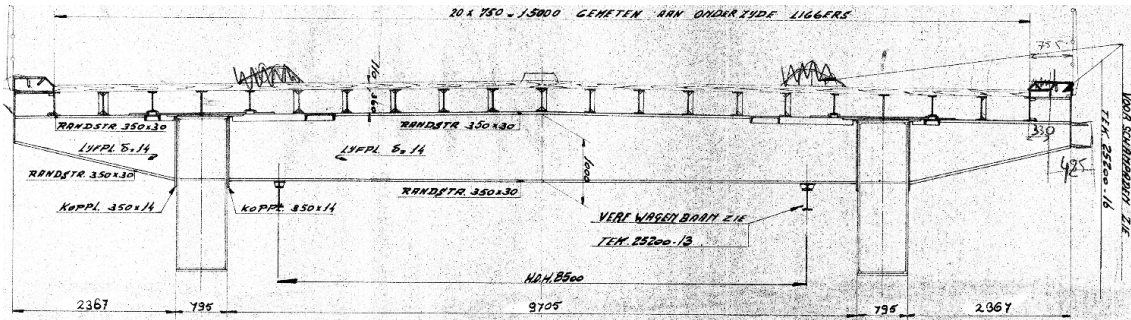


Figure A.2: Cross-section of the Beneden Merwede Bridge before the widening in the 70's [48]

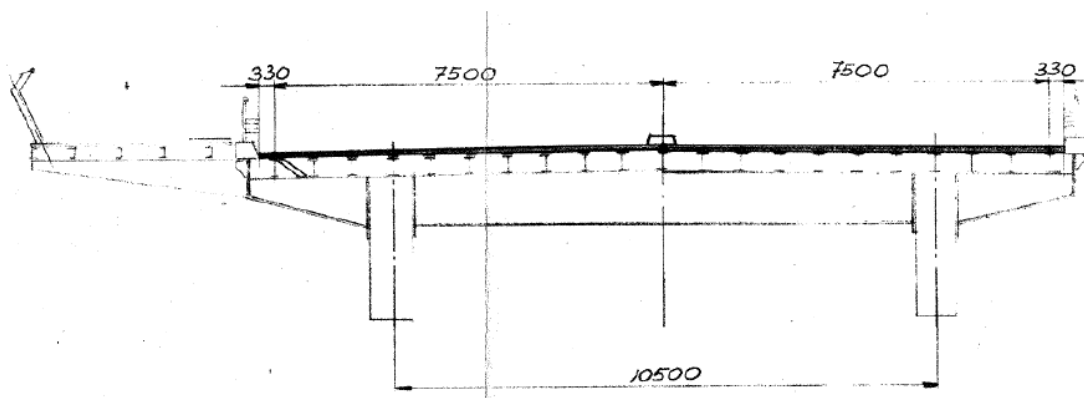


Figure A.3: Cross-section of the Beneden Merwede Bridge after the widening in the 70's [48]

B

Connection model

B.1. Material models

FRP laminate properties [1]

Table B.1: FRP laminate layup (sublaminates interfaces in red)

Facings	[0 ₄ /45/-45/0/90/0 ₄ /45/-45/0/90/0 ₄ /45/-45/0/90/0 ₄ /45/-45/0/90/0 ₄ /45/-45/0/90/45/-45]
Webs	[45/-45/45/-45/0/90/45/-45/45/-45]

Table B.2: Elastic FRP material properties

Material	Elastic constants [GPa]	Poison ratio's	Density [kg/m ³]
Elastic FRP UD ply - facing	$E_1 = 31.450, E_2 = E_3 = 8.459,$ $G_{12} = G_{13} = 4.838, G_{23} = 3.021$	$\nu_{12} = \nu_{13} = 0.272,$ $\nu_{23} = 0.4$	1873
Elastic FRP UD ply - webs	$E_1 = 21.17, E_2 = E_3 = 5.69,$ $G_{12} = G_{13} = 3.26, G_{23} = 2.032$	$\nu_{12} = \nu_{13} = 0.308,$ $\nu_{23} = 0.4$	1539

Table B.3: Nonlinear FRP material parameters

Property	Longitudinal tensile	Longitudinal compression	Transverse tensile	Transverse compression	Longitudinal shear	Transverse shear
Strength [MPa]	865	700	36	131	87	75
Fracture energy	92	80	0.2774	0.7979	-	-

Table B.4: Cohesive surface properties

Property	Normal - mode I	Shear - mode II and III
Contact strength [MPa]	21	30
Fracture energy [N/mm]	0.9	4.0

Steel material properties

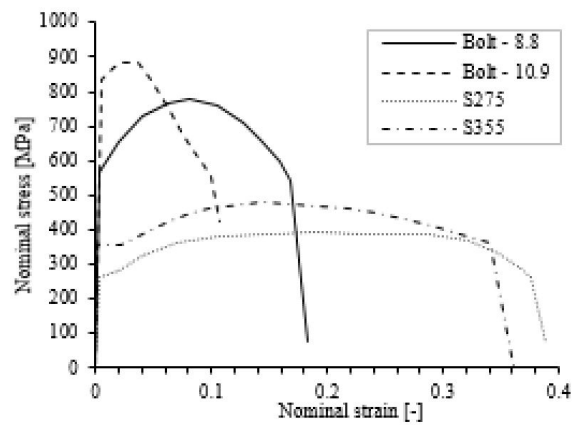


Figure B.1: Stress-strain relationship for various metals [1]

SRR material properties

Table B.5: Elastic and CDP material parameters for the SRR

Property		Unit	Value
Compression strength	f_c	[MPa]	74.3
Tensile strength	f_t	[MPa]	10.1
Young's modulus	E	[GPa]	9.3
Poisson ratio	ν	-	0.3
Eccentricity	ϵ	-	0.1
Ratio of biaxial/uniaxial strength	σ_{bo}/σ_{co}	-	1.2
Dilation angle	ψ	[°]	50.535
Second stress invariant parameter	K_c	-	0.78
Viscosity parameter	μ	-	0

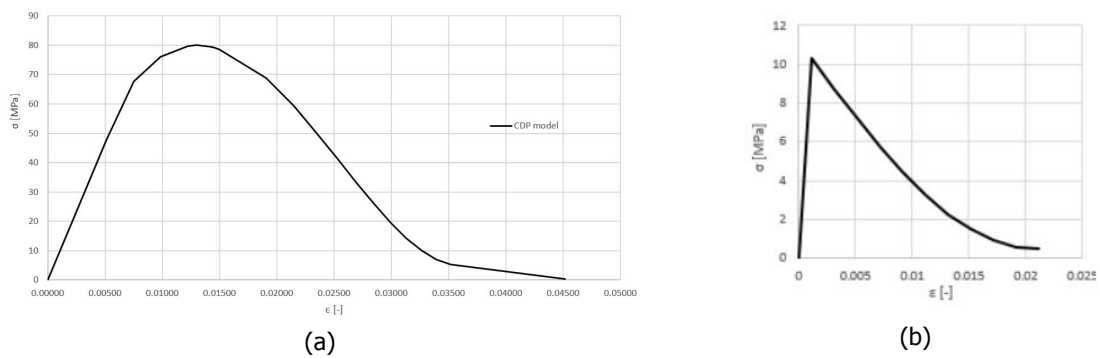


Figure B.2: Compression (a) and tension (b) stress-strain curves of the SRR [1]

Foam material properties

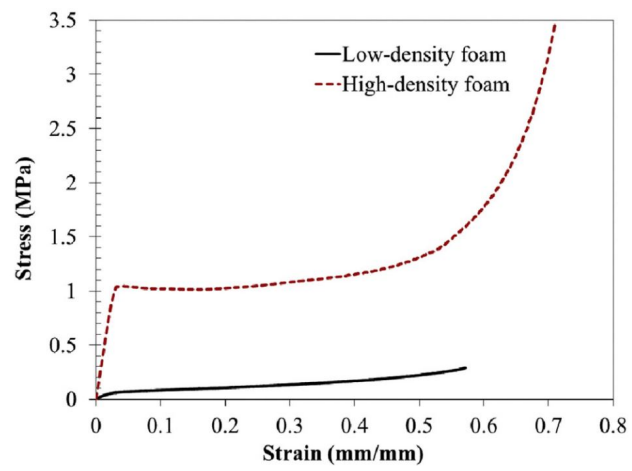


Figure B.3: Stress-strain relationship of PUR foams [8]

B.2. Results

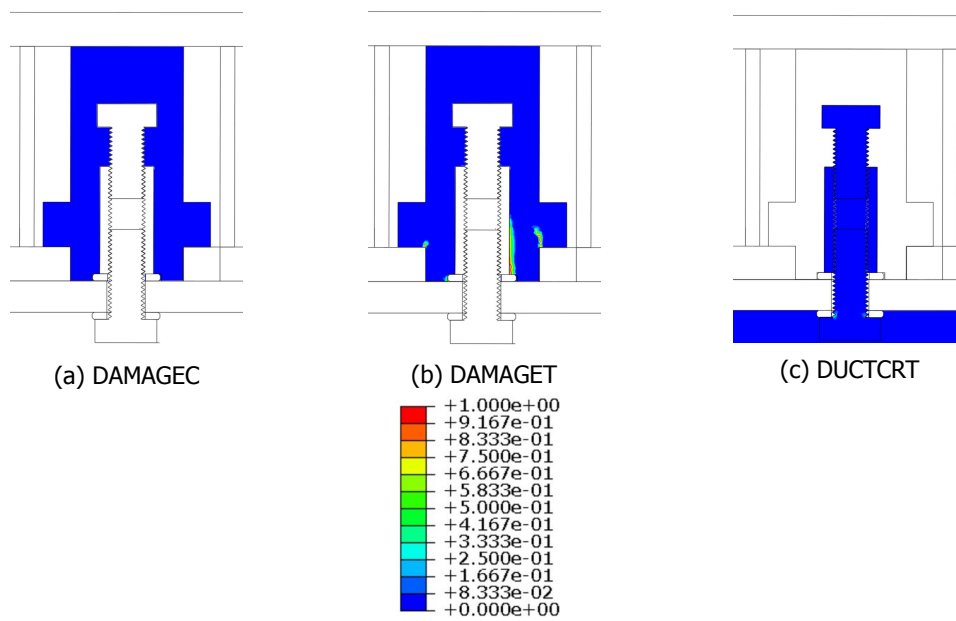


Figure B.4: Damage indices of the coupler configuration right before slipping (0.4mm): SRR compression damage (a), SRR tensile damage (b), ductile damage initiation (c)

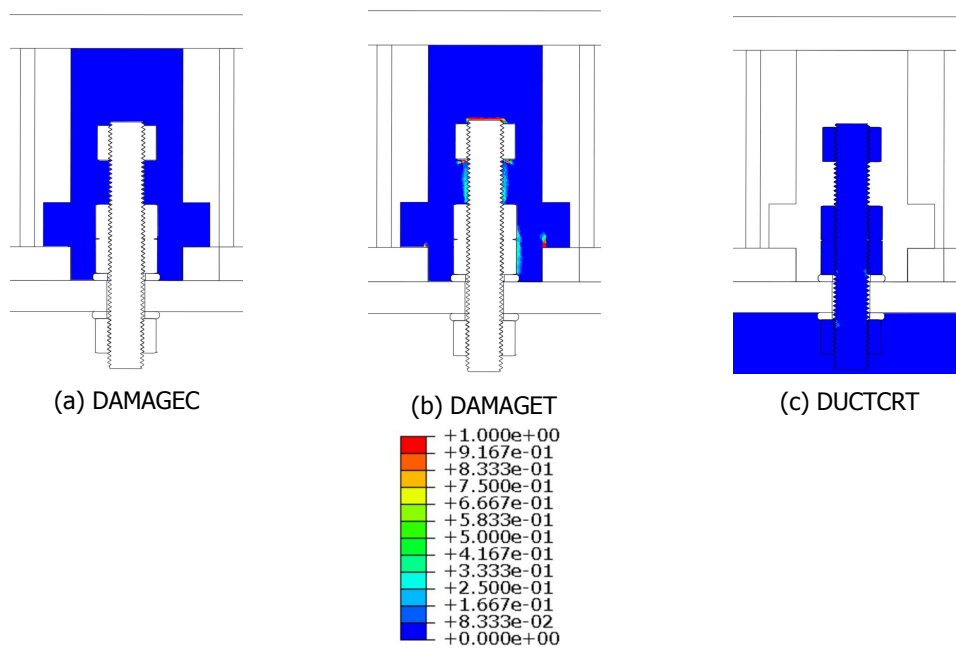


Figure B.5: Damage indices of the embedded nuts configuration right before slipping (0.4mm): SRR compression damage (a), SRR tensile damage (b), ductile damage initiation (c)

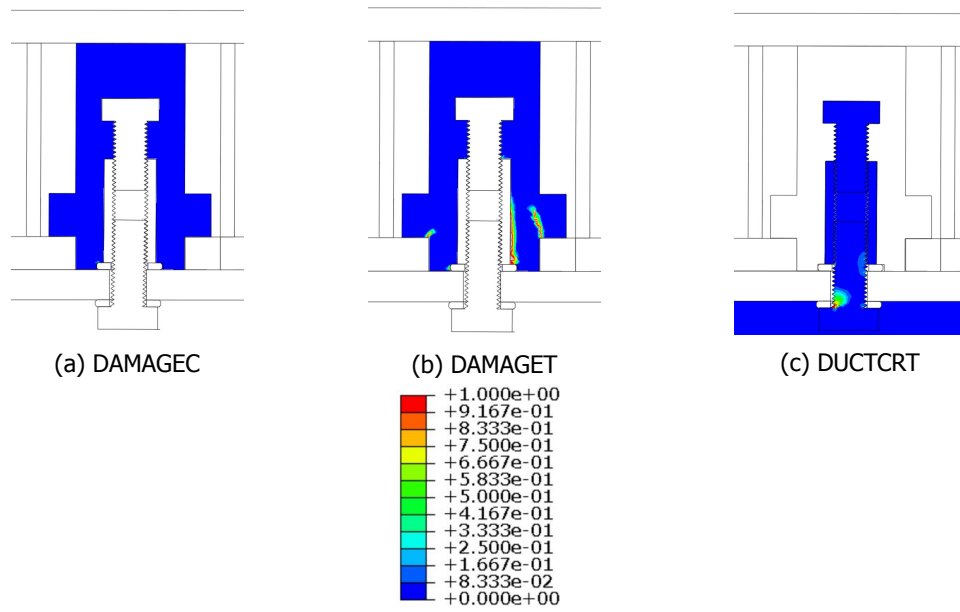


Figure B.6: Damage indices of the coupler configuration after slipping (1.8mm): SRR compression damage (a), SRR tensile damage (b), ductile damage initiation (c)

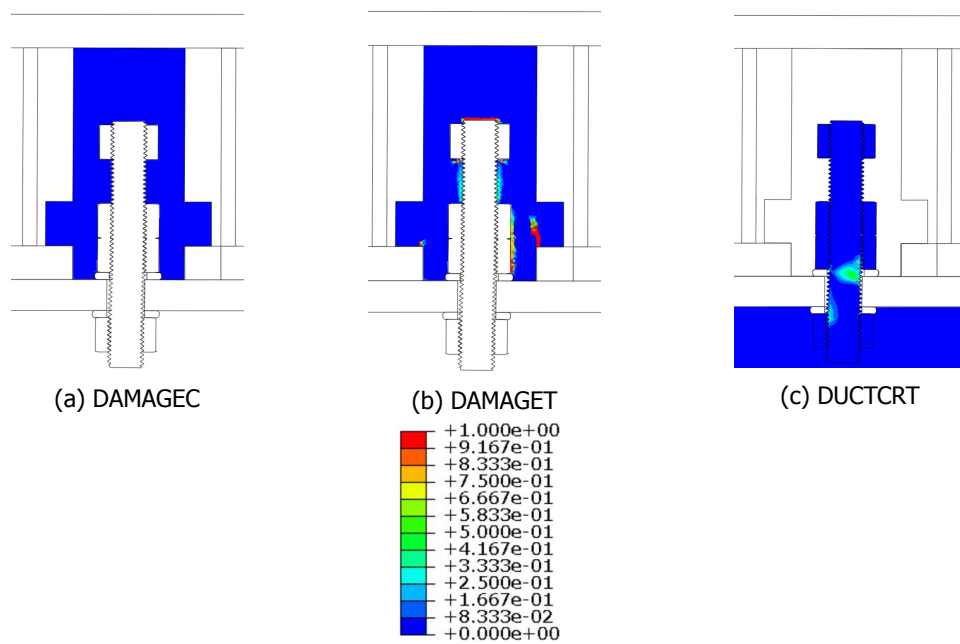


Figure B.7: Damage indices of the embedded nuts configuration after slipping (1.8mm): SRR compression damage (a), SRR tensile damage (b), ductile damage initiation (c)

B.3. Verification connection model

Verification connection model

1. Static resistance of iSRR connection

1.1 Input data

Bolt:

bolt diameter: $\phi_{b,iSRR} := 20\text{mm}$
 bolt material: $f_{ub} := 1000\text{MPa}$
 tensile area: $A_{s,M20} := 245\text{mm}^2$

Steel plate:

ultimate strength S355: $f_u := 490\text{MPa}$
 steel plate thickness : $t_{sp} := 20\text{mm}$
 hole in steel: $d_{0,s} := 21\text{mm}$

FRP panel:

thickness facing: $t := 19\text{mm}$
 hole in FRP: $d_{0,iSRR} := 60\text{mm}$

Material properties of FRP:

Elastic constants of the JRC laminate $[0^\circ/55\%, 90^\circ/15\%, 45^\circ/15\%, -45^\circ/15\%]$:

$$E_{1,f} := 25.8\text{GPa} \quad E_{2,f} := 15.9\text{GPa} \quad G_{12,f} := 5.6\text{GPa} \quad \nu_{12,f} := 0.32$$

Strength according to CUR:

$$\sigma_1 := E_{1,f} \cdot 1.2\% = 309.6\text{MPa} \quad \sigma_2 := E_{2,f} \cdot 1.2\% = 190.8\text{MPa} \quad \tau_{12,f} := G_{12,f} \cdot 1.6\% = 89.6\text{MPa}$$

1.2 Expected failure modes

Pin-bearing failure of the FRP panel

$$k_{cc} := 1$$

$$F_{b,R} := \frac{1}{k_{cc}} \sigma_2 \cdot d_{0,iSRR} \cdot t = 217.512\text{ kN}$$

Pin-bearing failure of HEB260 flange

edge and pitch distance: $e_1 := 140\text{mm}$ $e_2 := 70\text{mm}$ $p_2 := 150\text{mm}$

$$k_1 := \min\left(2.8 \cdot \frac{e_2}{d_{0,s}} - 1.7, 2.5\right) = 2.5$$

$$\alpha_b := \min\left(\frac{e_1}{3 \cdot d_{0,s}}, \frac{f_{ub}}{f_u}, 1.0\right) = 1$$

$$F_{b,pb} := k_1 \cdot \alpha_b \cdot f_u \cdot \phi_{b,iSRR} \cdot t_{sp} = 490\text{ kN}$$

Bolt shear failure

$$\alpha_v := 0.5 \quad \text{- for steel grades 10.9 or higher} \quad \gamma_{M2} := 1.25$$

$$F_{v,Rk} := \alpha_v \cdot f_{ub} \cdot A_{s,M20} = 122.5\text{ kN}$$

$$F_{v,Rd} := \frac{F_{v,Rk}}{\gamma_{M2}} = 98\text{ kN}$$

$$\alpha_v := 0.6 \quad \text{- matched better with test results Olivier & Csillag (2020)}$$

$$F_{v,Rk} := \alpha_v \cdot f_{ub} \cdot A_{s,M20} = 147\text{ kN}$$

$$F_{v,Rd} := \frac{F_{v,Rk}}{\gamma_{M2}} = 117.6\text{ kN}$$

Slip-resistance

$k_s := 1$ - Bolts in either oversized holes or short slotted holes with the axis of the slot perpendicular to the direction of load transfer

$n := 1$ $\mu := 0.35$

$$F_{p,C} := 0.7 \cdot f_{ub} \cdot A_{s,M20} = 171.5 \cdot \text{kN}$$

$$F_{s,Rk} := k_s \cdot n \cdot \mu \cdot F_{p,C} = 60.025 \cdot \text{kN}$$

In serviceability limit state: $\gamma_{M3,ser} := 1.1$

$$F_{s,Rd} := \frac{F_{s,Rk}}{\gamma_{M3,ser}} = 54.568 \cdot \text{kN}$$

1.3. Summary of results

Maximum static resistance of the push-out test with iSRR connectors:

$$V_{R,iSSR} := \min(F_{b,R}, F_{v,Rk}, F_{b,pb}) = 147 \cdot \text{kN} \quad \text{Bolt-shear failure is governing}$$

Design strength: $F_{v,Rd} = 117.6 \cdot \text{kN}$

Slipping of the bolt in the steel hole: $F_{s,Rk} = 60.025 \cdot \text{kN}$

Design slip resistance: $F_{s,Rd} = 54.568 \cdot \text{kN}$

C

Composite beam model

C.1. Influence of foam core

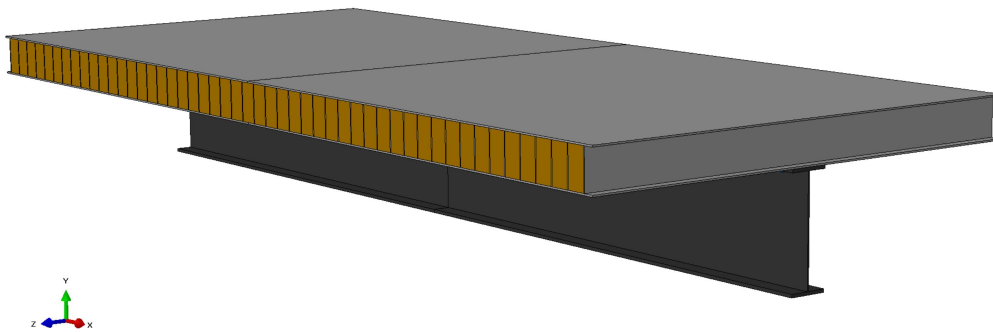


Figure C.1: Overview of the composite beam model including the foam core

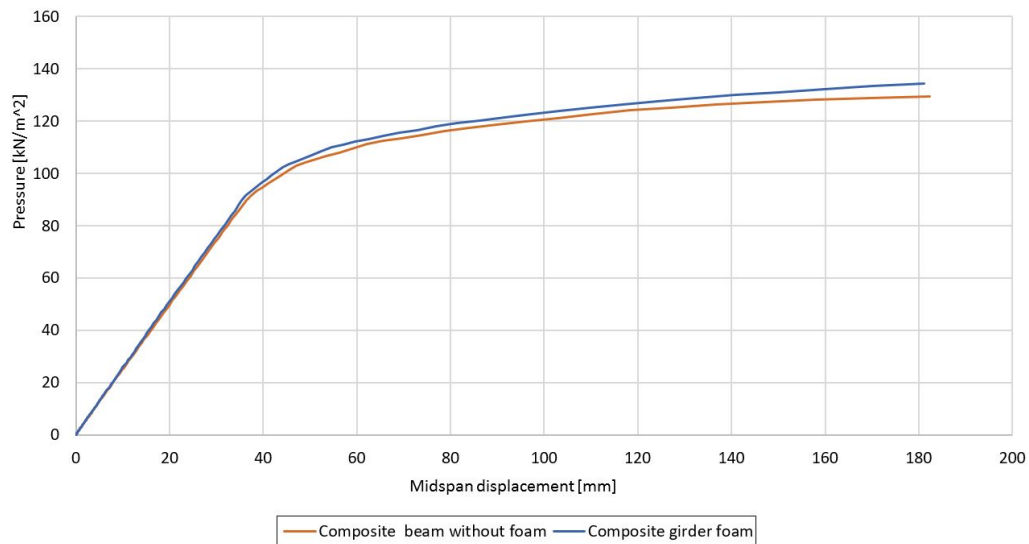


Figure C.2: Pressure-displacement curves of the composite beam model including VS excluding foam core

C.2. Connection simplification

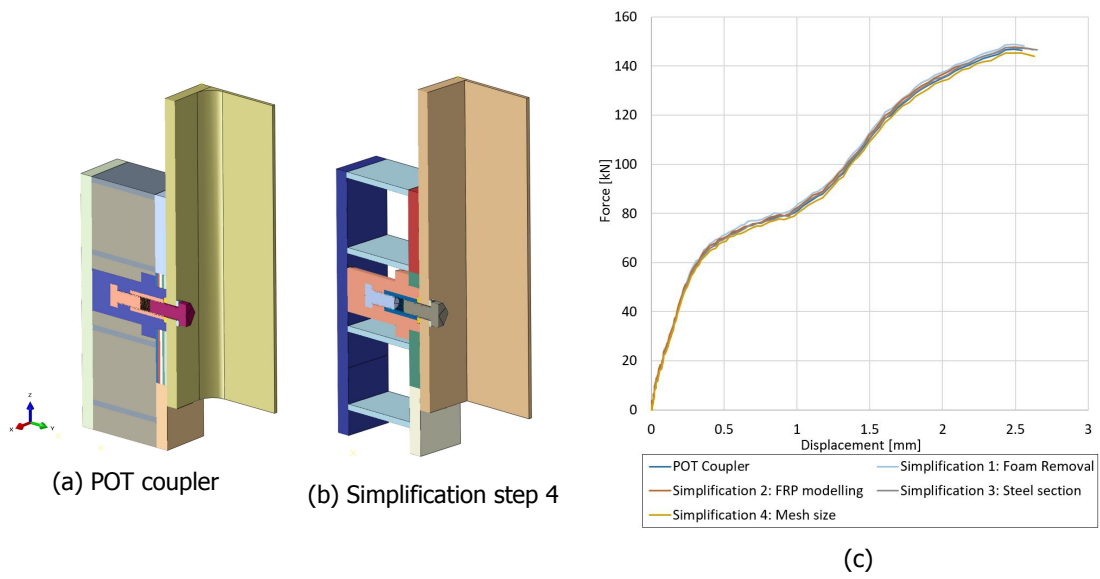


Figure C.3: Force-displacement curves for the elementary modelling simplifications of the coupler POT

C.3. Steel beam model

In order to compare the stiffness from the composite beam model to a ordinary steel beam, a steel beam model is made with identical properties and dimensions as the steel beam of the composite beam model, i.e. the Beneden Merwede bridge cross-girder. The only difference is the addition of a boundary condition to provide out-of-plane stability of the beam. In case of the composite beam, the FRP deck provides lateral stability to the top flange of the steel beam. Therefore, a lateral restraint is added to the top flange of the steel beam as can be seen in figure C.4.

The top flange of the steel beam is loaded with a uniformly distributed pressure that is applied using the smooth step function over a time period of 800s and a target time increment of 0.01s. The reaction forces and mid-span are measured and used to create the pressure-displacement curves. The equivalent pressure compared to the composite beam model is calculated using the following formula:

$$q = \frac{RF1 + RF2}{L_{beam}b_{deck}}$$

where RF1 and RF2 are the vertical reaction forces at the end of the beam, $L_{beam} = 10m$ is the length of the beam and $b_{deck} = 4.4m$ is the original width of the composite beam model.

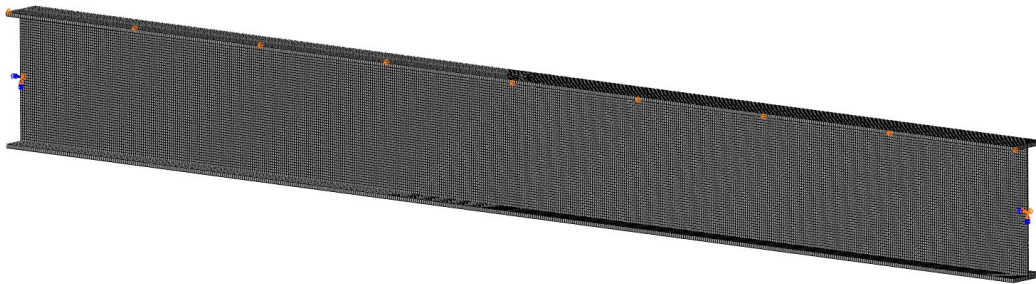


Figure C.4: Mesh and boundary condition of steel girder model

C.4. Verification composite beam model

Analytical verification composite girder

FRP material properties

Flanges - Anisotropic FRP laminate

$$E_{1,f} := 25.8\text{GPa} \quad E_{2,f} := 15.9\text{GPa} \quad G_{12,f} := 5.6\text{GPa} \quad \nu_{12,f} := 0.32$$

The application of the 1.2 % strain limit and 1.6 % shear strain limit results in the following typical strengths for these laminates as shown below.

$$\sigma_{1t,f} := 310\text{MPa} \quad \sigma_{2t,f} := 191\text{MPa} \quad \tau_{12,f} := 90\text{MPa}$$

$$\sigma_{1c,f} := 310\text{MPa} \quad \sigma_{c2,f} := 191\text{MPa} \quad \tau_{\text{ILSS},f} := 20\text{MPa}$$

Web - Quasi-isotropic FRP laminate

$$E_{1,w} := 18.6\text{GPa} \quad E_{2,w} := 18.6\text{GPa} \quad G_{12,w} := 7\text{GPa} \quad \nu_{12,w} := 0.33$$

The application of the 1.2 % strain limit and 1.6 % shear strain limit results in the following typical strengths for these laminates as shown below.

$$\sigma_{1t,w} := 223\text{MPa} \quad \sigma_{2t,w} := 223\text{MPa} \quad \tau_{12,w} := 112\text{MPa}$$

$$\sigma_{1c,w} := 223\text{MPa} \quad \sigma_{c2,w} := 223\text{MPa} \quad \tau_{\text{ILSS},w} := 20\text{MPa}$$

FRP Geometry

$L_{sp} := 4400\text{mm}$	- length of the panel
$t_f := 20\text{mm}$	- thickness of the facing
$h_c := 360\text{mm}$	- web/core height
$h_d := 2 \cdot t_f + h_c = 400\text{mm}$	- height of sandwich panel
$t_w := 10\text{mm}$	- web thickness
$s_w := 120\text{mm}$	- spacing of the webs

Steel material properties

$$f_y := 355 \text{MPa}$$

$$E_a := 210 \text{GPa}$$

Steel beam properties

$$b_{f,a} := 350 \text{mm}$$

$$t_{f,a} := 30 \text{mm}$$

$$h_{w,a} := 1000 \text{mm}$$

$$t_{w,a} := 14 \text{mm}$$

Section area:

$$A_a := 2 \cdot t_{f,a} \cdot b_{f,a} + t_{w,a} \cdot h_{w,a} = 0.035 \text{m}^2$$

Section moment of inertia:

$$I_a := \frac{1}{12} \cdot b_{f,a} \cdot (h_{w,a} + 2 \cdot t_{f,a})^3 - \frac{1}{12} \cdot (b_{f,a} - t_{w,a}) \cdot h_{w,a}^3 = 6.738 \times 10^9 \cdot \text{mm}^4$$

Effective bending stiffness according to EC5

$$L_{\text{beam}} := 10000\text{mm}$$

1. Top facing - Region 1

$$b_1 := L_{\text{sp}} = 4.4\text{m}$$

$$h_1 := t_f$$

Eurocode 4 part 1 concrete-steel girders is used to get an initial approximation of the effective width:

$$b_0 := 200\text{mm} \quad \text{- distance between outstand shear connectors}$$

$$b_{ei} := \frac{L_{\text{beam}}}{8} \quad \text{- effective width of the FRP flange on each side of the web}$$

$$b_{1,\text{eff}} := b_0 + 2 \cdot b_{ei} = 2.7 \times 10^3 \text{mm}$$

$$E_1 := E_{2,f} = 15.9 \cdot \text{GPa}$$

$$A_1 := b_{1,\text{eff}} \cdot h_1 = 0.054 \text{m}^2$$

$$I_1 := \frac{b_{1,\text{eff}} \cdot h_1^3}{12} = 1.8 \times 10^6 \cdot \text{mm}^4$$

In-plane shear stiffness of the FRP deck is taken from Gürtler (2004) as the shear stiffness of a DuraSpan deck

$$G_{\text{xz.DuraSpan}} := 3.3\text{MPa}$$

$$k_1 := G_{\text{xz.DuraSpan}} \cdot \frac{1}{h_d} = 8.25 \times 10^{-3} \cdot \frac{\text{N}}{\text{mm}^3}$$

$$K_1 := b_{1,\text{eff}} \cdot k_1$$

$$\gamma_1 := \frac{1}{1 + \frac{\pi^2 \cdot E_1 \cdot A_1}{K_1 \cdot L_{\text{beam}}^2}} = 0.208$$

2. Bottom facing - Region 2

$$b_2 := L_{sp} = 4.4 \text{ m}$$

$$b_{2,eff} := b_{1,eff} = 2.7 \text{ m}$$

$$h_2 := t_f = 20 \text{ mm}$$

$$E_2 := E_{2,f} = 15.9 \cdot \text{GPa}$$

$$A_2 := b_{2,eff} \cdot h_2 = 5.4 \times 10^4 \cdot \text{mm}^2$$

$$I_2 := \frac{b_{2,eff} \cdot h_2^3}{12} = 1.8 \times 10^6 \cdot \text{mm}^4$$

$$\gamma_2 := 1$$

3. Steel section - Region 3

$$h_3 := h_{w,a} + 2 \cdot t_{f,a} = 1.06 \times 10^3 \cdot \text{mm}$$

$$E_3 := E_a = 210 \cdot \text{GPa}$$

$$A_3 := A_a = 0.035 \text{ m}^2$$

$$I_3 := I_a = 6.738 \times 10^9 \cdot \text{mm}^4$$

$$k_3 := 212 \frac{\text{kN}}{\text{mm}} \quad \text{- initial connection stiffness}$$

$$K_3 := 2 \cdot k_3 = 424 \cdot \frac{\text{kN}}{\text{mm}} \quad \text{- 2 bolts per row}$$

$$c_w := 600 \text{ mm} \quad \text{- stud spacing}$$

$$\gamma_3 := \frac{1}{1 + \frac{\pi^2 \cdot E_3 \cdot A_3 \cdot c_w^2}{K_3 \cdot L_{beam}^2}} = 0.493$$

Distance from the region's geometrical centroid to its neutral axis:

$$a_2 := \frac{\gamma_1 \cdot E_1 \cdot A_1 \cdot (h_1 + h_2) - \gamma_3 \cdot E_3 \cdot A_3 \cdot (h_2 + h_3)}{2 \cdot (\gamma_1 \cdot E_1 \cdot A_1 + \gamma_2 \cdot E_2 \cdot A_2 + \gamma_3 \cdot E_3 \cdot A_3)} = -0.419 \text{ m}$$

$$a_1 := -\left(h_d - \frac{h_1}{2} - \frac{h_2}{2} - a_2 \right) = -0.799 \text{ m}$$

$$a_3 := \frac{h_2}{2} + \frac{h_3}{2} + a_2 = 0.121 \text{ m}$$

Effective bending stiffness:

$$EI_{\text{eff}} := \left(E_1 \cdot I_1 + \gamma_1 \cdot E_1 \cdot A_1 \cdot a_1^2 \right) + \left(E_2 \cdot I_2 + \gamma_2 \cdot E_2 \cdot A_2 \cdot a_2^2 \right) + \left(E_3 \cdot I_3 + \gamma_3 \cdot E_3 \cdot A_3 \cdot a_3^2 \right)$$

$$EI_{\text{eff}} = 1.733 \times 10^{15} \cdot \text{N} \cdot \text{mm}^2$$

Steel beam bending stiffness:

$$E_a \cdot I_a = 1.415 \times 10^{15} \cdot \text{N} \cdot \text{mm}^2$$

Displacements

$$q := 10 \frac{\text{kN}}{\text{m}^2}$$

Analytically

$$G_a := \frac{E_a}{2 \cdot (1 + 0.3)} = 8.077 \times 10^4 \cdot \text{MPa} \quad A_{a,w} := t_{w,a} \cdot h_{w,a} = 0.014 \text{ m}^2 \quad k_a := \frac{A_{a,w}}{A_a} = 0.4$$

$$w := \frac{5}{384} \cdot \frac{q \cdot b_1 \cdot L_{\text{beam}}^4}{EI_{\text{eff}}} + \frac{1}{8} \cdot \frac{q \cdot b_1 \cdot L_{\text{beam}}^2}{k_a \cdot G_a \cdot A_a} = 3.792 \cdot \text{mm}$$

Abaqus FEA

$$w_{\text{Abaqus.FEA}} := 3.9294 \text{ mm} \quad \text{Error}_{\text{Abaqus}} := 100 \left(1 - \frac{w}{w_{\text{Abaqus.FEA}}} \right) = 3.488$$

Steel beam only - including shear deformation

$$w_a := \frac{5}{384} \cdot \frac{q \cdot b_1 \cdot L_{\text{beam}}^4}{E_a \cdot I_a} + \frac{1}{8} \cdot \frac{q \cdot b_1 \cdot L_{\text{beam}}^2}{k_a \cdot G_a \cdot A_a} = 4.535 \cdot \text{mm}$$

$$\text{Improvement} := 100 \left(1 - \frac{w}{w_a} \right) = 16.382$$

Moment resistance

Yielding moment resistance - Steel beam only

$$q_y := \frac{f_y \cdot I_a \cdot 8}{\frac{(h_{w,a} + 2t_{f,a})}{2} \cdot L_{\text{beam}}^2 \cdot b_1} = 82.058 \cdot \frac{\text{kN}}{\text{m}^2}$$

C.5. Transverse bending effect

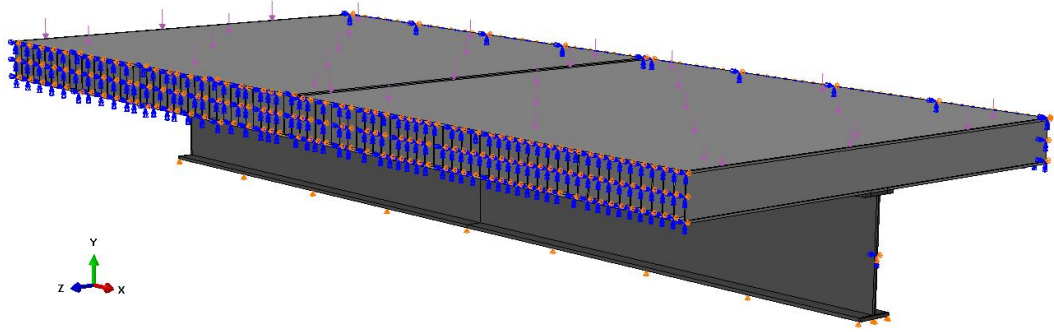


Figure C.5: Boundary conditions of composite beam model with the fixed beam

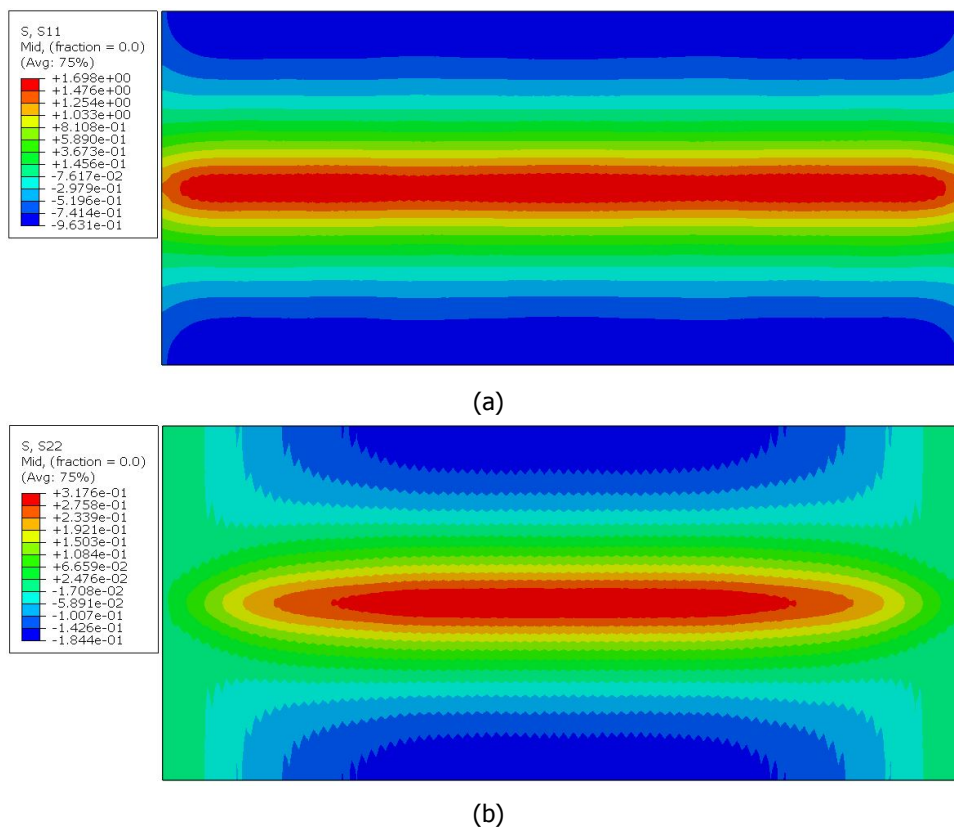


Figure C.6: Transverse (a) and longitudinal (b) stresses in the top facing

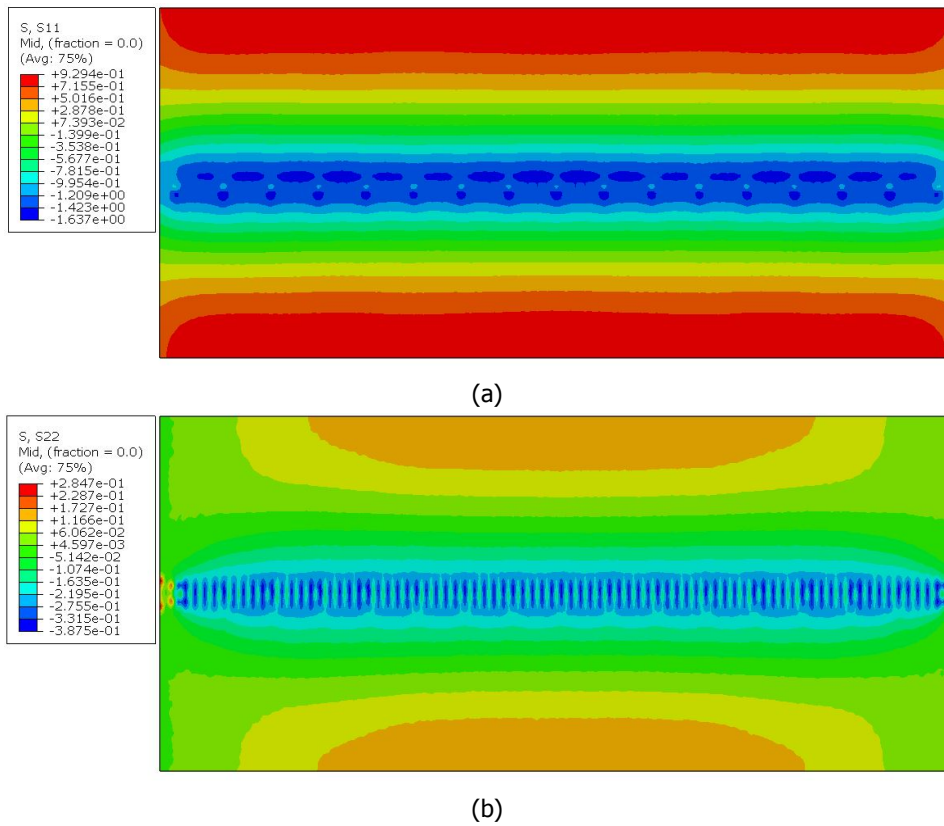


Figure C.7: Transverse (a) and longitudinal (b) stresses in the bottom facing

C.6. Secondary moment effect

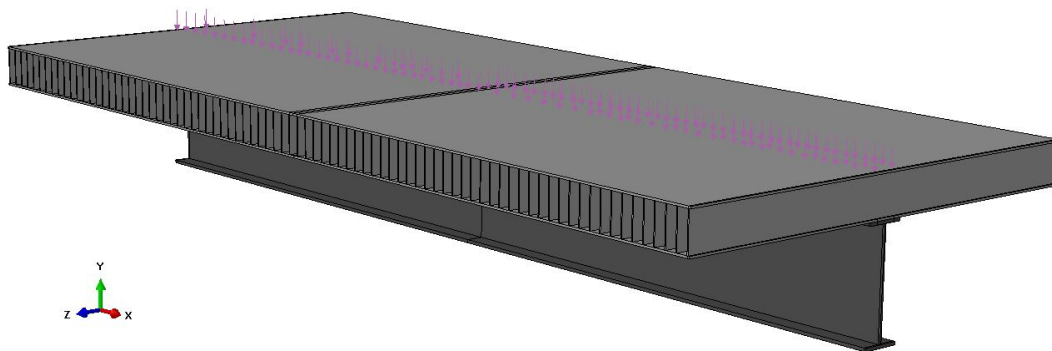


Figure C.8: Loading of composite beam model with the line load

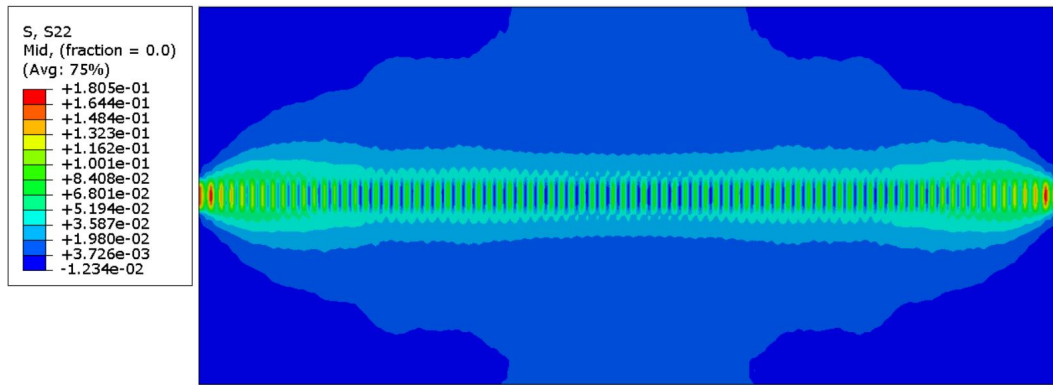


Figure C.9: Longitudinal stresses in the top facing

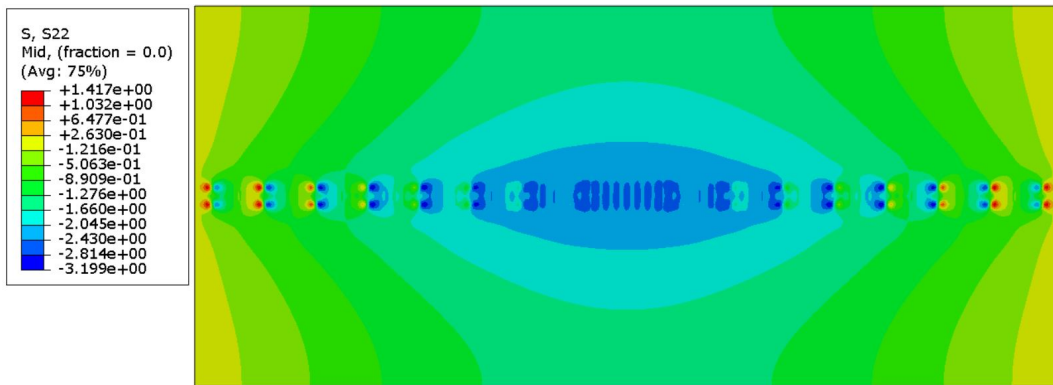
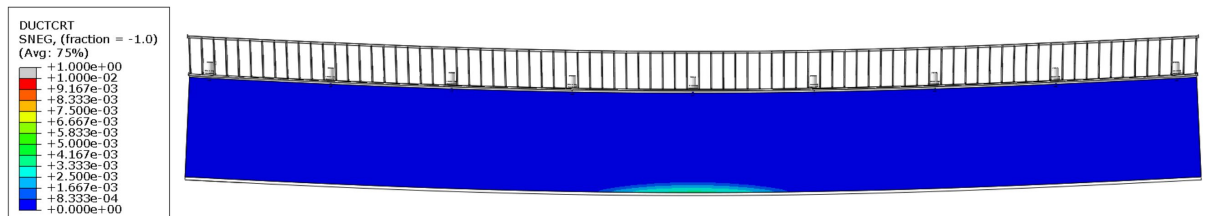
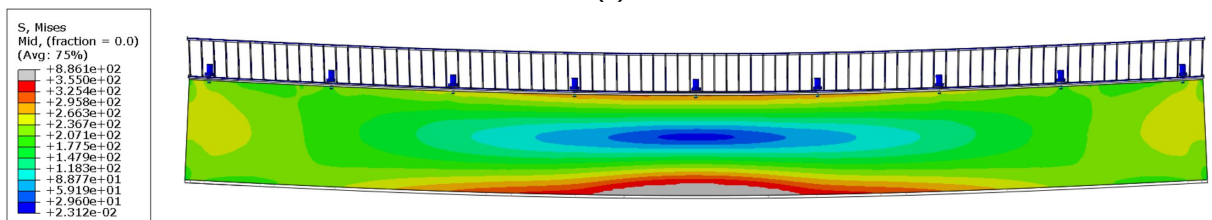


Figure C.10: Longitudinal stresses in the bottom facing

C.7. Connector spacing $c_w = 1200mm$



(a)



(b)

Figure C.11: Yielding of the steel beam at $90kN/m^2$ visualised with the ductile damage criterion (a) and Mises stresses $< 355MPa$ (b) (Deformations scaled 3x)

D

Bridge model

D.1. Permanent loads

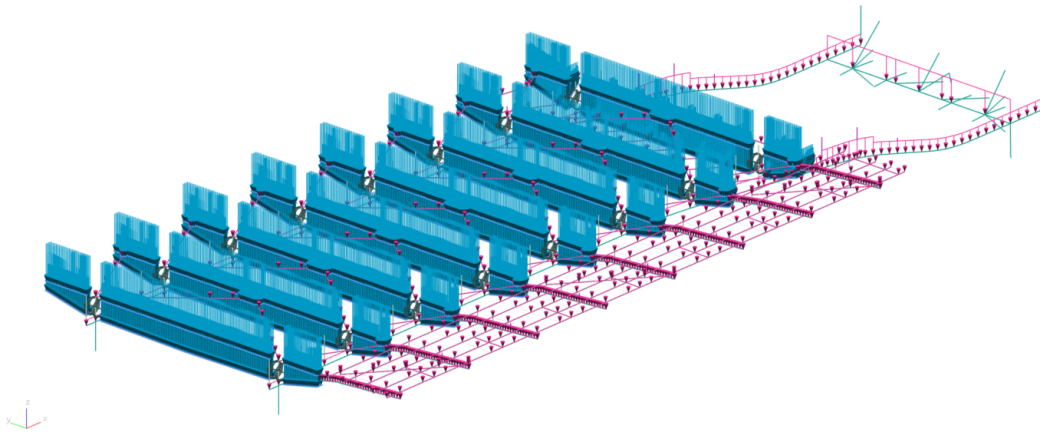


Figure D.1: Weight of the steel superstructure visualised

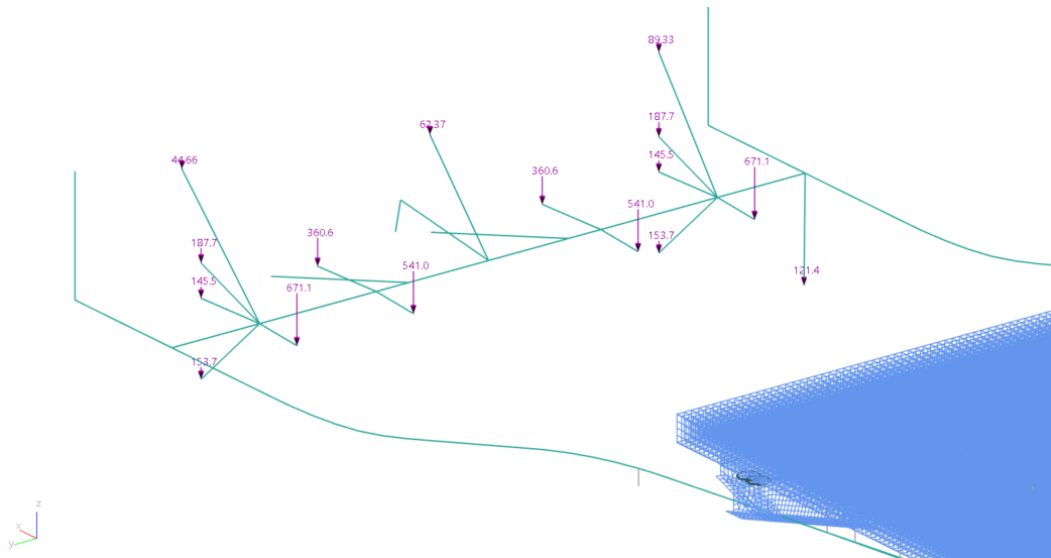


Figure D.2: Weight of the counterweight

FRP deck weight per square meter

$$\begin{aligned}
 V_f &= 0.5 & \rho_{E.glass} &:= 2510 \frac{\text{kg}}{\text{m}^3} & \rho_{Poly.Resin} &:= 1200 \frac{\text{kg}}{\text{m}^3} & \rho_{Foam} &:= 50 \frac{\text{kg}}{\text{m}^3} \\
 \rho_{GFRP} &:= V_f \cdot \rho_{E.glass} + (1 - V_f) \cdot \rho_{Poly.Resin} = 1.855 \times 10^3 \cdot \frac{\text{kg}}{\text{m}^3} \\
 B &:= 1000\text{mm} \\
 L_{\text{deck}} &:= 1000\text{mm} \\
 n_s &:= \frac{B}{s_w} + 1 = 9.333 \\
 m_w &:= n_s \cdot h_c \cdot t_w \cdot L \cdot \rho_{GFRP} = 62.328 \text{ kg} \\
 m_f &:= B \cdot L \cdot t_f \cdot \rho_{GFRP} = 37.1 \text{ kg} \\
 m_{foam} &:= h_c \cdot L \cdot [B - t_w \cdot (n_s - 1)] \cdot \rho_{Foam} = 16.5 \text{ kg} \\
 m_{sp} &:= m_w + m_f + m_{foam} = 115.928 \text{ kg} \\
 q_G &:= \frac{m_{sp} \cdot g}{B \cdot L} = 1.137 \cdot \frac{\text{kN}}{\text{m}^2}
 \end{aligned}$$

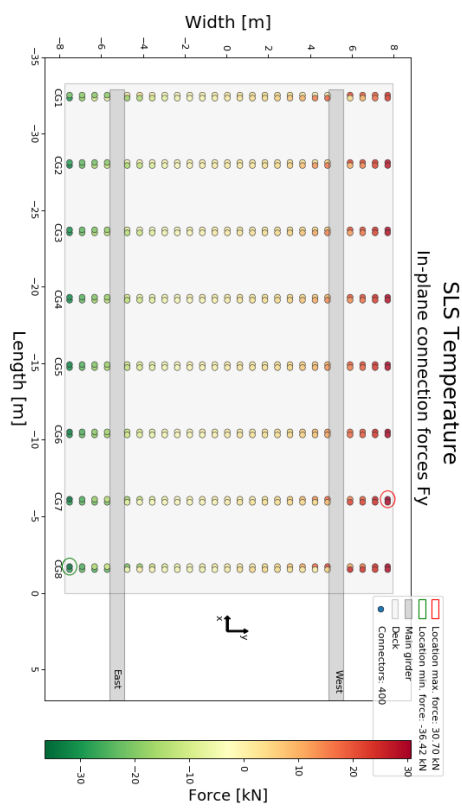
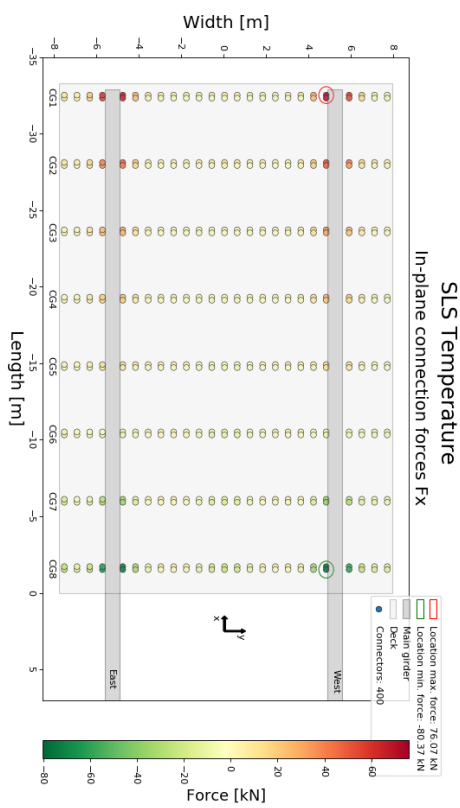
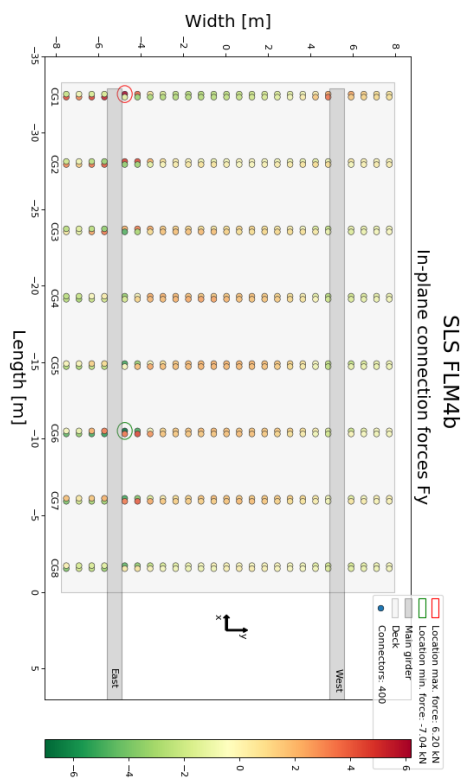
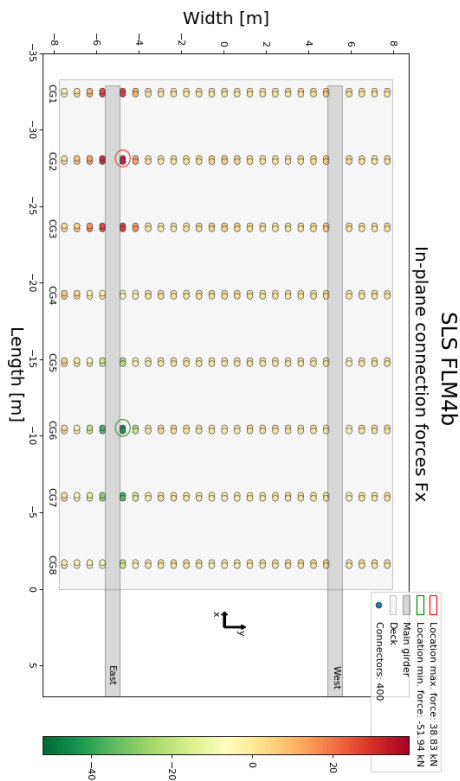
Figure D.3: Calculation of the weight of the FRP deck

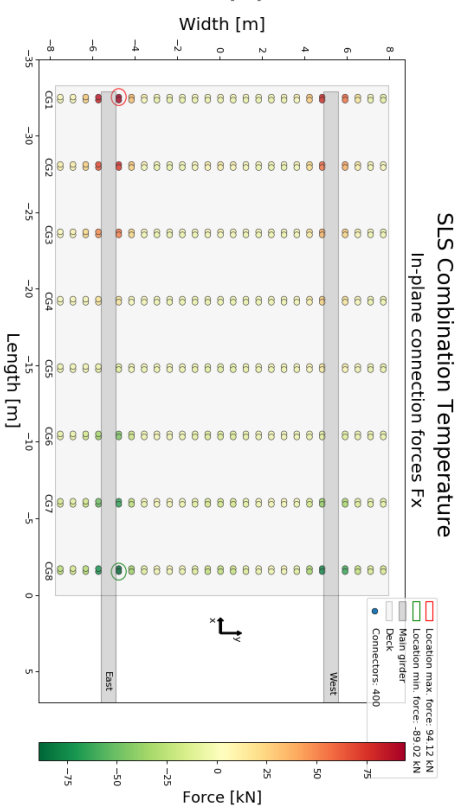
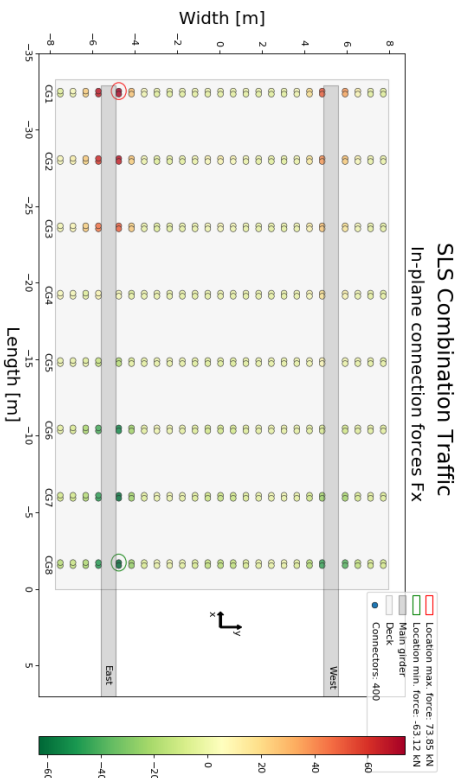
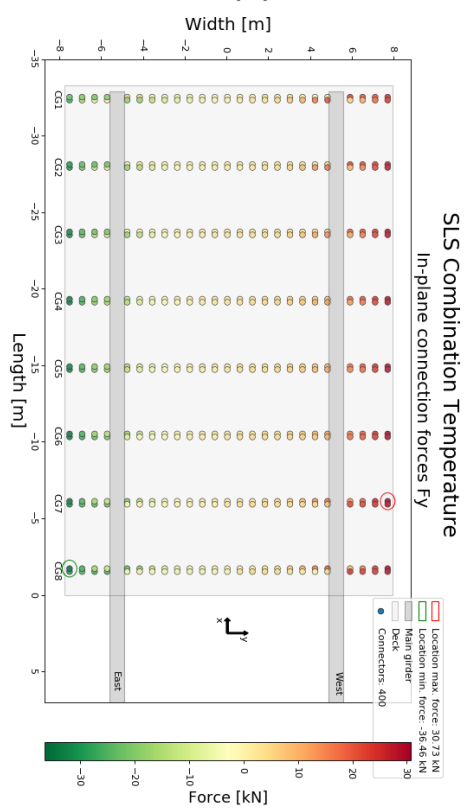
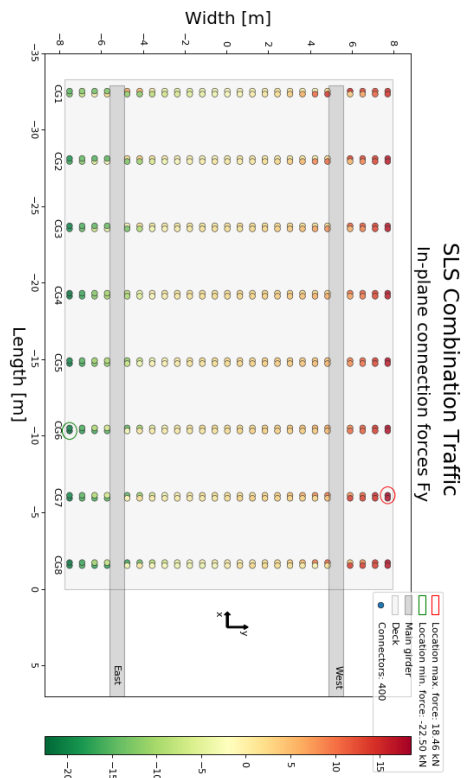
Original wooden deck weight

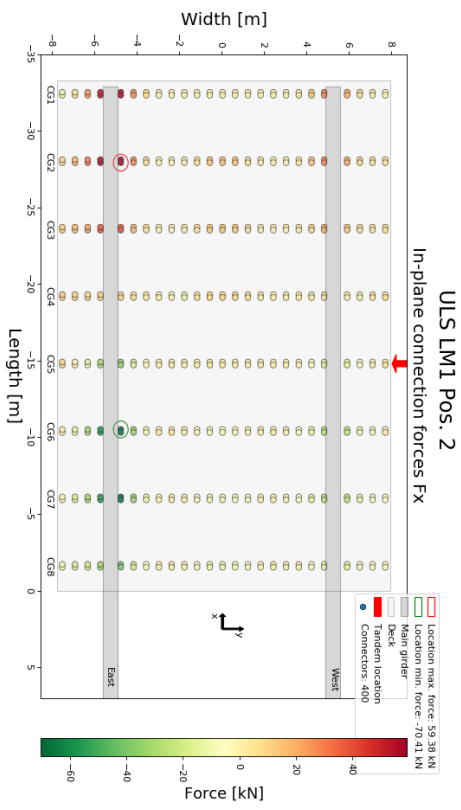
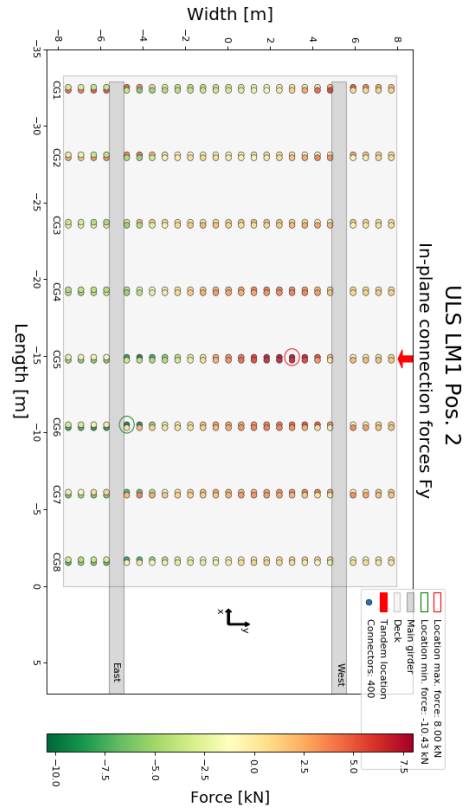
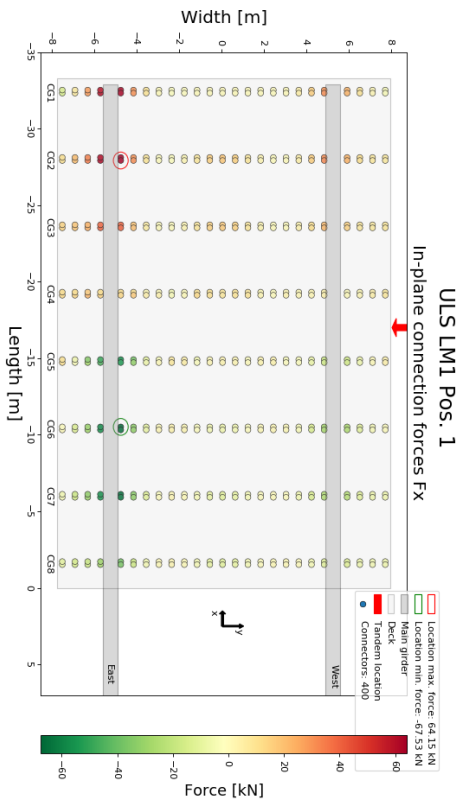
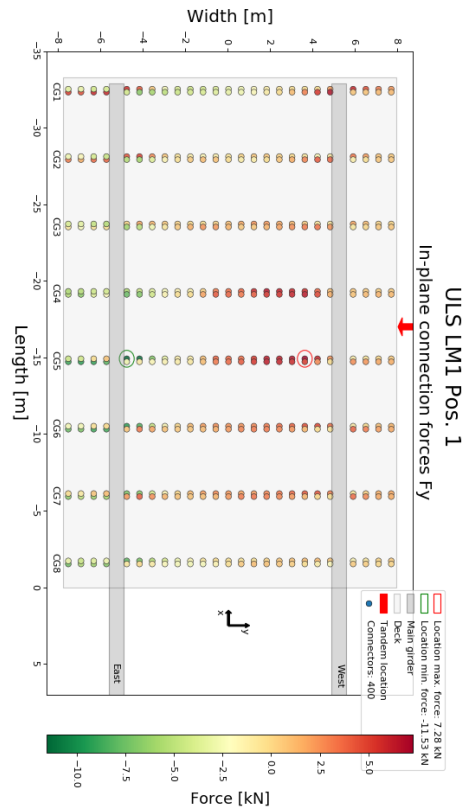
$$\begin{aligned}
 \rho_{\text{aobe}} &:= 1120 \frac{\text{kg}}{\text{m}^3} & n_{IPE360} &:= 21 \\
 h_{\text{deck}} &:= 110\text{mm} & \rho_{\text{steel}} &:= 7850 \frac{\text{kg}}{\text{m}^3} \\
 L_{\text{deck}} &:= 32.76\text{m} & A_{IPE360} &:= 72.7\text{cm}^2 \\
 B_{\text{deck}} &:= 15.5\text{m} \\
 m_{\text{A:obe.deck}} &:= L_{\text{deck}} \cdot B_{\text{deck}} \cdot h_{\text{deck}} \cdot \rho_{\text{aobe}} = 6.256 \times 10^4 \text{ kg} \\
 m_{IPE360} &:= n_{IPE360} \cdot A_{IPE360} \cdot L_{\text{deck}} \cdot \rho_{\text{steel}} = 3.926 \times 10^4 \text{ kg} \\
 m_{\text{deck}} &:= m_{\text{A:obe.deck}} + m_{IPE360} = 1.018 \times 10^5 \text{ kg} \\
 q_{G.\text{original}} &:= \frac{m_{\text{deck}} \cdot g}{B_{\text{deck}} \cdot L_{\text{deck}}} = 1.966 \cdot \frac{\text{kN}}{\text{m}^2}
 \end{aligned}$$

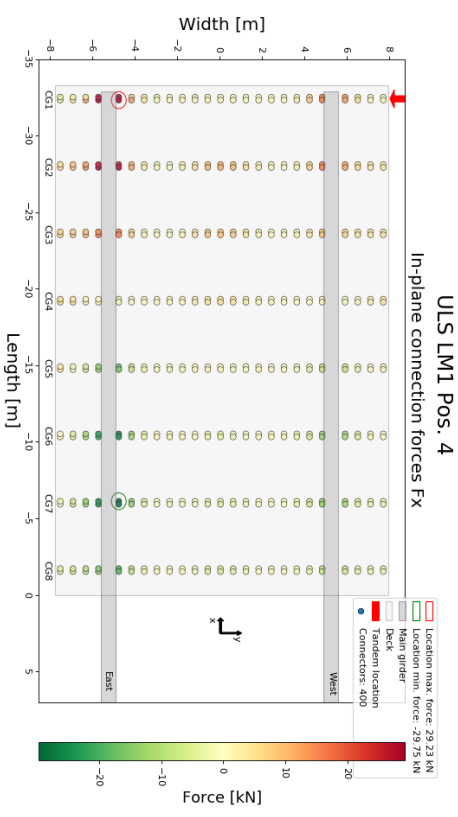
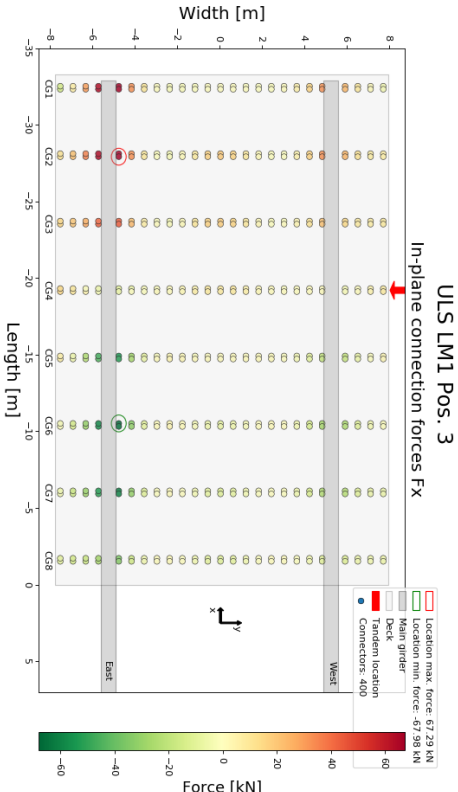
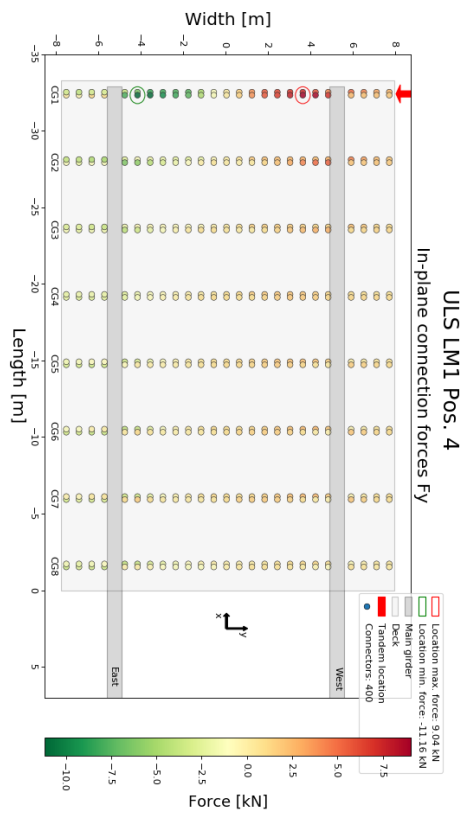
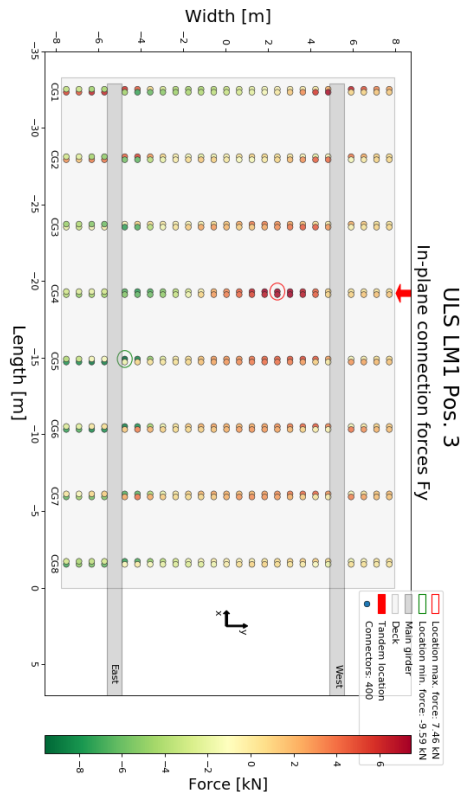
Figure D.4: Calculation of the weight of the timber deck including the secondary girders

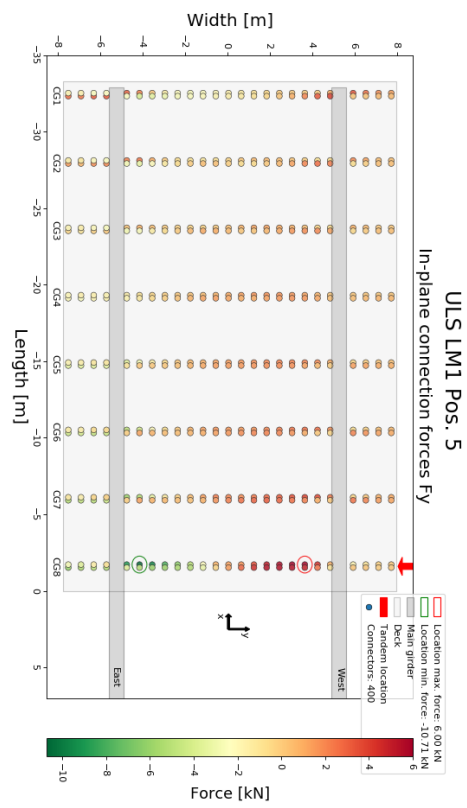
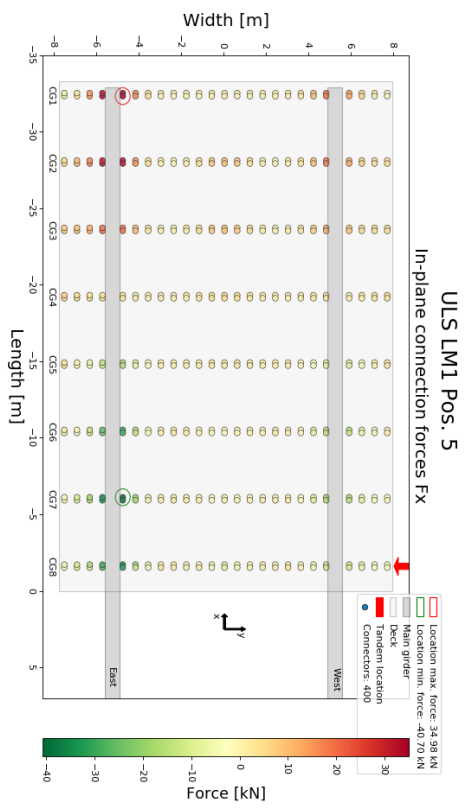
D.2. Connector forces: Cross-girder

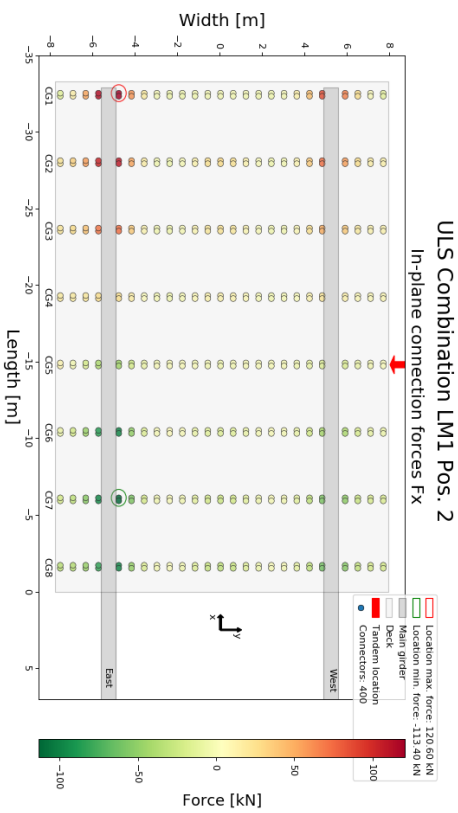
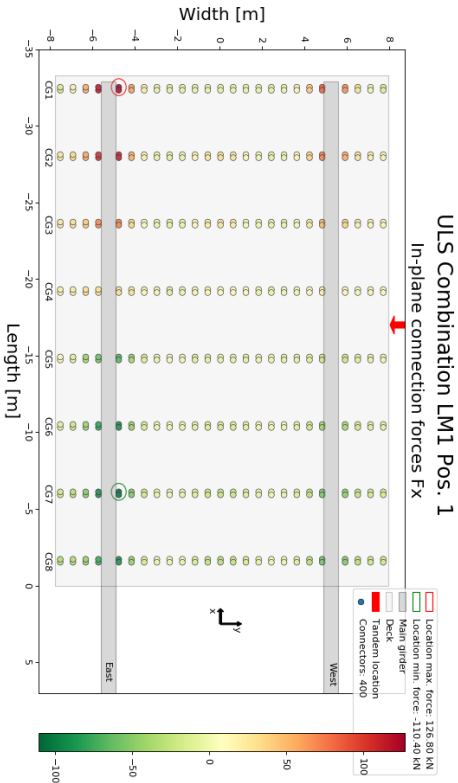
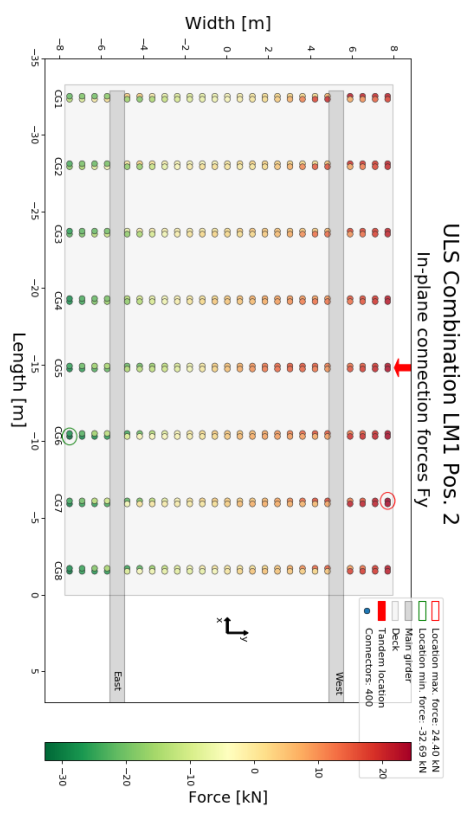
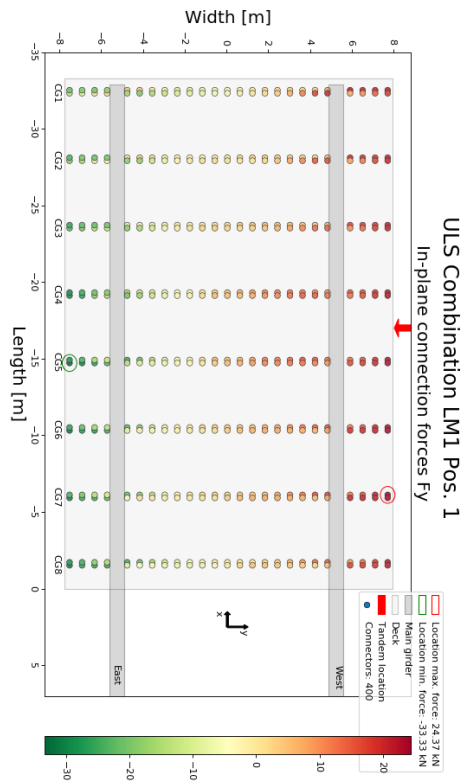


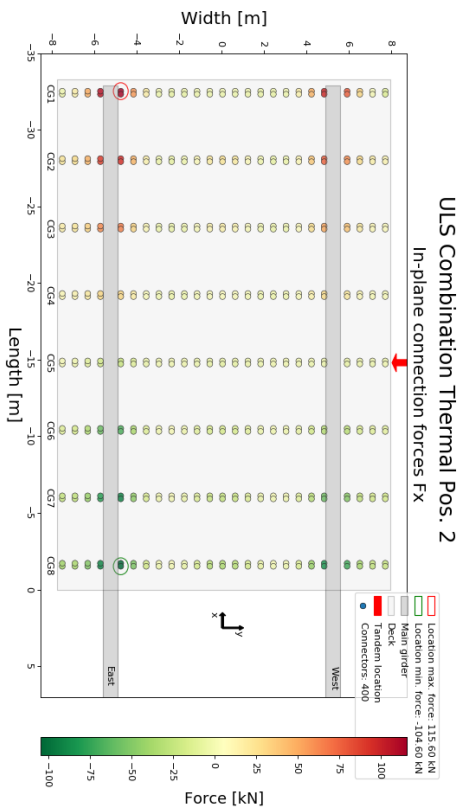
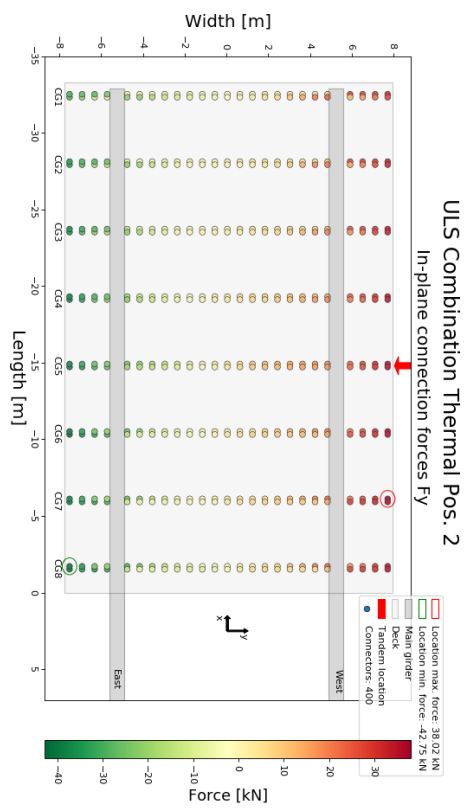
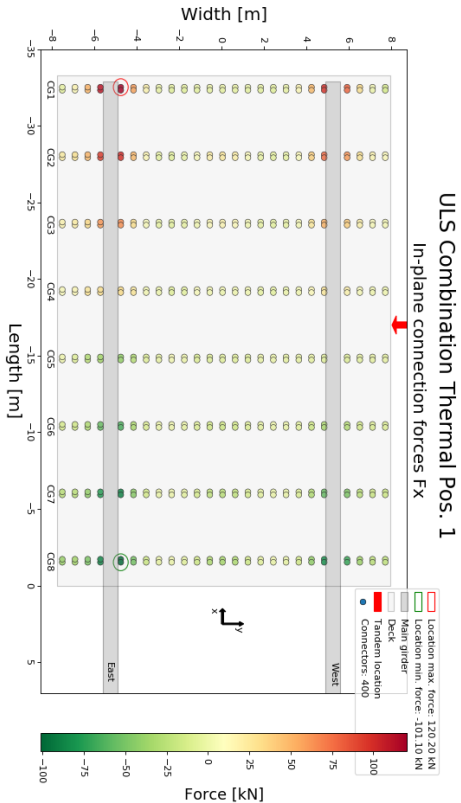
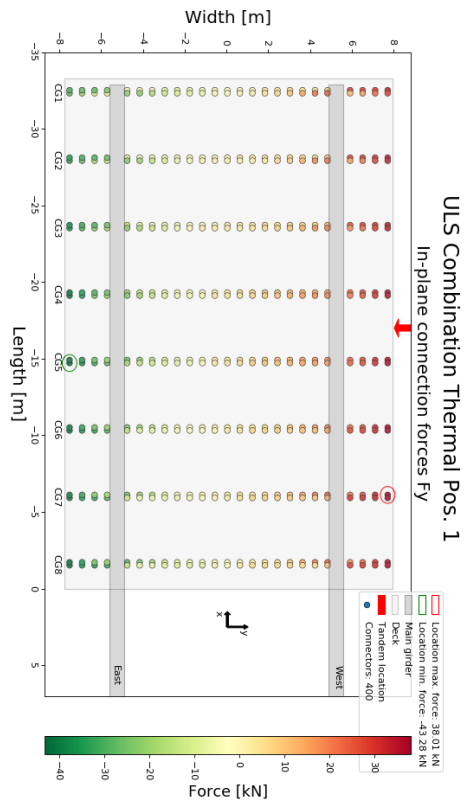












D.3. Connector forces: Cross- and main-girder

